Istituto Nazionale
di Fisica Nucleare
Laboratori Nazionali di Frascati

Preliminary

Technical Design Report

for the

SPARC Advanced Photo-injector

January 12, 2004

Laboratori Nazionali di Frascati
Istituto Nazionale di Fisica Nucleare

Editors:

Luigi Palumbo
James Rosenzweig

Contributors:

D. Alesini, S. Bertolucci, M.E. Biagini, C. Biscari, R. Boni, M. Boscolo, M. Castellano, A. Clozza, G. Di Pirro, A. Drago, A. Esposito, M. Ferrario, V. Fusco, A. Gallo, A. Ghigo, S. Guiducci, M. Incurvati, C. Ligi, F. Marcellini, M. Migliorati, C. Milardi, A. Mostacci, L. Palumbo, L. Pellegrino, M. Preger, P. Raimondi, R. Ricci, C. Sanelli, M. Serio, F. Sgamma, B.Spataro, A. Stecchi, A. Stella, F. Tazzioli, C. Vaccarezza, M. Vescovi, C. Vicario, M. Zobov *(INFN /LNF)*

F. Alessandria, A. Bacci, I. Boscolo, F. Broggi, S.Cialdi, C. DeMartinis, D. Giove, C. Maroli, V. Petrillo, M. Romè, L. Serafini, *(INFN /Milano)*

S. De Silvestri, M. Nisoli, S. Stagira *(Politecnico/Milano)*

D. Levi, M. Mattioli, G. Medici *(INFN /Roma1)*

L. Catani, E. Chiadroni, A. Cianchi, C. Schaerf, S. Tazzari *(INFN /Roma2)*

G. Dattoli, L. Giannessi, L. Mezi, L. Picardi, M. Quattromini, A.Renieri, C. Ronsivalle (ENEA/FIS)

S. Reiche, J. Rosenzweig , G. Travish *(UCLA)*
D. Dowell, P. Emma, C. Limborg, D. T. Palmer *(SLAC)*

Abstract

This document presents the Preliminary Technical Design Report for an advanced photo-injector, to be built at the Laboratori Nazionali di Frascati of INFN within the framework of the SPARC project.

The main goals of the SPARC injector project are: (1) the generation of a high brightness electron beam able to drive a self-amplified spontaneous free-electron laser (SASE FEL) experiment in the green visible light, and (2) the development of an ultra-brilliant beam photo-injector needed for the future SASE FEL-based X-ray sources.

Beams with the features anticipated in the SPARC project are also of strong interest for experiments into other cutting edge fields. The SPARC injector may allow investigations into the physics of ultra-short beams, plasma wave-based acceleration, and production of X-ray Compton back-scattering.

1. Introduction

1.1 Origin of the SPARC Project

Driven by the large interest that 4th generation light sources, *i.e.* X-ray SASE FELs, have raised world-wide in the synchrotron light scientific community, as well as in the particle accelerator community, and following the solicitations arising from several Italian national research institutions, the Italian Government launched in 2001 a long-term initiative devoted to the realization in Italy of a coherent X-ray source in the next decade.

To pursue this program, the Italian Government published two calls for proposals, in March 2001, and in December 2001, staging the initiative in two steps: a 3 year R&D program with a budget of 11 M , and a subsequent program for a X-ray coherent source planned to be built in the second phase with a budget of 96 M . The budget is comprised of 70% from the Government and 30% from the proposing institutions.

In March 2002 the SPARC proposal, born from a collaboration among ENEA, INFN, CNR, Università di Roma “Tor Vergata”, Sincrotrone Trieste and three units of the INFM, and strategically oriented to explore both the feasibility of a ultra-brilliant photo-injector and to perform a SASE-FEL experiment at □500 nm, was approved. The project was funded with 9.5 M budget, and the Government funding (70%) was delivered on January 2003, allowing the project to commence.

Almost a year before, in February 2002, the collaboration submitted also the SPARX proposal, an initiative that is tightly correlated to the approved project SPARC. The SPARX project is directed towards the construction of a coherent soft X-ray source in the “Tor Vergata” University Campus.

The SPARC proposal and subsequent approval have followed a path that is quite different from the process that INFN projects usually undertake. In fact, the proposal was based on a preliminary conceptual design, and a real effort on the project was planned only after the approval. Despite the uncertainty about the project, due to an unexpected delay of funding from MIUR, the SPARC injector group worked with high dedication in order to proceed with the optimization of the working point, the design of subsystems and with the technical specifications of the accelerator components. This work achieved on these design tasks is summarized in the present report.

1.2 Goals of the SPARC Project

The overall SPARC project consists of four main lines of activity directed towards several goals; their common denominator is to explore the scientific and technological issues that give rise to the most crucial challenges on the way to the realization of a SASE-FEL based X-ray source. These are:

- **150 MeV Advanced Photo-Injector**

Since the performances of X-ray SASE-FEL's are critically dependent on the peak brightness of the electron beam delivered at the undulator entrance, this activity was conceived with the purpose of investigating two main issues:

1) generation of a high brightness electron beam by means of an innovative scheme of space charge compensation, able to drive an FEL-SASE experiment at □500 nm.
2) generation of a ultra high brightness, high peak current beams, via RF and/or magnetic compressors, suitable for future X-Ray sources.

Due to short schedule and limited budget, the task (1) was given the priority inside the MIUR proposal, and forms what we will refer to as SPARC Phase 1. Nevertheless, the latter task is of urgent importance for the development of ultra-brilliant electron beams. Therefore, although the SPARC injector group is concentrated on the tasks of Phase 1, some strategic activity will continue on the secondary tasks in description 2) in order to perform the necessary work that will enable Phase 2 of the SPARC project to continue with as little delay as possible beyond the successful completion of Phase 1.

This activity is performed under the responsibility of INFN and is the main subject of the present report.

- **SASE-FEL Visible-VUV Experiment**

This component of the SPARC initiative foresees: a) performance of a SASE FEL experiment with the 150 MeV photo-injector-derived beam, using a segmented undulator with additional strong focusing, to observe FEL radiation at 500 nm and below; b) investigation of the problems related to matching the beam into an undulator and keeping it well aligned to the radiation beam, as well as the generation of non-linear coherent higher harmonics.

This activity is under the responsibility of ENEA.

- **X-ray Optics/Monochromators**

Radiation emitted from an X-ray FEL will provide photon beams to users that are unique in terms of peak brightness and pulse time duration (100 fs). Such beams pose severe challenges in implementing the optics necessary to guide and handle the intense radiation. This project will pursue also a vigorous R&D activity on the analysis of radiation-matter interactions in the spectral range typical of SASE X-ray FEL's (from 0.1 to 10 nm), as well as the design of new optics and monochromators compatible with these beams.

This activity is under the responsibility of CNR, and will be developed at the collaborating CNR institutes.

- **Soft X-ray table-top Source**

In order to test the optics developed for X-ray SASE FEL sources, and to begin R&D on ultra-short X-ray-based applications, the project will undertake an upgrade of the presently operated table-top source of X-rays at INFM-Politecnico Milano. This source will deliver 10^7 soft X-ray photons in 10-20 fs pulses by means of high harmonic generation of an ultra-fast intense laser pulse in a gas. This will be a very useful test-bed for techniques developed in the research into X-ray optics and monochromators.

This activity is under the responsibility of INFM, and will be developed at the INFM institutes.

The first two activities listed above are strictly connected, and can be considered as a unique R&D program. Therefore, although this report concerns mainly the photo-injector and its lay out, the parameter list and the working point optimization will be presented for the full photo-injector/FEL system. Further, as this document is meant to concentrate on the electron beam generation portion of the project, descriptions of technical components will be given only for the photo-injector.

Schematic drawings displayed at the end of this report show the exact location inside the Frascati Laboratories, and the layout of the full system, photo-injector plus undulator, inside the SPARC hall.

2. SPARC Layout and Parameter Lists

2.1 SPARC LAYOUT

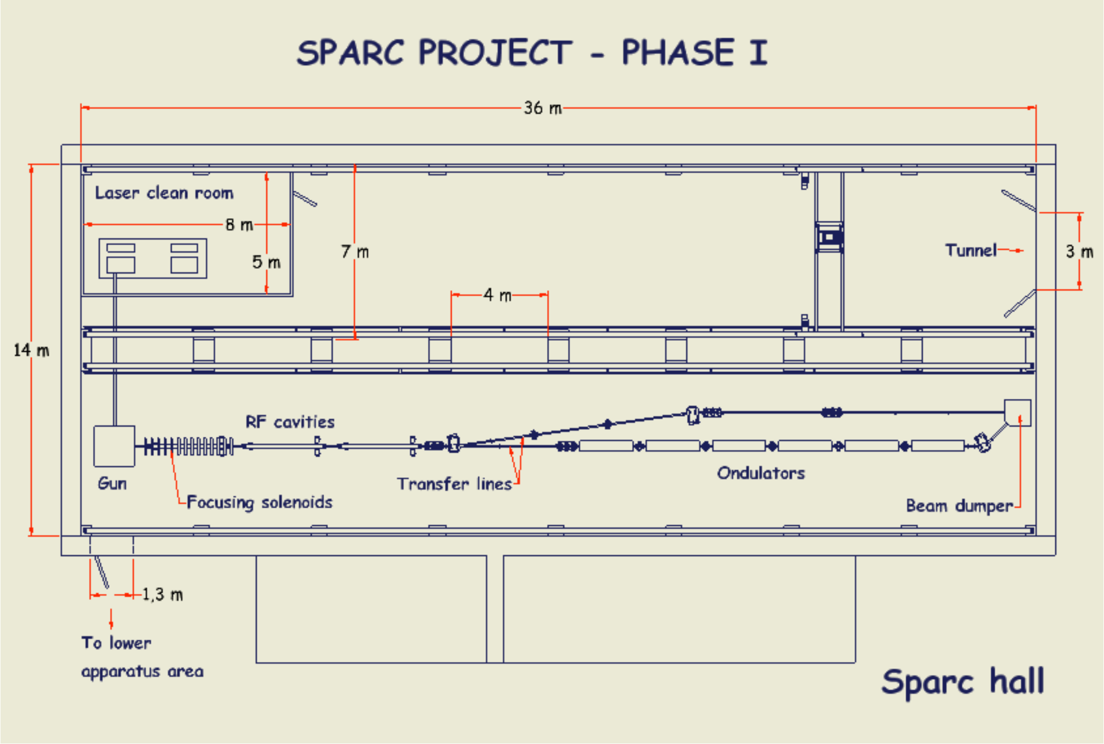

Figure 2.1: *Schematic of layout of the SPARC photo-injector complex inside the SPARC experimental hall, including undulator, and by-pass line (Phase 1).*

The proposed system to be built consists of: a 1.6 cell RF gun operated at S-band (2.856 GHz, of the BNL/UCLA/SLAC type) and high peak field on the cathode (≥120 MV/m) with incorporated metallic photo-cathode (Copper or Mg), generating a ≥5.6 MeV beam which is properly focused and matched into 3 accelerating sections of the SLAC type (S-band, travelling wave) which accelerate the bunch up to 150-200 MeV. The final layout of SPARC showing Phase 1 is displayed in Fig. 2.1.

The choice of the S-band Linac with respect to a L-band is due to compactness of the system, the lower cost, and the existence at LNF of a 800 MeV Linac based on the same technology, with obvious advantages on the side of the expertise and spares components. Morover, the higher RF frequency leads to a higher peak brightness attainable by an optimized photo-injector.

The production of highest brightness electron beams in the photo-injector requires that a temporally-flat, picosecond laser source be used to drive the photo-cathode. The laser system driving the photocathode will therefore employ high bandwidth Ti:Sa technologies with the oscillator pulse train locked to the RF (Fig. 2.2). The Ti:Sa mode locked oscillator and amplifiers able to produce the requested energy per pulse (500 μJ at 266 nm) are commercially available. To obtain the desired time pulse shape we will test the manipulation of frequency lines in the large bandwidth of Ti:Sa, in order to produce the 10 ps long flat-top shape. We plan to use a liquid crystal mask in the Fourier plane of the non-dispersive optic arrangement or a collinear acousto-optic modulator for linear frequency manipulation.

The SASE FEL experiment will be conducted using a permanent magnet undulator made of 6 sections, each 2.15 m long, separated by 0.39 m gaps, and featuring single quadrupoles which focus the electron beam in the horizontal plane. The undulator period is set at 2.8 cm, with an undulator parameter $k_w = 2.15$.

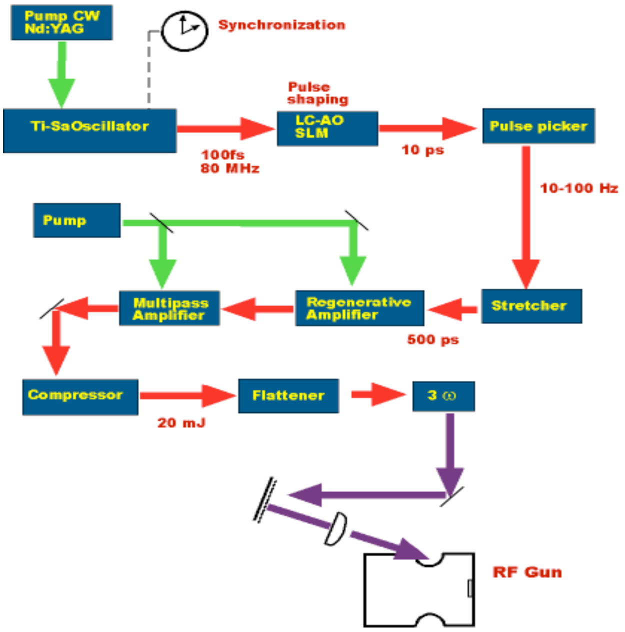

Figure 2.2*: Layout of the photocathode laser system.*

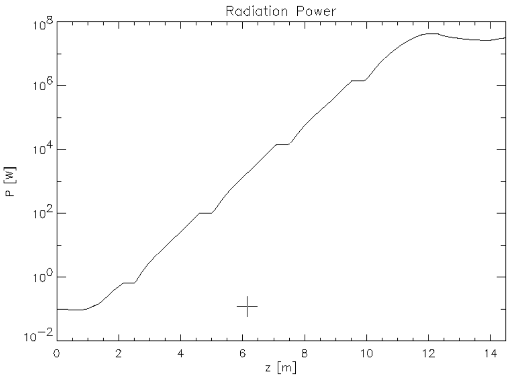

Figure 2.3*: Radiation Power at 500 nm growth along the undulator, from GENESIS simulation.*

A simulation performed with GENESIS is reported in Fig.2.3, showing the exponential growth of the radiation power at 500 nm along the undulator; almost 10^8 W can be reached after 12 m of total undulator length. Preliminary evaluations of the radiation power generated into the non-linear coherent odd higher harmonics show that 10^7 and 7×10^5 W can be reached on the third and fifth harmonics, respectively.

The second beam line is envisioned to by-pass the undulator, thus experiments on magnetic pulse compression to be performed. In particular, in Phase 2, it is foreseen to investigate emittance degradation due to CSR induced effects on and surface roughness wake-field effects.

2.2 SPARC PARAMETER LIST (Release 2, December 19th 2003)

We present here the parameter lists describing the photo-injector in two slightly different configurations, (A) 155 MeV and (B) 200 MeV operation. The 155 MeV case has been intensively studied for use in driving the FEL. The higher energy operation is of course interesting, as it results to be the maximum allowed beam energy for FEL experiments.

2.2.1 Standard parameter set, no bunch compression

Table 2.1 *(Ferrario working point, distance 1st section entrance to cathode = 1.5 m, gap between sections 0.5 m, two cases with three accelerating sections at 155 MeV and 200 MeV)*

ELECTRON BEAM	**A**	**B**
Electron Beam Energy (MeV)	**155**	**200**
Bunch charge (nC)	1.1	1
Repetition rate (Hz)	1-10	1-10
Cathode peak field (MV/m)	120	120
Peak solenoid field @ 0.19 m (T)	0.273	0.273
Photocathode spot size (mm, hard edge radius)	1.13	1
Central RF launch phase (RF deg)	33	35
Laser pulse duration, flat top (ps)	10	12
Laser pulse rise time (ps) 10%→ 90%	1	1
Bunch energy @ gun exit (MeV)	5.6	5.6
Bunch peak current @ linac exit (A)	100	85
Rms normalized transverse emittance @ linac exit (mm-mrad); includes thermal comp. (0.3)	< 2	< 2
Rms slice norm. emittance (300 μm slice)	< 1	< 1
Rms longitudinal emittance (deg.keV)	1000	1250
Rms total correlated energy spread (%)	0.2	0.2
Rms incorrelated energy spread (%)	0.05	0.05
Rms beam spot size @ linac exit (mm)	0.4	0.3
Rms bunch length @ linac exit (mm)	1	1

DRIVE LASER SYSTEM	
Laser central wavelength (nm)	780
Laser oscillator rep rate (MHz)	79.3
Laser pulse length @ oscillator exit (fs)	100
Laser pulse energy (IR) @ amplifier output (mJ)	20
Laser pulse energy (UV) @ photocathode (mJ)	0.5
Repetition rate (Hz)	1-10
Laser pulse duration, flat top (ps)	8-12
Laser pulse rise time (ps) 10%→ 90%	< 1
Phase jitter w.r.t. RF (ps)	< 1
Rms energy jitter in UV (shot-to-shot) (%)	5
Rms pointing stability on cathode (mm)	< 0.1
Flat top uniformity (peak-to-peak) (%)	< 30
Intensity transverse uniformity on photocathode (%)	20
Spot ellipticity on cathode: (1-*a*/*b*) (%)	< 10

RF GUN and LINAC	**A**	**B**
Maximum peak field at cathode (MV)	120	
Maximum rep rate (Hz)	10	
RF pulse duration (μs)	4.5	
Gun RF peak power (MW) at 140 MV/m	15	
Operating vacuum - RF, laser on (Torr)	10^{-9}	
Operating temperature (deg C)	45	
Cathode material(s)	Cu, Mg	
Quantum efficiency	10^{-5}, 10^{-4}	
Laser incidence angle @ cathode (deg)	72	
Maximum solenoid magnetic field (T)	0.31	
Power supplies for gun solenoid sections	4	
1st section accel. gradient (MV/m)	25	25
1st section accel. Phase (RF deg)	on crest	on crest
2nd section accel. gradient (MV/m)	12.5	25
2nd section accel. Phase (RF deg)	on crest	on crest
3rd section accel. gradient (MV/m)	12.5	15
3rd section accel. Phase (RF deg)	on crest	on crest
RF peak power per section (MW)	55,15,15	55,55,20
# klystrons	2	2
# solenoids on 1st section	12	12
# linac solenoid power supplies	4	4
Magnetic field on 1st linac section (Gauss)	750	750

TRANSFER LINE	**A**	**B**
Drift (m)	0.5	0.5
Q1 length (m)	0.1	0.1
Q1 gradient (T/m)	-4.4	-7.4
Drift (m)	0.15	0.15
Q2 length (m)	0.1	0.1
Q2 gradient (T/m)	9.3	9.4
Drift (m)	0.15	0.15
Q3 length (m)	0.1	0.1
Q3 gradient (T/m)	-5.0	-1.2
Drift (m)	2.95	2.95
Q4 length (m)	0.1	0.1
Q4 gradient (T/m)	-4.3	-9.7
Drift (m)	0.15	0.15
Q5 length (m)	0.1	0.1
Q5 gradient (T/m)	3.3	9.3
Drift (m)	0.15	0.15
Q6 length (m)	0.1	0.1
Q6 gradient (T/m)	8.3	8.4
Drift (m)	0.75	0.75
Total length (m)	5.4	5.4

UNDULATOR & FEL	**A**	**B**
Undulator period (cm)	2.8	2.8
# Undulator sections	6	6
Undulator parameter	2.15	2.15
Undulator field on axis (T)		
Undulator gap (mm)	9.5	9.5
Undulator section length (m)	2.16	2.16
Drifts between undulator sections (m)	0.39	0.39
FEL wavelength (nm)	500	290
Saturation length (m, geometrical)	< 12	NA
FEL pulse length (ps)	3	NA
FEL power @ saturation (MW)	> 80	NA
Brilliance (st. units)		NA
# Photons/pulse	10^{15}	NA
FEL power @ sat. (MW) 3rd harm.	> 10	NA
FEL power @ sat. (MW) 5th harm.	> 0.7	NA

3. Photo-Injector Design Optimization

3.1 OVERVIEW

The SPARC photoinjector serves two requirements. First, it serves as test-bend for development of techniques and concepts in high brightness beam generation and manipulations. Second, and not less importantly, it is to be employed for driving a SASE FEL experiment at 500 nm, as discussed in the general project overview. The FEL requirements, being a test of the entire integrated system robustness at SPARC, may be taken, therefore, as the nominal design parameters for the injector. To meet the FEL requirements a high brightness (high current low emittance, $B_n = 2I/\varepsilon_n^2$) electron beam has to be generated, accelerated up to 155 MeV and transported up to the entrance of the undulator, minimizing the emittance and energy spread degradation due to correlated space charge and wake field effects.

In order to saturate the FEL radiation in the planned 12 m long undulator, and to additionally allow generation of higher harmonics, the design beam parameters are very rigorous: normalized emittance $\varepsilon_n < 1$ μm, relative energy spread $\Delta\gamma/\gamma < 0.1$ % and peak current $I \sim 100$ A. Fortunately, such parameters have to be reached only on the scale of the FEL cooperation length, which in our case is about 300 μm. With these demands in mind, detailed beam dynamics studies that allow current and phase space optimization have been performed. These include start-to-end simulations for the ideal case, in which all known realistic phenomena that affect the beam dynamics are included. These simulations display the sometimes subtle effects that details of the beam distribution in phase space on may exert on beam optimization and on FEL performance. This sensitivity has been noted in previous SASE FEL experiments using similar systems. Because of this need to know phase space details whenever possible, and to benchmark simulations so the other more difficult to measure parameters may be determined, simulation models have been developed for “virtual diagnostic experiments”. These simulations allow us to examine collective effects in measurements, and also give us fundamental insights about what one may actually measure, and learn about the beam dynamics systems, during the injector commissioning.

We discuss in this chapter the present status of beam dynamics simulation activities. We begin in the following section by describing the simulation tools we have adopted or developed to study the beam dynamics of the SPARC project. The approach to achieving the design criteria and the start-to-end simulation for the nominal working point of the injector/FEL system are then discussed in Section 3.3. Phase 1a of the SPARC project will consist in the commissioning of the laser/rf photocathode gun/solenoid system (5.6 MeV beam), with a systematic measurement of the emittance compensation process along the subsequent drift. The main goal of this experiment is to collect as much information as possible about the 6D beam phase space evolution, in order to obtain the capability of understanding and optimizing the SPARC system with full energy beam. A dedicated emittance-meter tool has been foreseen in this phase, as discussed in the diagnostic section of this TDR. This task is critical for benchmarking simulation tools, and can only be accomplished in Phase 1a, when there is no interference from post-acceleration linac hardware, In support of this delicate phase of the project, we have developed a simulation tool able to reproduce as closely as possible the proposed measurement technique, as discussed in Section 3.4. Similarly for phase 1b (155 MeV operation) we discuss the slice emittance measurement through examination of simulations. The effects of beam perturbations on the injector performance are studied Section 3.5.

Phase 2 of the project will consist mainly in beam compression techniques studies, via a magnetic chicane device and via a new technique based on the so-called velocity bunching. In Section 3.6 we discuss the injector performances comparing the two beam compression option foreseen, in particular the velocity bunching technique and its possible integration in a higher energy linac.

It is worthwhile to compare the state of the art in photo-injectors, in terms of beam quality achieved so far at different RF frequencies, to the goals set for the SPARC project.

In the following table we list the most relevant parameters characterizing the measured beam emittance and brightness at this selection of laboratories. Most laboratories used non-shaped laser pulses, i.e. pulses with the natural gaussian time-profile produced by the oscillator: only the Sumitomo photo-injector adopted laser shaping, achieving a quasi uniform flat–top time profile in the laser pulse. The improvement obtained is dramatic, almost a factor 2 decrease in the emittance. L-band performances confirm that the current tend to be lower than S-band case, mainly because of the lower cathode peak field achieved (typically 50 MV/m vs. 100): the LANL case is sort of an exception with 85 A per nC of bunch charge. This result was obtained in a special multi-cell RF gun design which keep the space charge longitudinal debunching much lower that in split photo-injectors. We can see that the Sumitomo result are close to the goals set for the SPARC project with which we want to achieve a similar brightness with an equilibrated beam, i.e. at an energy larger than 150 MeV where the emittance is no longer sensitive to envelope (plasma) oscillations. To this end SPARC photo-injector lay-out is based on the Ferrario working point, expected to give minimum emittance at the photo-injector exit and the laser beam pulse will be shaped to quasi uniform flat-top profile. A third relevant characteristic issue of SPARC injector will be the investigation of the bunch compression with RF techniques.

Laboratory	Q [nC]	Energy [MeV]	I [A]	Laser Pulse shaping	ϵ_n [μm]	ϵ_n slice [μm]
UCLA (S)	0.5	15	80	no	3	
BNL (S)	0.2	71	85	no	1.5	0.8
NERL (S)	0.5	25	50	no	3	
GTF (S)	0.3	30	100	no	1.5	
SUMI (S)	1	14	100	yes	1.2	
SUMI (S)	1	14	100	no	2.1	
LANL (L)	2	18	170	no	7	5
TTF (L)	1	233	50	no	3	

3.2 SIMULATION TOOLS

It has been well established in the high brightness beam community that a start to end simulation of a SASE FEL experiment must be performed by means of the PARMELA-ELEGANT-GENESIS chain of codes [1]. We have adopted the same tools in our studies, and have additionally employed simpler codes that we have developed to speed up the process of beam parameter scanning, and more complex codes to study in more detail 3D effects. We cross-check the results across levels of complexity in this hierarchy of codes. We list below our arsenal of simulation codes, with short descriptions of their capabilities and range of applicability:

Simulation codes for the injector/linac:

— **PARMELA** is an electron-linac particle-dynamics code[2],[3]. It is a wide spread reliable multi-particle code that transforms the beam, represented by a collection of particles, through a user-specified linac and/or transport system, where field maps of magnets and accelerator cavities are derived from **POISSON** and **SUPERFISH**. It includes a 2-D and 3-D space-charge calculation in the "quasi static" approximation, and therefore does not include radiative effects in bends. Both LANL and UCLA versions of this code are employed in SPARC studies.

— **HOMDYN** relies on a multi-envelope model based on the time dependent evolution of a uniform bunch approximation[4]. The algorithm is very efficient and despite some strong simplifying assumptions it allows the quick relaxation of the large number of parameters involved in parameter studies, to quickly find a reasonably optimized configuration. After fast scanning with HOMDYN, PARMELA is typically used to explore the proposed working point. It does not presently have a strong model for bending systems

— **TREDI** provides a rigorous space charge fields description by taking into account the effects due to the finite propagation velocity of signals through the bunch with a 6D time dependent representation of beam dynamics[5]. Space charge forces are calculated by a Lienard-Wiechert retarded potential formalism. This is accomplished in TREDI by storing the histories of macro-particles trajectories, and by tracking back in time the source coordinates until the retarded condition is satisfied, a very memory-intensive process. The effects of boundaries for flat walls are included by the image charge method.

— **ABCI** computes wakes field, impedances and loss factors, by solving the Maxwell equation in the time domain for a Gaussian bunched beam propagating through an axi-symmetric structure on or off axis[6].

Simulation codes for beam transport

— **ELEGANT:** is an beam dynamics code that computes Twiss parameters, transport matrices, nonlinear transport to 3rd order, closed orbits, beam transport floor coordinates, error amplification factors, dynamic apertures, and more[7]. It performs 6-D tracking with matrices and/or canonical integrators, and supports a variety of time-dependent elements. It computes coherent synchrotron radiation effects using a 1D model, and also performs optimization algorithms *(e.g.,* matching), including optimization of tracking results.

- **MAD:** is a tool for charged-particles optics in alternating gradient accelerators and beam lines[8]. Includes linear lattice parameter calculation, linear lattice matching, transfer matrix matching, and particle tracking.

- **RETAR:** a 3D EM PIC code based on retarded potentials via an integral algorithm. It was recently developed by the SPARC group and is presently under test. It can describe in a self-consistent fashion the interaction of an electron bunch with its own self-field (velocity and radiation field). Only flat boundaries can be treated in the present version.

Simulation codes for free electron laser dynamics

- **GENESIS:** is a time-dependent three-dimensional FEL simulation code [9]. It is mainly devoted to the simulation of single pass free electron lasers, integrates the averaged electron motion in the undulator as it is coupled to the radiation fields, which evolve in the "slowly varying envelope approximation".

- **GINGER:** direct descendant of the LLNL FEL simulation code "FRED", GINGER as GENESIS is a KMR wiggler period averaged FEL code. The fields are assumed in cylindrical symmetry while the electron trajectories are integrated in 3D [10].

- **MEDUSA:** is a 3D, multifrequency, macroparticle simulation code that represents the electromagnetic field as a superposition of Gauss-Hermite modes and uses a source-dependent expansion to determine the evolution of the optical mode radius[11]. The field equations are integrated simultaneously with the Lorentz force equations. MEDUSA differs from other nonlinear simulation codes in that no undulator-period averaging is imposed on the electron dynamics.

- **PERSEO:** the "Perseo" FEL-cad library allows the 1D time dependent simulation of SASE FEL configurations, oscillator configurations and exotic configurations like MOPA, it includes higher order harmonics and startup from shot-noise[12].

- **PROMETEO:** is a 1D, multiparticle code based on a modified version of the Prosnitz, Szoke, and Neil formulation of FEL dynamical equations. The original model has been generalized to include the effect of beam emittance and the undulator errors. The code is capable of accounting for the evolution of the coherent generation of higher-order harmonics in SASE or oscillator FELs, including the optical klystron and segmented undulators [13].

3.3 DESIGN CRITERIA

A detailed theoretical study of the emittance compensation process in a photoinjector [14] has demonstrated that the optimization of a photoinjector corresponds to accelerating and propagating the beam through the device as closely as possible to two relevant beam equilibria: a laminar Brillouin flow in drifts and the so-called invariant envelope in accelerating sections, which is a generalization of Brillouin flow for an accelerated beam. In this case the beam undergoes cold plasma oscillations of spatial wavenumber k_p, in which the space charge collective force is largely dominant over the emittance pressure. The frequency of the plasma oscillations, due to mismatches between the space charge force and the external focusing gradient, is to first order independent of the current while the betatron motion (trajectory cross-over) is almost absent (laminar flow). In fact it is the frequency independence that leads to reversible normalised emittance oscillations: accelerating the beam on the invariant envelope damps these oscillations like the square root of the beam energy, so that the normalised emittance at the injector exit reduces to a steady state minimum when the oscillations are properly tuned.

It has been shown that the rms projected normalized transverse emittance $\varepsilon_n = \sqrt{\langle x^2\rangle\langle(\beta\gamma x')^2\rangle - \langle x\beta\gamma x'\rangle^2}$ oscillates with a frequency $\sqrt{2K_r} = k_p$ at an amplitude $\Delta\varepsilon_n \propto \sqrt{\hat{I}/\gamma}$ whenever a bunched beam is rms matched into a focusing channel of gradient K_r, *i.e.* on a Brillouin flow equilibrium:

$$\sigma_B(\zeta) = \sqrt{\frac{\hat{I}(\zeta)}{2I_0\gamma^3 K_r}} \tag{3.1}$$

where σ is the rms beam spot size, eventually slice dependent, $\zeta \equiv z - \beta ct + z_0$ is the slice position, $\hat{I}$ is the peak current and I_O=17 kA the Alfven current. In a similar way, accelerating on the invariant envelope,

$$\sigma_{inv}(\zeta) = \frac{2}{\gamma'}\sqrt{\frac{\hat{I}(\zeta)}{I_0\gamma}}, \tag{3.2}$$

where $\gamma' = eE_{acc}/m_e c^2$ (E_{acc} is the accelerating field), which is a particular exact solution of the rms envelope equation in the laminar flow regime, leads to *damped* oscillations of the emittance, and secular diminishing of the amplitude of the oscillations.

The basic point in the design of a photoinjector is therefore to match properly the beam at injection into any accelerating section, according to these criteria:

$$\sigma' = 0 \tag{3.3}$$

implying a laminar waist at injection and

$$\gamma' = \frac{2}{\sigma_w}\sqrt{\frac{\hat{I}}{2I_0\gamma}} \tag{3.4}$$

giving an rms match on the invariant envelope for a TW accelerating field.

The laminar regime extends up to an energy given by:

$$\square = \sqrt{\frac{8}{3}}\frac{\hat{I}}{2I_o\square_{th}\square\square} \qquad (3.5)$$

where $\square_{th}$ is the thermal emittance. With the expected SPARC parameters: $\hat{I}$=100 A, E_{acc}=25 MV/m and an estimated [15] thermal emittance of 0.3 □m for a Cu cathode with UV excitation, the transition occurs around 150 MeV (this estimate assumes little additional uncorrelated emittance is added through nonlinear space-charge forces and other effects[16]). For this reason the emittance compensation process of the SPARC injector has to be optimized up to the exit of the booster linac, before injecting the beam in the undulator through the transfer line, which in turn must be examined for its emittance preserving properties.

Following the previous matching condition a new working point very suitable to damp emittance oscillations has been recently found [17] in the context of the LCLS FEL project [18] and adopted also by the TESLA-FEL[19] and ORION[20] facilities. By a proper choice of rf gun and solenoid parameters, the emittance evolution shows a double minimum behavior in the drifting region (see simulations in Chapter 4), caused by a chromatic effect occurring in the solenoid[21]. If the booster is located where the relative emittance maximum and the envelope waist occur, the second emittance minimum can be shifted at the booster exit line as shown in following figure and frozen at a very low level, preventing additional emittance oscillations in the subsequent beam propagation.

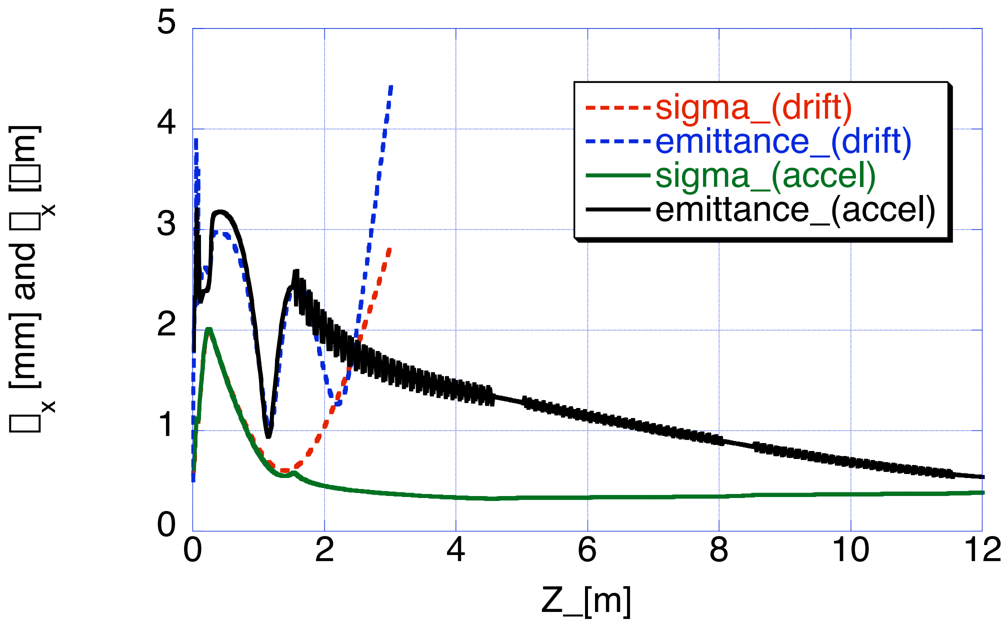

Figure 3.1. *HOMDYN simulation of SPARC injector transverse rms beam size and normalized emittance, in two TW linac configuration. Thermal emittance of 0.3 mm-mrad is assumed; additional focusing is provided around the first linac.*

3.4 START-TO-END SIMULATIONS

A start-to-end simulation of the beam dynamics from the injector through transfer line and undulator system has been performed by means of the codes PARMELA and GENENIS to quantitatively explore the expected performances of the injector systems in driving the SPARC FEL experiment. We take as our example the most conservative system that is to be encountered, one with no velocity bunching, and a relatively low energy of 155 MeV (consistent with either low gradient, three TW section operation, or high gradient, two TW section operation).

3.4.1 Start-to-end: choice of operating point

As the SPARC injector the first one driving a saturating FEL without the use of a compressor scheme — either chicane or velocity bunching — the FEL demands concerning the beam current have moved the design towards the limits of the state-of-the-art for pulse charge and pulse shape. In order to reach the goal with a good level of confidence we have explored a range of parameters that are not far from the previous best performances obtained in photoinjector labs. At present the best experimental results [22] give for a flat pulse with a FWHM=9 psec an emittance of 1.2 mm-mrad at Q=1 nC and an emittance of 1.5 □m at Q=1.2 nC, as seen in Fig. 3.2. Keeping in mind these we restricted the studies of operating point to a region of charge between 1-1.2 nC and a range of pulse lengths of 9-10 psec (FWHM). A detailed parametric investigation of these options of was performed using PARMELA code.

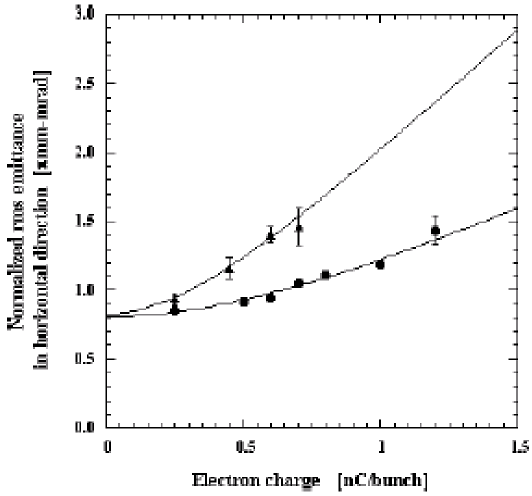

Figure. 3.2 *Measured normalized emittance versus bunch charge for two temporal pulse distribution: gaussian (triangle) and square (dot) pulse shapes at pulse length of 9 psec FWHM, from Ref. 8.*

Starting from the parameters optimised for the original SPARC working point at 85 A, the best performance in terms of increasing final current, which in the range of the SPARC FEL has been found to be the key parameter for shortening the FEL gain length [23] was obtained by means of scaling approach in which more charge is launched from the cathode. The preservation of the beam plasma frequency requires that the spot size be scaled according to $□_x \quad (Q/□_z)^{1/2}$, as indicated in Table 3.1. In the study, for all cases a thermal emittance linearly increasing with the radius and equal to 0.3 □m/1 mm of radius was assumed, as was a rise time of 1 psec (derived from previous optimization studies).

The results of this study are summarized in Table 3.2 where the configuration that meets the requirement with the minimum emittance has been deduced. It corresponds to a working point with 1.1 nC and a pulse length of 10 psec. In all cases a slice length defining the slice emittance and current of 300 μm has been considered.

Table 3.1. *Range of parameters for working point optimization studies.*

Q(nC)	τ(psec) FWHM	Laser spot radius (mm)
1	11.7	1
1	10	1.08
1.1	10	1.13
1.2	10	1.2
1	9	1.14
1.1	9	1.2

Table 3.2. *Summary of PARMELA results exceeding 100 A in 50% beam working point.*

Q (nC)	τ(psec) FWHM*	Beam fraction with I ≥ 100 A	ε_n (μm)	Total rms energy spread	Max. slice rms energy spread**
1	11.7	0% (max. slice current ≈92 A) (average bunch current ≈86 A)	0.6	0.002	0.0005
1	10	23% (max. slice current ≈102 A) (average bunch current ≈94 A)	0.67	0.00162	0.0005
1.1	**10**	**54% (max. slice current ≈110 A)** **(average bunch current ≈102 A)**	**0.75**	0.00165	0.00052
1.2	10	60% (max. slice current ≈120 A) (average bunch current ≈110 A)	0.81	0.00166	0.00054
1	9	50% (max. slice current ≈110 A) (average bunch current ≈101 A)	0.8	0.00167	0.00042
1.1	9	58% (max. slice current ≈120 A) (average bunch current ≈110 A)	0.86	0.00167	0.00043

** rise time=1 psec, ** 85% of the particles*

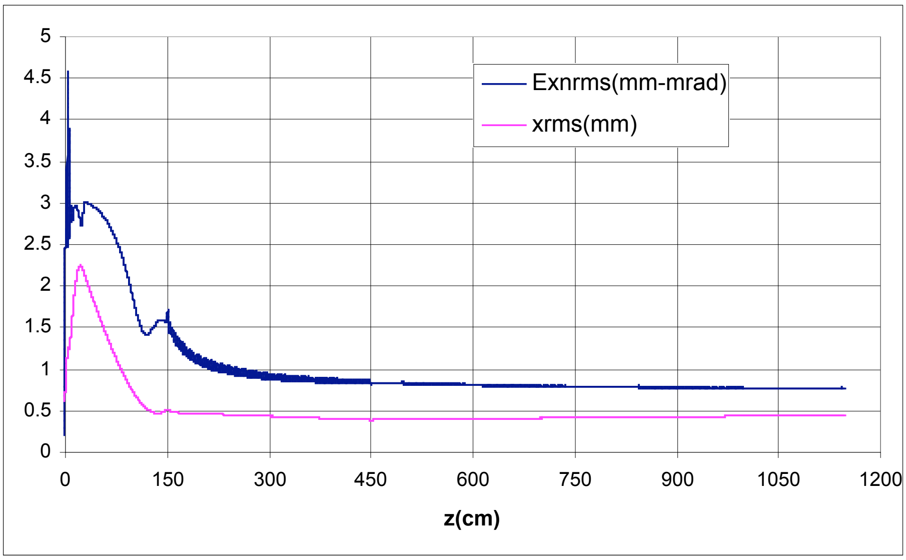

Figure 3.3. *PARMELA computed RMS normalized emittance and RMS horizontal envelope vs z from gun to the linac output for Q=1.1 nC, τ=10 psec, εth=0.34 mm mrad, laser spot radius=1.13 mm.*

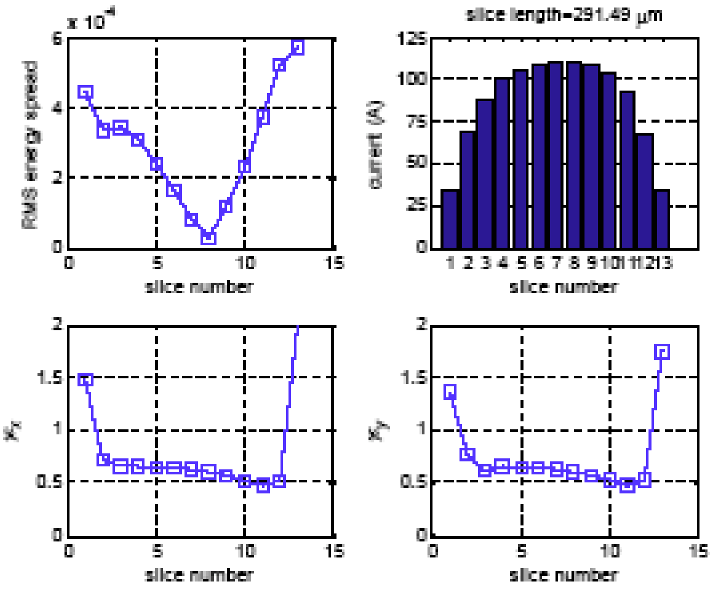

Figure 3.4. *Computed slice parameters for Q=1.1 nC, τ=10 psec.*

One can observe from the Table 3.2 that it is not convenient to work with 9 psec pulse length. This is due essentially to the fact that the higher aspect ratio increases the debunching longitudinal forces [23]. A pulse length of 10 psec allows the reaching the SPARC-FEL goal without increasing the charge over the limits of the state-of-art in high brightness guns of similar design.

In Figure 3.3 the rms norm. emittance and the rms envelope as a function of z from the gun to the linac output, as computed by PARMELA, are shown for the increased current working point. Note that scaling in the anticipated way from the parameters found for the original 85 A working point (ϕ_{gun}=33°, B_{sol}= 2.73 kG, and average longitudinal fields in TW section 1 of B=750 G, E=25 MV/m, TW sections 2 and 3 E =12.5MV/m), preserves the emittance compensation scheme. The plots of Fig. 3.4 refer to the slice analysis for this case: 85% of the particles are in slices with an emittance smaller than 0.7 mm mrad, 54% have current ≥100 A and 70% have a current ≥90 A.

3.4.2 Start-to-end: transfer line and undulator matching optics

A detailed analysis of the transfer line (TL) and the matching conditions to the undulator optics has been explored in Ref. [24]; its main conclusions of will be summarized in the following. Two triplets are used to match the optical functions of the beam at linac exit to the values desired at the undulator entrance. This solution, as opposed to a doublet and a triplet configuration which was also suitable, has been chosen in order to assure the most flexibility to the line. A 0.7 m drift is left free after the first triplet to allow for the installation of a RF deflector for bunch length measurements, performed on a flag installed in the drift after the second triplet. To conserve space each quadrupole is assumed to have a physical length of 10 cm.

Two cases have been studied at 155.3 MeV and 200 MeV, with correspondingly different values of the beam optical functions and emittance at the linac end. In Table .33 the beam the main TL parameters are summarized.

In Figure 3.5, the behavior of β_x and β_y from the end of the linac (corresponding to z=0 in the plot) to the undulator input is plotted. The peak horizontal beam size is in Fig. 3.6. The matching has been performed including the focal effects of 6 undulator sections interleaved by small horizontally focusing quadrupoles. The effect of each undulator section on the beam has been simulated as a vertically focusing quadrupole.

Table 3.3. *Injector-undulator transfer line optical characteristics.*

Energy (MeV)	155 – 200	**Max beam size (□)**	430
Length (m)	5.4	**Max □$_x$ (m)**	120
Number of 0.1 m quads	6	**Max □$_y$ (m)**	75
Max quad strength (m^{-2})	10	**Min □$_x$ (m)**	0.6
Max gradient (T/m)	10 – 13	**Min □$_y$ (m)**	0.2

The magnetic layout and quadrupole strengths for the 155 MeV case are summarized in Table 3.4, for the TL and the first undulator section (repeated 6 times). In both cases, 155 and 200 MeV, the average □ value in the undulator is between 1.5 and 2.0 m.

Table 3.4. *Transfer line magnetic characteristics.*

Element	L_{tot} (m) from Gun	Strength (m^{-2}) @ 155 MeV	G (T/m) @ 155 MeV	Strength (m^{-2}) @ 200 MeV	G (T/m) @ 200 MeV
Drift	12.	-	-	-	-
Q1	12.1	-11.4	-5.9	-11.	-7.4
Drift	12.25	-	-	-	-
Q2	12.35	15.	7.8	14.	9.4
Drift	12.5	-	-	-	-
Q3	12.6	-2.6	-1.4	-1.85	-1.2
Drift	15.55	-	-	-	-
Q4	15.65	-14.8	-7.7	-14.6	-9.7
Drift	15.8	-	-	-	-
Q5	15.9	18.3	9.5	14.	9.3
Drift	16.05	-	-	-	-
Q6	16.15	10.5	5.4	12.6	8.4
Drift	16.9	-	-	-	-

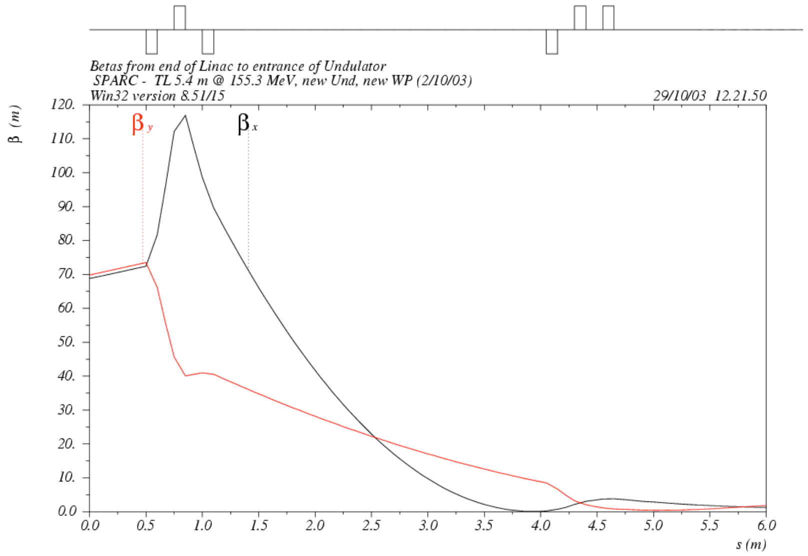

Figure 3.5. *Optical functions in meters (black horizontal, red vertical), for the 155 MeV case, from the linac output to the undulator input (z=0. corresponds to 11.5 m from the gun).*

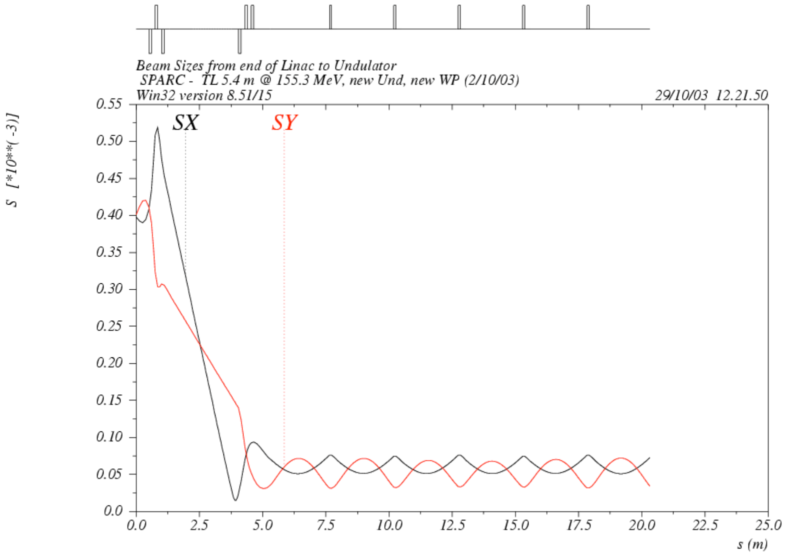

Figure 3.6. *Beam sizes in mm (black horizontal, red vertical) for the 155 MeV case, from the Linac output to the undulator output. The normalized beam emittance is 500 □m.*

The calculations of the matching parameters have been performed using the MAD code that does not take into account space-charge forces. In order to check the matching and to evaluate the effects of space-charge in the transfer line, the beam dynamics from the gun up to the undulator entrance for the nominal start-to-end configuration has been computed by using PARMELA, switching on and off the space charge computation. In Fig. 3.7 the behaviour of the normalized rms emittance and rms envelope in the *x* and *y* planes are shown as computed by PARMELA with space-charge included.

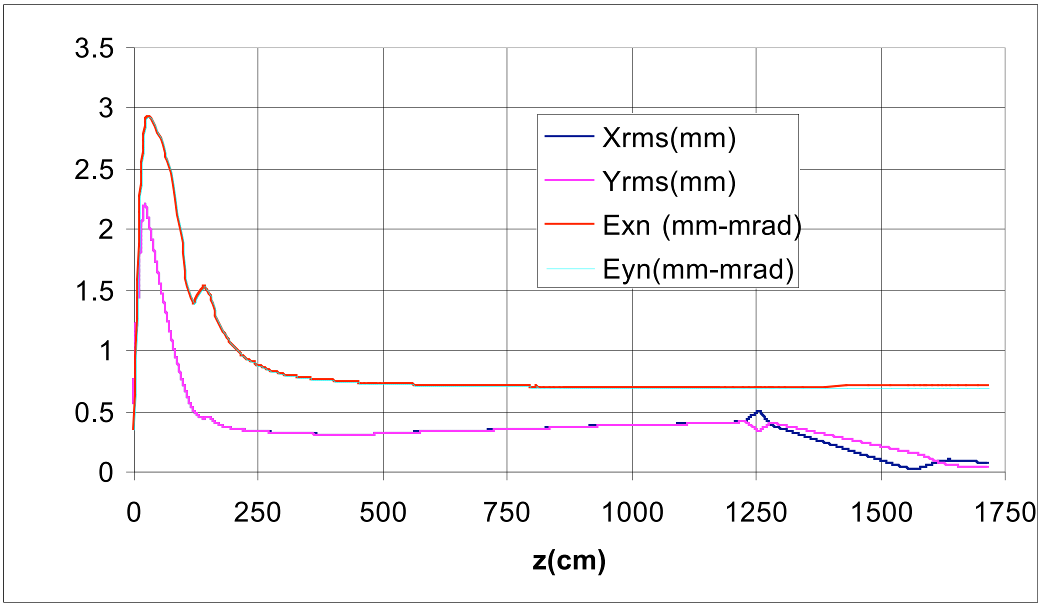

Figure 3.7. *Horizontal and vertical rms normalized emittances and envelopes from the gun to the undulator entrance.*

Figure 3.8 shows the beam phase space at the end of the TL with space charge on and off. One can see that when the space charge is off the agreement between the ideal values and the values given by the tracking is within 15%, while the mismatching increases when the space charge effect is taken into account: in particular the mismatching affects the Twiss parameters $\square_x$ and $\square_y$.

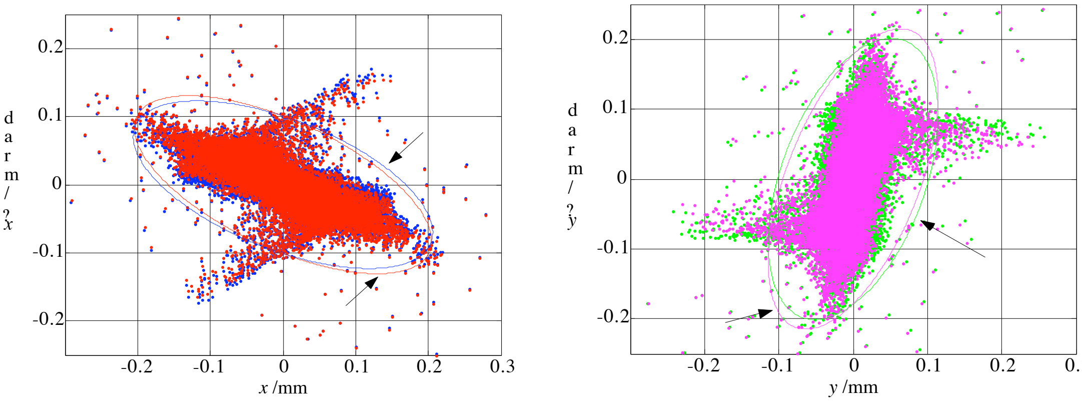

Figure 3.8. *(Left) PARMELA computed x-x space at the end of the TL with the space charge on (red) and off (blue) in the TL. (Right) The y-y' phase space at the end of the TL with the space charge on (green) and off (purple) in the TL.*

These results refer to the whole beam, but the single longitudinal slices in general do not have the same Twiss parameters of the whole bunch. Therefore a slice analysis has been carried out in order to evaluate the mismatching of the single slices of the bunch. In this analysis the slice length has been taken equal to approximately one cooperation length (~300 μm). The results are shown in Fig. 3.9 where the x and y Twiss parameters and the relative mismatching parameters $M = 0.5(\beta_o\gamma - 2\alpha_o\alpha + \gamma_o\beta)$, ($\alpha_o$, β_o and γ_o are the undulator matched parameters), are plotted in function of the slice number: one can see that 85% of the beam has a mismatching parameter lower than 1.2.

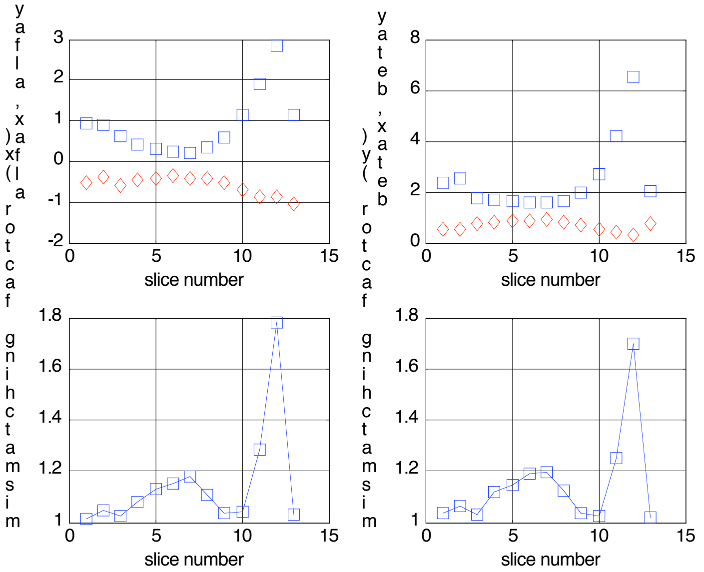

Figure 3.9. *Upper plots: Twiss parameters vs. slice number. Lower plots: x and y mismatching parameter vs. slice number.*

3.4.3 Start-to-end: SASE FEL simulations

The undulator parameter set used for the simulation of the SPARC SASE FEL are those of Ref. [25] and are summarized in the following table

Table 3.5. *Injector-undulator transfer line optical characteristics.*

Period	2.8 cm
Number of Periods/section	77 (+1 for phase matching)
Number of Sections	6
K	2.145

FEL simulations based on average beam parameters have been analyzed in Refs. [26] and [25]. In this section we summarize the results of a "start-to-end" (STE) simulation obtained starting from the phase space generated by PARMELA after transporting the beam through the injector, the linac, the transfer line, until the entrance of the undulator [27]. The beam phase spaces have been described in detail in the previous section (and in ref. [27]). As also anticipated in the previous section the beam optics in the undulator is realized taking advantage of the natural vertical focusing of the undulator itself. The matching conditions have been calculated by imposing that the vertical and horizontal beta functions are equal each other when averaged over one lattice period, and that the sum $\langle \beta_x \rangle^2 + \langle \beta_y \rangle^2$ is minimized. The simulation has been performed using GENESIS 1.3 [28] in time dependent mode. In Fig. 3.10 the RMS electron-beam size is shown along the undulator.

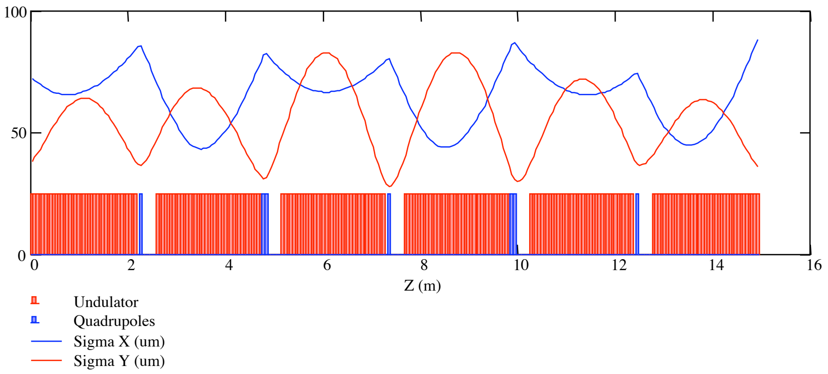

Figure 3.10. *RMS electron-beam size as a function of* z *in undulator.*

.

The beam propagated by PARMELA appears slightly mismatched with respect to the ideal case and the effect of this mismatching is the cause of the x-y asymmetry in the transverse RMS. In Fig. 3.11 the FEL power as a function of z is shown. The saturation length is shorter than 9 m. In Fig. 3.12 shown the radiation power spectrum with the typical spiking of SASE FEL light is displayed.

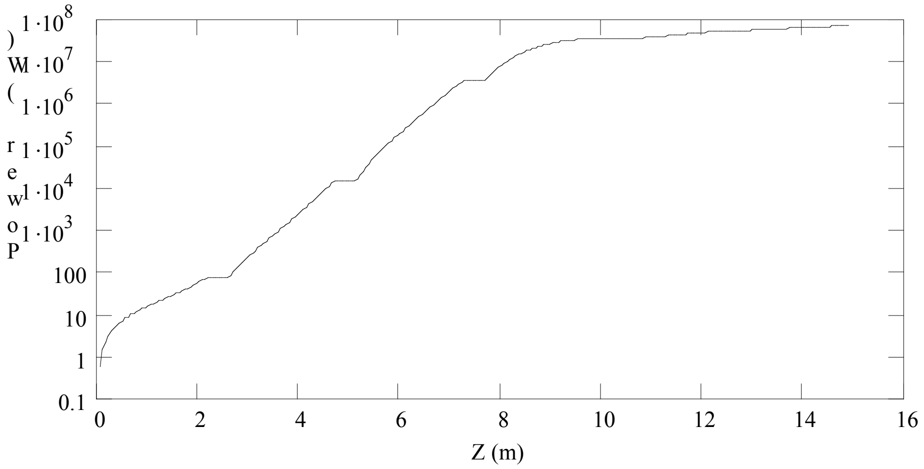

Fig. 3.11 *Power vs. z for the SPARC FEL, from GENESIS (final step in STE) simulation.*

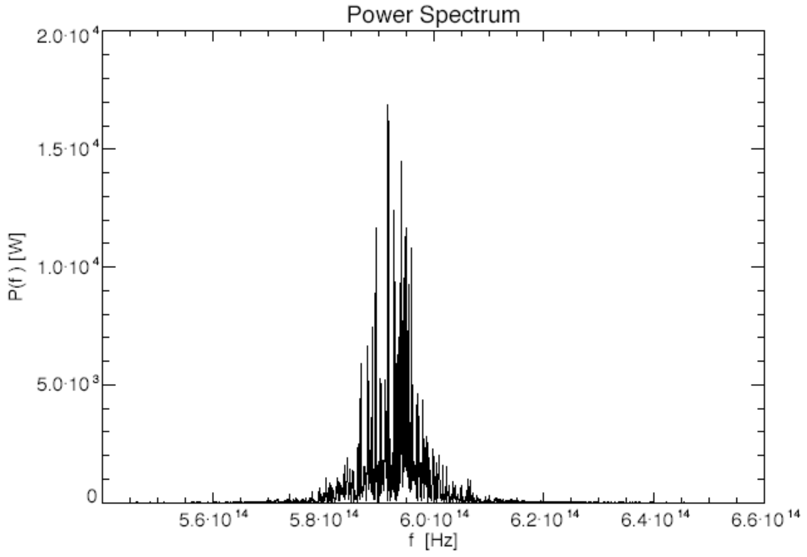

Fig 3.12*. SPARC final power spectrum, from GENESIS (final step in STE) simulation.*

STE simulations have been extremely precise in reproducing experimental data from other experiments and VISA is one of the main examples [see e.g. 29]. However we note that the STE simulation presented in this section has not been run in an attempt to reproduce a concluded experiment, but with the intention to anticipate the results of an experiment yet to be done. There is an important difference between these two situations. We have indeed to stress the fact that the electron beam has been "numerically" generated in ideal conditions, with an ideal laser pulse, from an ideal cathode and with all the parameters defining the configuration perfectly optimized. The contingency of more than 4 meters of undulator resulting from an analysis of Fig. 3.11 gives a reasonable margin of operation, but starting from this ideal configuration an analysis of the FEL performances degradation due to the mismatch of different parameters will be the topic of forthcoming investigations.

3.5 PARAMETRIC SENSITIVIES

One of the major goals of the SPARC project is to experimentally explore the stability and robustness of the ultra-high brightness beam/SASE FEL systems. In order to appreciate how the performances of the systems are degraded by standard laboratory errors, jitters and uncertainties, one must analyze the systems with detailed models [30]. In this section we discuss the results of such studies performed thus far [31]. There are two classes of parameters that we have studied. The first class bears directly on the efficacy of the emittance compensation process, and includes: laser beam spot size and ellipticity, rf field amplitude and phase errors, and solenoid field errors. Because of their primary importance, we have chosen to explore the variation of all of these quantities together, to set a boundary on the expected performance of the entire device, including the FEL in the end.

Other issues, are not as simple to parameterize, such as cathode emission uniformity, and laser time structure, and are discussed separately. In addition, the studies are presently being expanded to include the effects laser centroid offset in a more systematic way [32].

3.5.1 Tolerances and sensitivity to errors

In order to investigate the stability of the SPARC working point and to predict the most probable values of the projected and slice emittance in realistic conditions a sensitivity study to various types of random errors, as listed above, in the SPARC accelerator was performed. The study was divided in two steps. In the first step the tolerances of the main tuning parameters were set with the criterium of having a maximum increase of the projected emittance of 10% respect to the nominal case (0.71 mm mrad). In the second step the errors were combined in the defined tolerance ranges and a statistical analysis has been performed in order to study the effect of the combination of errors on the projected and slice emittance and on the mismatching at the entrance of the undulator.

3.5.2 Setting of tolerances

The sensitivity of the projected emittance to errors of individual parameters that can fluctuate during the machine operation was studied by extensive simulations with the PARMELA code. The parameters that have been considered are:

1. the gun phase (32° for the nominal case)
2. the beam charge (1.1 nC for the nominal case)
3. the emittance compensation solenoid magnetic field (2.73 kG in the nominal case)
4. the gun electric field amplitude (120 MV/m for the nominal case)
5. the spot size (radius=1.13 mm for the nominal case)
6. the spot ellipticity ($x_{\max}/y_{\max}=1$ for the nominal case)

The reference case of 10 psec FWHM, 1.1 nC beam with a laser pulse rise time of 1 psec (see discussion below on the setting of this parameter) and a thermal emittance of 0.34 mm mrad was considered. A systematic scan of each parameter was performed around the optimized working point reference value in order to derive the minimum variation of each parameter giving an increase of emittance of 10%. The results of these scans are shown in the plots of Figures 3.13-3.18.

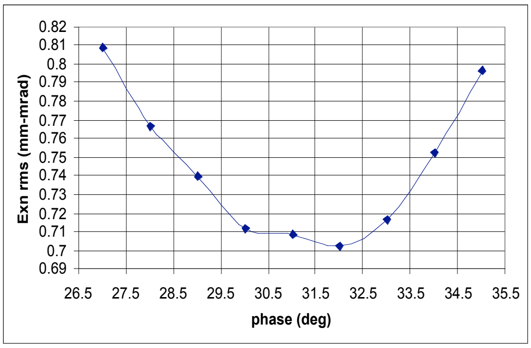

Figure 3.13 *Emittance vs phase-jitter(Q_0=1.1 nC)*

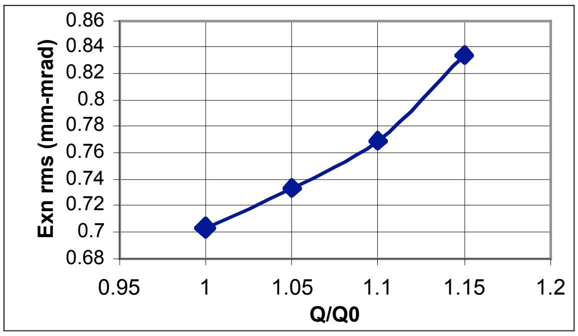

Figure 3.14 *Emittance vs charge fluctuation*

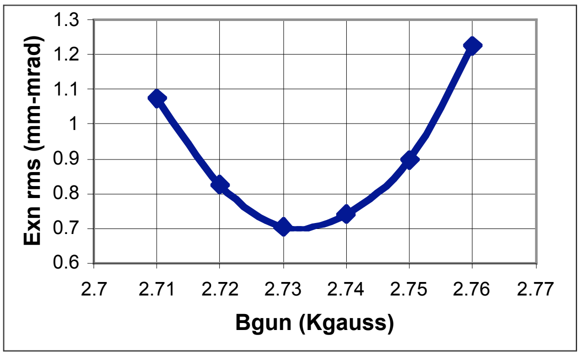

Figure 3.15 *Emittance vs gun magnetic field*

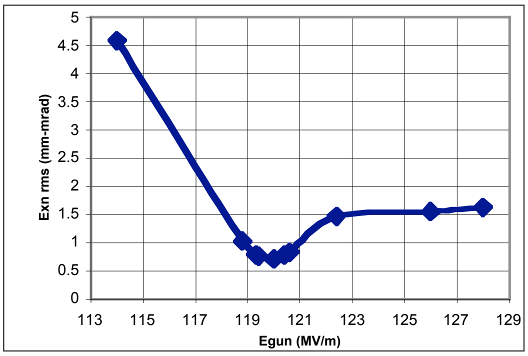

Figure 3.16 *Emittance vs gun electric field*

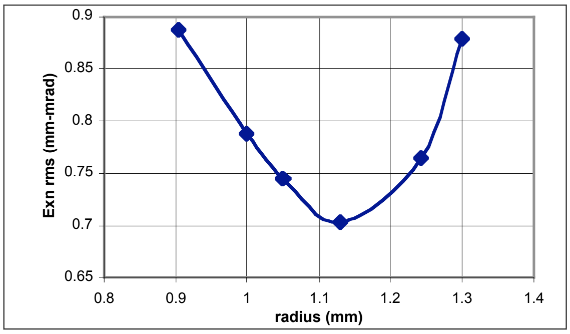

Figure 3.17 *Emittance vs spot radius*

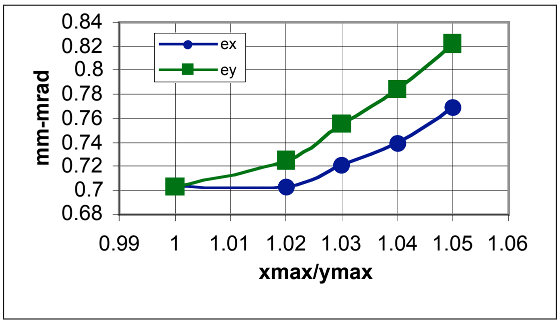

Figure 3.18 *Emittance vs ellipticity* ($x_{max}y_{max}=R^2$)

The resulting tolerances on the different tuning parameters are listed in Table 3.6.

Table 3.6. *Minimum variation of the single parameters value for a 10% emittance increase*

Phase jitter	± 3°
Charge fluctuation	+ 10%
Gun magnetic field	± 0.4%
Gun electric field	± 0.5 %
Spot radius dimension	± 10%
Spot ellipticity	3.5% (x_{max}/y_{max}=1.035)

It can be seen that the most critical parameters are the electric field amplitude and the spot ellipticity.

3.5.3 Statistical study of sensitivity to combined errors

One hundred PARMELA simulations runs have been performed, each with errors set randomly within the tolerance limits. In particular PARMELA was interfaced with a MATLAB based program that accepts in input the limits of variation of the single parameters and generates a number of input files in which the six parameters of our interest are varied randomly in the pre-defined ranges according with the sampling technique of the “latin hypercube”, as this algorithm is implemented in MATLAB statistical toolbox.

The numbers used are uniform distributions with average values and rms widths listed in Table 3.7. The interval of errors distribution is ± 3 □ around the average value.

Table 3.7. *Variation of parameters for combined tolerance study of errors in SPARC gun.*

Parameter	**Average value**	**RMS**
Gun phase	31.5°	1.74°
Charge	1.15 nC	0.032 nC
Gun magnetic field amplitude	2733 Gauss	5.8 Gauss
Gun electric field amplitude	119.9 MV/m	0.32 MV/m
Spot radius	1.132	0.068 mm
Ellipticity	1	0.02

PARMELA beam dynamics simulations gave the sensitivity of projected and normalized emittance to such types of errors. The results of the simulations were used to construct the curve plotted in Fig. 3.19(a) that gives the probability to obtain an emittance greater or equal than the corresponding value on the abscissa: for example the probability to get a normalized projected emittance ≥ 1 mm mrad is around 10%. The histogram in Figure 3.19(b) gives the distribution of the emittance values that has an average value of 0.86 mm mrad and a rms value of 0.1 mm mrad. The histogram follows a Poisson distribution indicating the independent nature of the results.

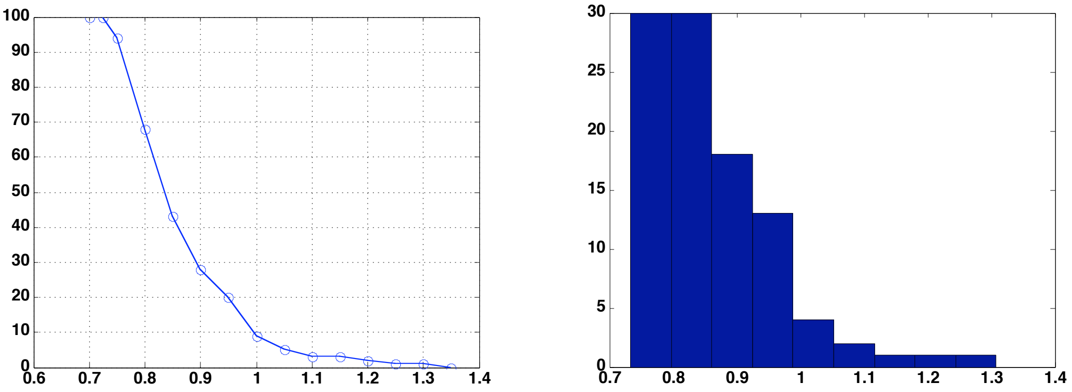

(a) (b)

Figure 3.19 *(a) Probability vs emittance plot over 100 simulations (b) Histogram of the emittance over 100 simulations*

Concerning the slice emittance, in the 100 simulations it does not exceed 0.9 mrad for the 9 central slices out of 13 slices, as it can be seen in Fig. 3.20 in which two extreme cases obtained from error study simulations results are compared with the computed ideal case.

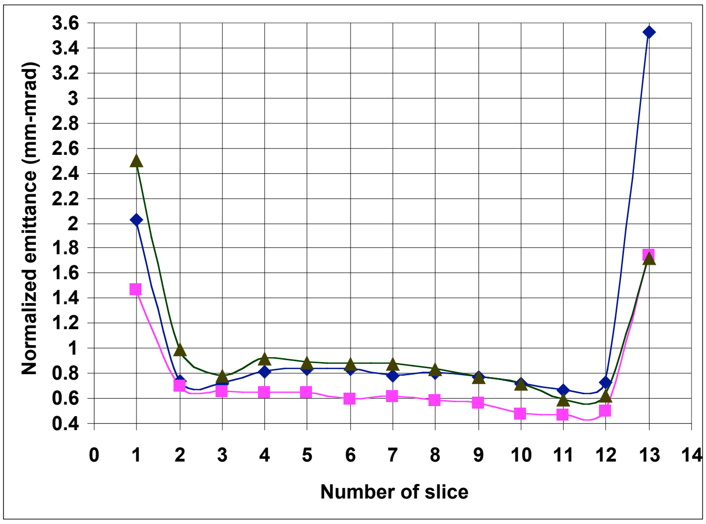

Figure 3.20 *Interval of variation of slice emittance over 100 simulations*

On the basis of error study it can be concluded that combining multiple errors on tuning parameters the projected and slice emittance values remain within the limits of the SPARC design (2 mm mrad for the projected emittance and 1 mm mrad for slice emittance).

The effect of random errors on the transverse phase space orientation at the entrance of the undulator has also been investigated. In Fig. 3.21(a) the distribution of the mismatching factor defined as $M = \frac{1}{2}\cdot\left(\beta_0\gamma - 2\alpha_0\alpha + \gamma_0\beta\right)$ where α_0, β_0 are the matched values at the entrance of the undulator is shown: 1.3 and 0.32 are respectively the average and the rms values. The mismatched ellipse corresponding to M=1.3 is compared to the ideal matched ellipse (M=1) in Fig. 3.21(b).

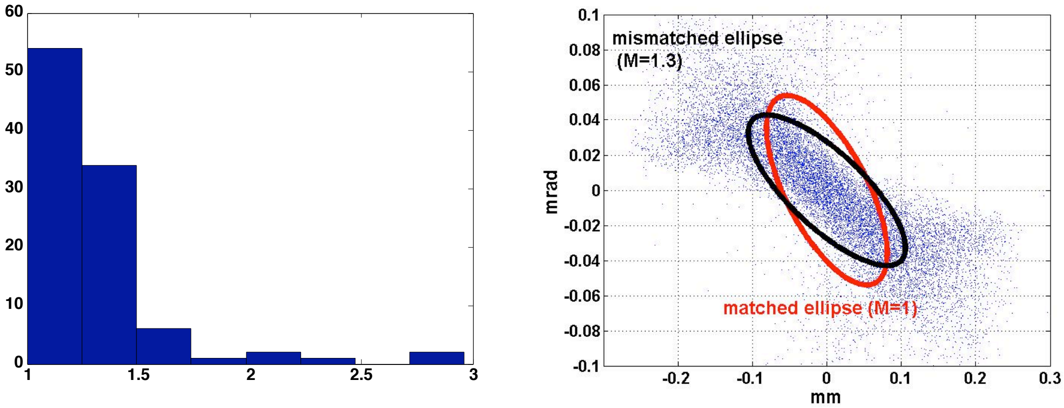

(a) (b)

Figure 3.21 *(a) Histogram of mismatching factor over 100 simulations (b) Comparison of two transverse phase spaces corresponding to M=1 and M=1.3 mismatching factor values*

3.5.4 Cathode emission inhomogeneities

The issue of cathode quantum efficiency/laser non-uniformity is somewhat more difficult to quantitatively describe than the simple parameters of spot-size and ellipticity. The effects of cathode's inhomogeneities [33] have been tested by simulating, using TREDI's powerful 3D field calculations, a zone on the cathode with reduced quantum efficiency. We assumed a circular spot (a "hole") with a surface S~10% (R~316 μm) of the nominal spot centered half-way of the spot nominal radius (x=0.5 mm, y=0.0 mm). Simulations were made as above ($5\cdot 10^4$ particles, SC fields evaluated on a

$20(n_x) \times 20(n_y) \times 30(n_z)$ 3D mesh) using the following parameter set: gun peak field *E*=140 MV/m, *B*=3.09 kG focusing solenoid strength, 10 ps laser pulse duration. Figures 3.22) and 3.23 show respectively the *x-y* space at extraction ($z = 0$) for $Q_E = 50\%$ and the emittance degradation as a function of Q_E. The results suggest that localized inhomogeneities do not dramatically degrade the emittance, for it grows by $\Delta\varepsilon_{x(y)} \approx 10\%(15\%)$ for $Q_E = 70\%$. This analysis will be further extended to the cases of randomly distributed ("spotty") inhomogeneities, which better describe the behavior of real cathodes.

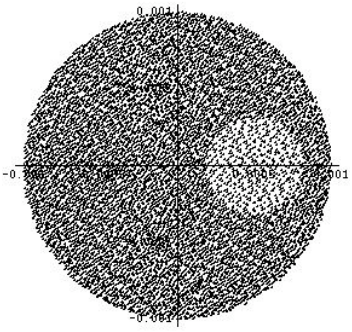

Figure 3.22*: The x-y space at extraction (z=0) for* $Q_E = 50\%$.

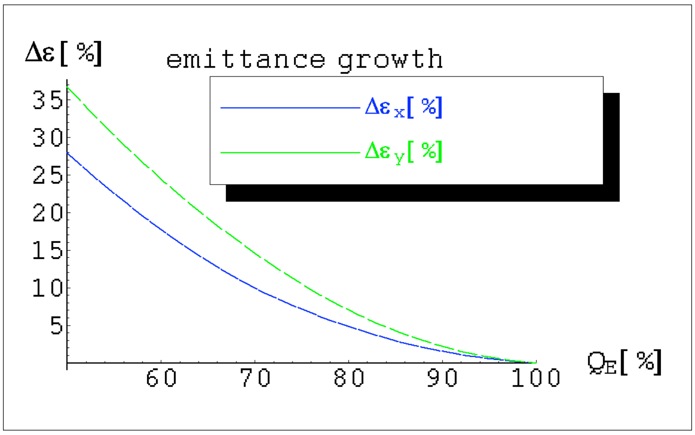

Figure 3.23: *Emittance growth as a function of* Q_E

3.5.5 Sensitivity to Laser Rise Time and Time Structure

The electron beam's final characteristics strongly depend not only on the spatial uniformity of beam emission induced by the laser, but also the temporal laser pulse shape. In order to optimize the characteristics of the electron beam, shaping of both phase and amplitude of the light pulse is required. We report in this section beam dynamics simulations concerning the effects of temporal characteristics of the driving light pulse for optimal performances of the electron RF gun. PARMELA has been used for this analysis. This study was performed some time ago to set the laser requirements, and thus employed the original set of SPARC parameters. The conclusions reached are not significantly impacted by the small change in parameter sets.

The studies on the temporal pulse shaping are particularly interesting. It is well known that the lowest beam emittance can be obtained if the laser pulse is uniform in time, with short rise/fall times [22]. The simulations reported in Fig. 3.24 refer to a temporal pulse length of 11.65 ps FWHM, they show that the normalized projected emittance deteriorates as the laser pulse rise time increases. As results from these studies, flat top pulses with rise times shorter than1 ps are required in order to avoid emittance degradation.

As discussed in the upcoming laser section, laser pulse shaping with short rise time may result in the formation of longitudinal ripples. Therefore, the effect of a laser pulse with longitudinal ripples has been investigated and compared to a plain square pulse with no ripples. We have performed beam-dynamics simulations with a temporal pulse length of 11.65 ps FWHM, 1 ps of rise time and we have assumed the presence of ripples in the longitudinal distribution, having 10% and 30% of the nominal amplitude, as shown respectively in left and right plot of Fig. 3.25. The beam is assumed to be transversely uniform in these studies. The striking result is that even with a 30% of longitudinal irregularity the beam emittance does not appear to be strongly affected. This result is displayed in Fig. 3.26, where it is evident that the presence of ripples does not affect either the emittance or the rms beam envelope. This is clear also from Table 3.8, where the emittance value is moreover constant for the three reported cases.

This result can be interpreted as if the space-charge force induces a compensation of the longitudinal irregularity. This hypothesis is justified by PARMELA simulation results. In Figs. 3.27-3.30 the longitudinal beam distributions along the beam line are displayed. At the cathode the temporal spectrum has a 30 % ripple overlapped on a square pulse, the relative energy spread is zero. As the beam goes through the gun and drifts the temporal oscillations transform in energy oscillations. At the entrance of the first acceleration structure (at *z*=150 cm) the beam has lost the temporal ripples, which have converted into energy variations through a fractional plasma oscillation. These energy ripples do not have any notable effect to the rms energy spread at the end of the linac, as they are soon suppressed inside the first accelerating structure.

These results indicate that the shape of the laser pulse should be square with a very small rise time, whereas a smooth temporal profile in the "flat-top" region of the pulse is not a stringent requirement.

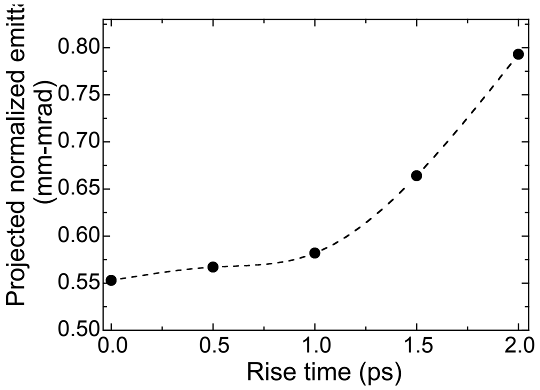

Figure 3.24: *Normalized projected emittance vs rise time, calculated for thermal emittance of 0.3 μm and an electron beam of 1 mm radius (with uniform transverse distribution).*

Table 3.8*. PARMELA simulation results: emittance after second RF accelerating structure versus longitudinal beam profiles.*

Beam distribution	emittance [mm mrad]
Square pulse 1ps rise time	0.580
Square pulse 1ps r.t. and 10% ripple	0.576
Square pulse 1ps r.t. and 30% ripple	0.616

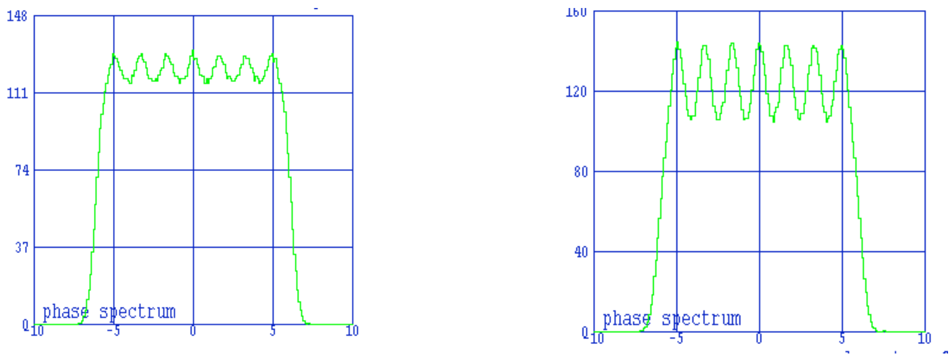

Figure 3.25 *Longitudinal beam distribution with ripples, with 11.65 ps FWHM of temporal pulse length and 1ps of rise time. Left (right) plot: 10% (30%) amplitude irregularity.*

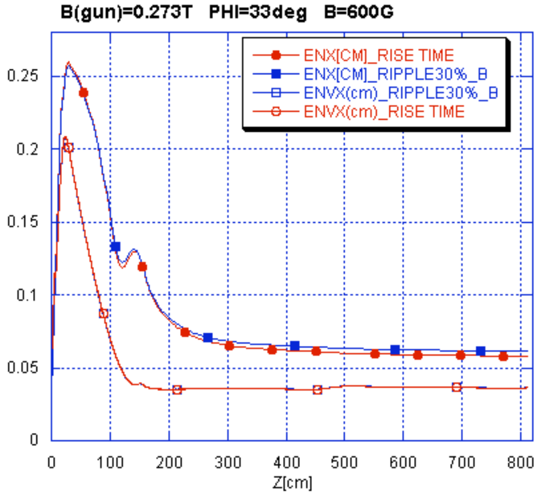

Figure 3.26 *Beam emittance and envelope with (blue squares) and without (red dots) 30% in amplitude longitudinal ripples: there are not significant changes for the two cases. These PARMELA simulations have been performed for a square pulse with 1ps of rise time , a solenoidal gun field of 0.273T, 33° RF of injection phase and solenoidal field at the first RF structure 600G.*

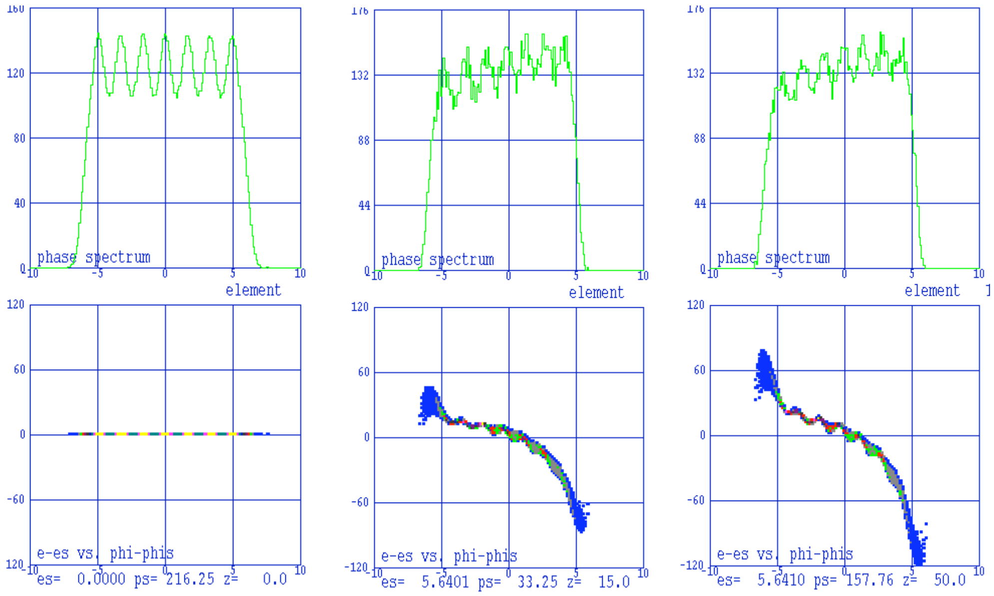

Figure 3.27*: Longitudinal beam distribution: phase and energy spectrum in the upper and lower plots, respectively. Left plot: initial distribution at cathode (z=0 cm); middle plot: at the end of RF gun (z=15cm); right plot: beam at z=50cm.*

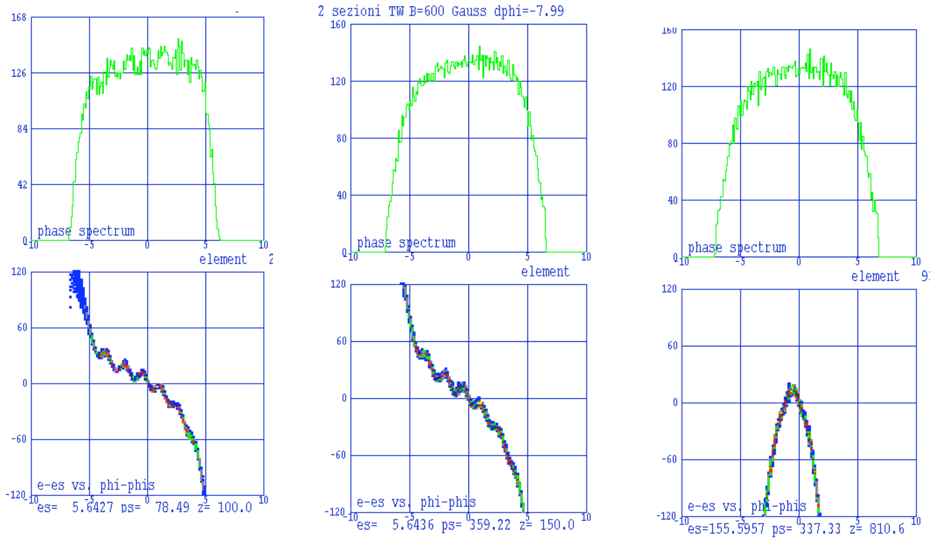

Figure 3.28: *Longitudinal beam distribution: First left plot: z=100 cm; second plot: at the entrance of first RF structure (z=150cm); right plot: at the end of second RF structure z=810cm.*

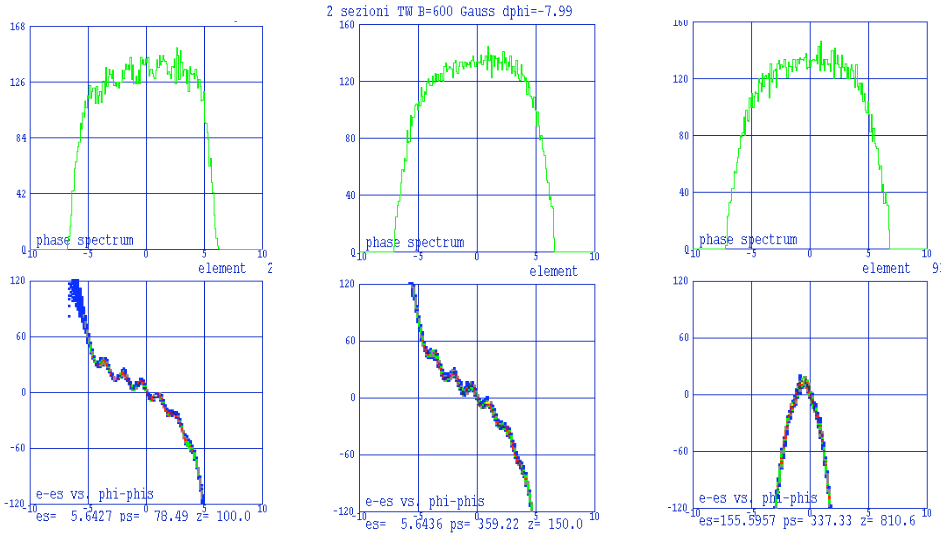

Figure 3.29: *Energy distribution at different longitudinal positions: Left plot: at cathode (z=0 cm); middle plot: at the end of RF gun (z=15cm); right plot: beam at z=50cm.*

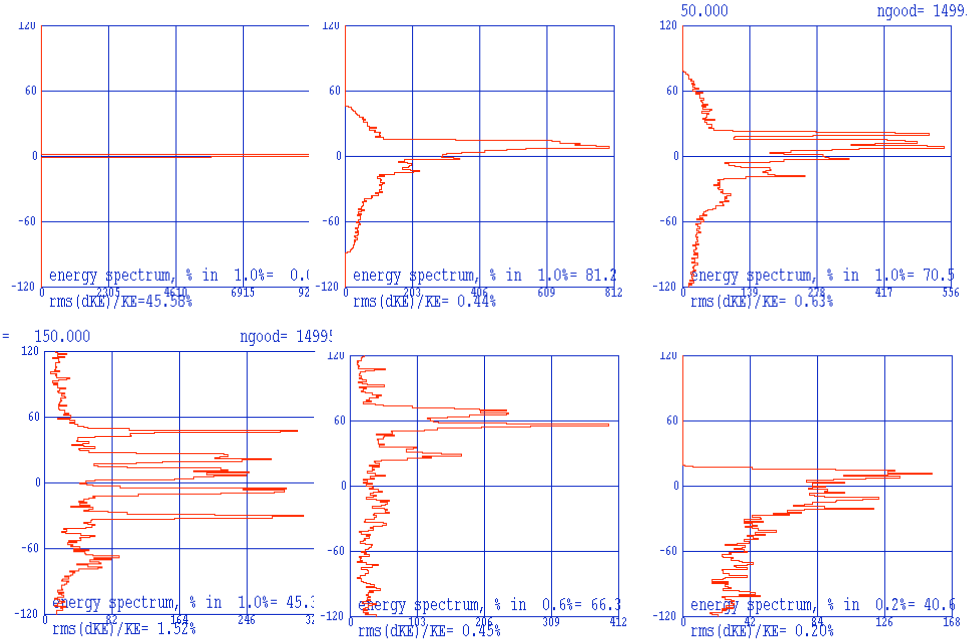

Figure 3.30: *Left plot: entrance of first RF structure (z=150cm); middle plot: energy oscillations at z=300cm; right plot: at the end of second RF structure, z=810cm.*

3.5.6 Sensitivity to Laser Pointing Stability

As discussed in the photocathode laser section below, the long optical transport line of the UV radiation from the laser room to the photo-cathode may produce a misalignment of the beam that gives rise to cathode illumination jitter. Simulations and experimental results at VISA FEL (@600 nm) show that for optimal FEL performance the trajectory walk-off in the undulator should not exceed an rms beam size in a gain length [34]. In our case the rms beam size at the undulator entrance is 60 μm and the gain length is L_g ~ 0.7 m. The requirement of laser pointing stability less than 60 μm may not be the right answer, since the original beam offset could be magnified during the acceleration and transport along the transfer line (it would be in fact demagnified considerably if one naively employs linear optics analysis). The beam line is in fact optimized for a space-charge dominated beam dynamics while the centroid of the bunch behaves as a single particle. Because no space-charge force is acting on it, is "over-focused" by the emittance-compensating optics. In addition the beam divergence at the entrance of the undulator has to be less than 57 μrad to prevent walk-off in the undulator.

A preliminary study of this effect has been done by the code HOMDYN. In Fig 3.31 the beam envelope is shown along the beam line, from the gun up to the entrance of the undulator, together with the bunch centroid evolution for two different initial offsets: 33 and 100 μm. The initial centroid offset of 33 μm (100 μm) becomes a 40 μm (120 μm) at the undulator entrance.

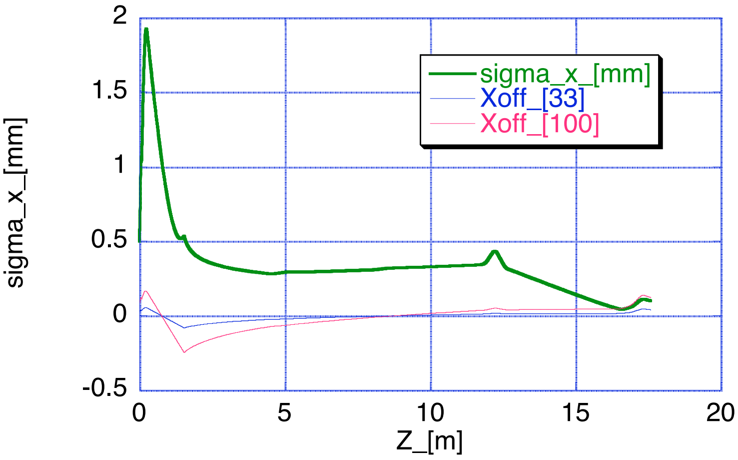

***Figure 3.31:** Beam envelope and bunch centroid evolution along the beam line for two different initial offsets: 33 and 100 μm in the horizontal plane.*

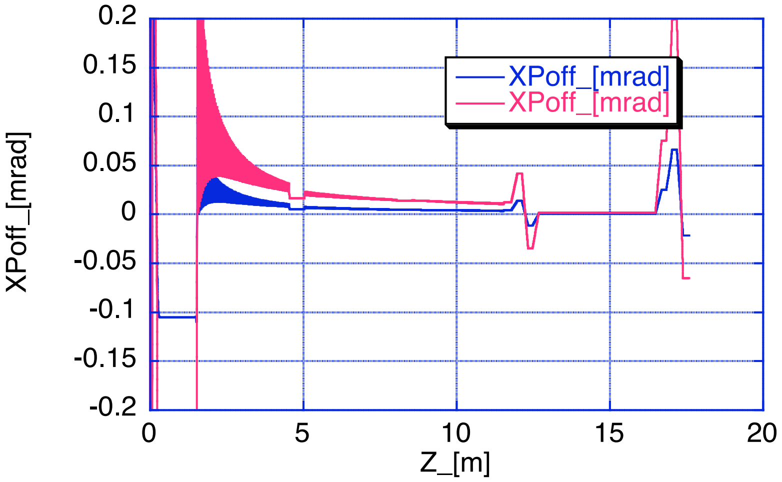

***Figure 3.32:** Beam centroid divergence X’ along the beam line for two different initial offsets: 33 and 100 μm in the horizontal plane.*

As expected the betatron motion of the centroid and of the envelope are out of phase due to the differentiating effects of space-charge: the centroid cross the axis the first time at z=0.8 m while the beam envelope is gently focused to a space-charge dominated waist at the entrance of the first linac section. In the linac the focusing effect of the solenoid around the first accelerating section reduces the centroid offset, but when the beam leaves the linac the centroid still has an angle that is increased by the last triplet before entering the undulator. Figure 3.32 shows the beam divergence x' for the two cases along the beam line. The 33 μm (100 μm) offset case enters in the undulator with a 20 μrad (65 μrad) divergence. We can conclude that a laser pointing jitter of 30 μm is suitable for our purposes.

Recent studies have indicated that with a careful treatment of tranverse wakefields, that the projected emittance may not be well preserved in the presence of misalignments. As the misalignments in question concern not only the laser, but the structures within the electron beamline as well, this subject in now undergoing further review.

3.6 SIMULATION PARAMETER LISTS

In order to provide a compact reference to the simulation inputs for the numerical work involved in the present SPARC beam dynamics design, we provide here a listing of the most relevant parameters employed in this work.

GUN

Charge	1.1	nC
Longitudinal pulse form	trapezoidal *	
FWHM e-beam duration	10	psec
Rise time	1	psec
Beam radius	1.13	mm
RMS thermal emittance	0.34	mm-mrad
RF frequency	2856	MHz
Number of cells	1.6	
Maximum extraction field	120	MV/m
Electron beam energy at exit	5.64	MeV
Phase**	32	°
Solenoid field	2.73	Kgauss
Solenoid centre	0.19	m

** stack of 13 gaussians*

*** cathode at z=0*

**** phase of the bunch centre*

LINAC

Number of sections	3	
Section length	3	m
First section solenoid field (a stack of 12 Helmoltz coils + an independently powered initial coil)	600 (in the 12 Helmoltz coils solenoid) 700 (in the initial coil)	Gauss
Centre of the initial coil	1.435	m
Centre of the first coil of the 12 Helmoltz coils solenoid	1.635	m
Position of the centre of the initial cell of the first section	1.535	m
Distance between the first cell centres of two adjacent sections	3598.77	mm
First Section accelerating field	25	MV/m
Second Section accelerating field	12.5	MV/m
Third Section accelerating field	12.5	MV/m
First section phase	(on crest)	
Second section phase	(on crest)	
Third section phase	(on crest)	

Beam parameters (*linac output*)

Output energy	155.3 MeV
Peak current	102 A
RMS Energy Spread	0.165 %
RMS Transv. Norm. Emittance	0.7 mm mrad
RMS Longitudinal Emittance	980 deg-KeV
$\square_z$	0.934 mm
$\square_x$	0.4 mm
$\square_{xy}$	67 m/rad
$\square_{xy}$	- 4

Slice parameters (*linac output*)

Slice length	300	□m
Slice energy spread	0.05	%
Slice RMS norm. emittance (average on 70% beam)	0.6	mm-mrad
Max. Slice current	110	A
Beam fraction with I≥100 A	54	%

TRANSFER LINE

Drift	L=0.5 m
Q1	L = 0.1 m, G = - 4.4353 T/m
Drift	L = 0.15 m
Q2	L = 0.1 m, G = + 9.3514 T/m
Drift	L = 0.15 m
Q3	L = 0.1 m, G = - 4.9916 T/m
Drift	L=2.95 m
Q4	L = 0.1 m, G = - 4.2539 T/m
Drift	L=0.15 m
Q5	L = 0.1 m, G = + 3.32819 T/m
Drift	L=0.15 m
Q6	L = 0.1 m, G = + 8.26156 T/m
Drift	L = 0.75 m

Total length= 5.4 m

UNDULATOR

Number of modules	6
Module length	2.156 m
Number of periods	77
Period	0.028 m
Magnetic length	12.936 m
Break length	0.392 m
Number of breaks	5
Effective length	14.896 m
Gap	9.58 mm (for □=500 nm)
K	2.144
q-pole length	5.4 cm
Drift before q-pole	5.7 cm
Drift after q-pole	28.1 cm
q-pole gradient	G= 5.44 T/m
Average □	1.516 m

Matched Twiss parameters at undulator entrance

□x	0.878
□x	2 m/rad
□y	-0.787
□y	0.68 m/rad

3.7 MODELLING OF DIAGNOSTIC SYSTEM BEAM DYNAMICS

The goals of the SPARC injector project require that sophisticate modeling and diagnostic approaches be undertaken jointly, in support of each other — the benchmarking of codes with experiments, and the illumination of the underlying beam dynamics by simulation. We now present some results of detailed modeling of concerning two of the more elaborate experiments planned for the SPARC injector program, the low energy slit-based emittance measurement, and the high energy dispersion-based slice emittance measurement.

3.7.1 Low energy emittance measurement simulations

The first phase of the SPARC project consists of the commissioning of the low energy section of the photoinjector system (5.6 MeV beam), with a systematic measurement of the emittance compensation process during the post-rf gun drift. This systematic study is intended to learn as much as possible about the critical low energy portion of the compensation process, where the emittance oscillations are most pronounced, and there is thus more risk in handling the beam. The most serious anticipated sources of non-ideal behavior in emittance compensation arise from non-uniform beam emission at the cathode, due to laser or photoemitter imperfections. To study the low-energy emittance compensation process in detail, before the areas needed for both propagation and diagnosis are occluded by a linac section, a dedicated, movable (in *z*) emittance-meter tool (Fig. 3.33) has been proposed for this phase. More aspects of this device, schematically shown in Fig. 3.34, are discussed further in the diagnostic section of this document.

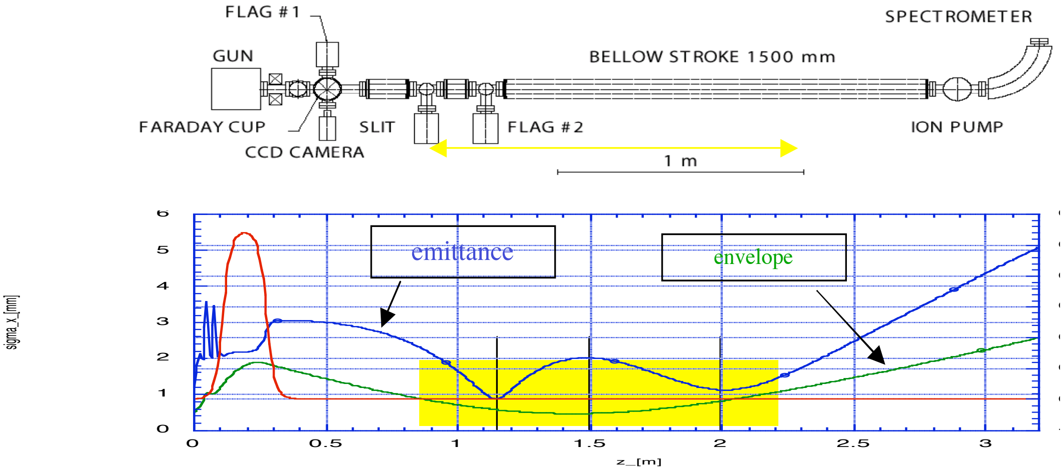

Figure 3.33: *Movable emittance measurement tools (upper picture); rms normalized emittance and envelope evolution from the cathode to the drift end (lower picture). The solenoid field (red line, lower plot) is also shown, and the yellow area represents the range of the movable emittance measurements.*

The emittance measurement in the drift after the SPARC photocathode gun will be based on the multislit technique, in which the beam is sliced into well-separated sampling beamlets by means of an intercepting mask (Fig. 3.34). The slits convert the space charge dominated incoming beam into several emittance-dominated beamlets that then drift to a detection screen. The intensity of beamlet spots on the screen is directly proportional to the number of particles in the beamlets which hit the screen. Numerical simulations of the measurement based on PARMELA beam dynamics calculation have been done in order to verify the optimization the device's mechanical measurement assembly parameters (slit width and spacing, distance between multislit mask and output screen) which may be chosen on the basis of analytical guidelines [35]. The simulations also serve to evaluate the effect of the residual space charge which has been minimized by the correct choice of the design parameters. They also check the possibility of retrieving the rms emittance in the range of interest.

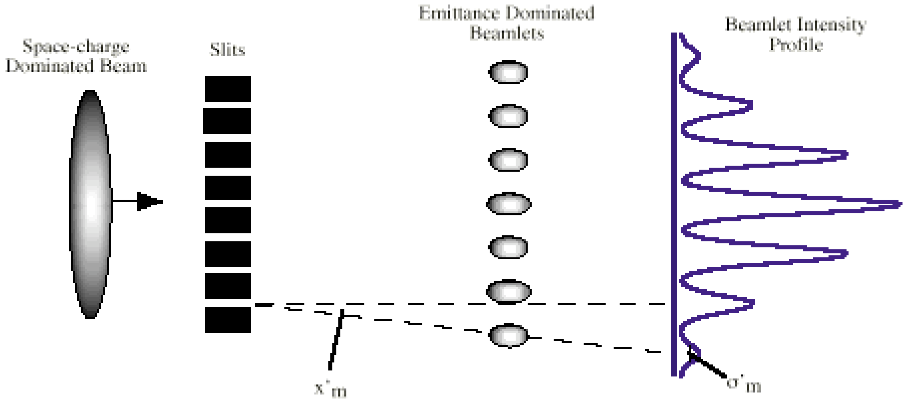

Figure 3.34: Multi-slit based emittance measurement scheme

In particular, we have developed two MATLAB-based programs. The first one generates a simulated output image by means of a density plot generated from the phase space distribution predicted by PARMELA, which is used to retrace each electron from before the slits up to the output screen. The second MATLAB program retrieves the phase-space parameters from the simulated image recorded by the first program on a TIFF file.

The formula used to find the rms emittance [36] employs only geometrical parameters of the slits and of the spots on the screen:

$$\varepsilon_n^2 = \langle x^2\rangle\langle x'^2\rangle - \langle xx'\rangle^2$$

$$\approx \frac{1}{N^2}\left\{\left[\sum_{j=1}^{p} n_j\left(x_{sj}-\bar{x}\right)^2\right]\cdot\left[\sum_{j=1}^{p} n_j\sigma_{x'_j}^{\ 2} + n_j\left(\overline{x'_j}-\overline{x'}\right)^2\right]-\left[\sum_{j=1}^{p} n_j x_{sj}\overline{x'_j}-N\bar{x}\overline{x'}\right]^2\right\} \tag{3.6}$$

where:

p = total number of slits
n_j = number of particles passing through j-th slit and hitting the screen (this is a practical weighting of spot intensity
x_{sl} = slit positions
$\overline{x}_j$ = mean position of spots on screen
$\overline{x}$ = mean position of all beamlets
$\overline{x}'_j$ =mean divergence of all beamlets
σ_j = rms size of spots on screen

The first step of the numerical simulation of the emittance measurement is the beam dynamics calculation in the SPARC region gun + drift. The plot of Fig. 3.35 shows the normalized rms emittance and rms x-envelope computed by PARMELA in this region. The temporal distribution of the 1 nC input beam is given by a pulse with a 11.7 psec width (FWHM) and 1 psec rise time, while the radial distribution is uniform. The particle coordinates are saved in a binary file along the drift at steps of 5 cm in order to have the possibility to introduce at different points of the drift an intercepting multi-slit mask, simulated by cutting the output PARMELA distribution. The surviving particles are traced in a successive run from the "cutting" point (the mask plane) up to the output screen.

For the simulation of the emittance measurement we begin with 450K simulation particles, in order to save, after the cut, a number of particles that can be sufficient for the successive computation that requires a large number of particles (50K at least), if one wants to take into account the residual space charge effect, noting that a 3D calculation is needed being the beamlets a collection of sheet beams.

Analytical considerations based on the envelope equation [35] applied to the SPARC beam (*I*□100 A, □□0.5 mm, □$_{msn}$ □ 1 mm-mrad) yield a slit width *d*< 75 □m in order to have an emittance dominated beam expansion after collimation. The slit spacing *w* has to be chosen much larger than the slit width and smaller than the beam size to ensure that the beam can be resolved (*d* < *w* < □). The drift length *L* between the slit plate and the output screen is a compromise between two considerations; it must be large enough to have a high resolution for the low beam emittance, but small enough to prevent the overlapping of the beamlet profiles on the screen.

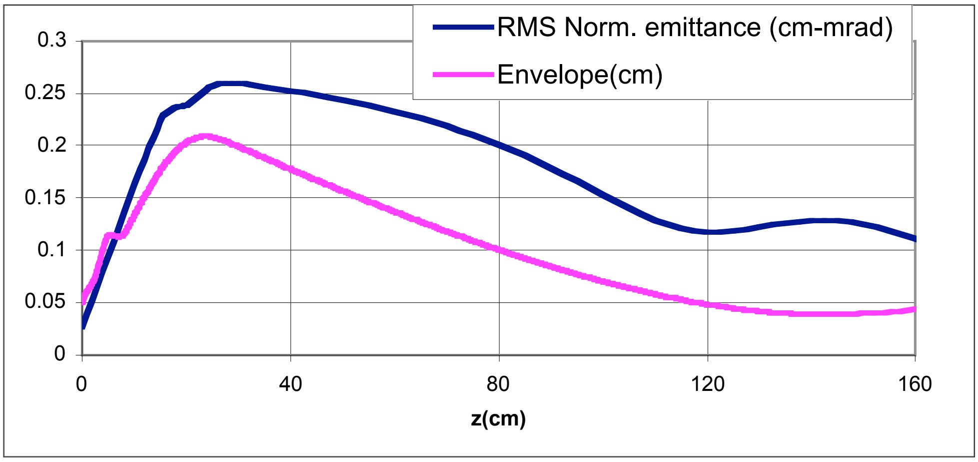

Figure 3.35: *RMS normalized emittance and RMS x-envelope in the gun+drift region computed by PARMELA (N_p=450K).*

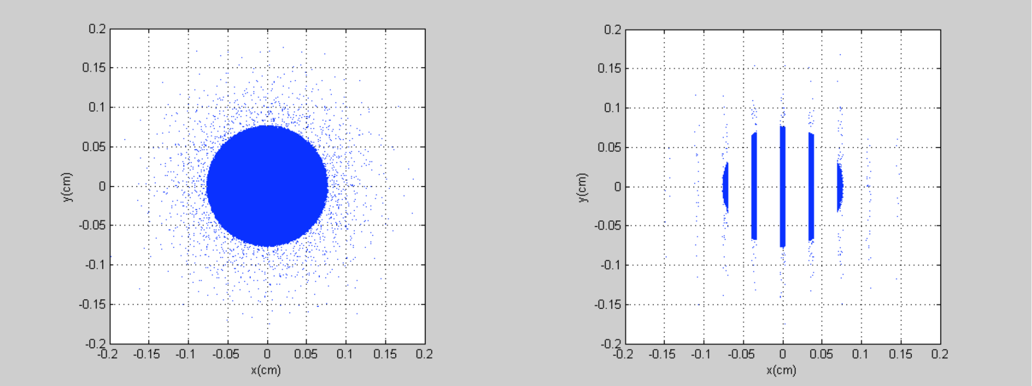

Figure 3.36**:** *Spatial x-y plot of PARMELA distribution at z=150 cm before the slits (Np=450K) and immediately after the zero thickness slit (Np=74671)*

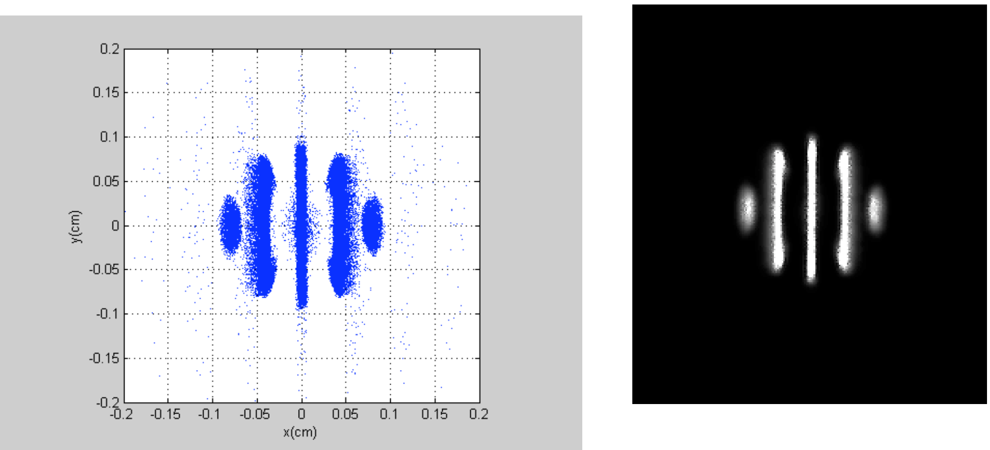

Figure 3.37: *Spatial x-y plot of PARMELA distribution at z=170 cm and the relative image reconstructed on the output screen*

The following parameter set has been used: d = 65 μm, w = 300 μm, L = 20 cm. In the case of a measurement setup with these parameters about 74K particles survived the intercepting slits. These particles are re-input to PARMELA for the tracking to the output screen. Figure 3.36 shows the x-y plot of PARMELA distribution computed before and after the multi-slit mask, while Figure 3.37 shows the x-y plot of PARMELA distribution computed on the output screen and the relative image obtained by an intensity plot recorded in a TIFF format file.

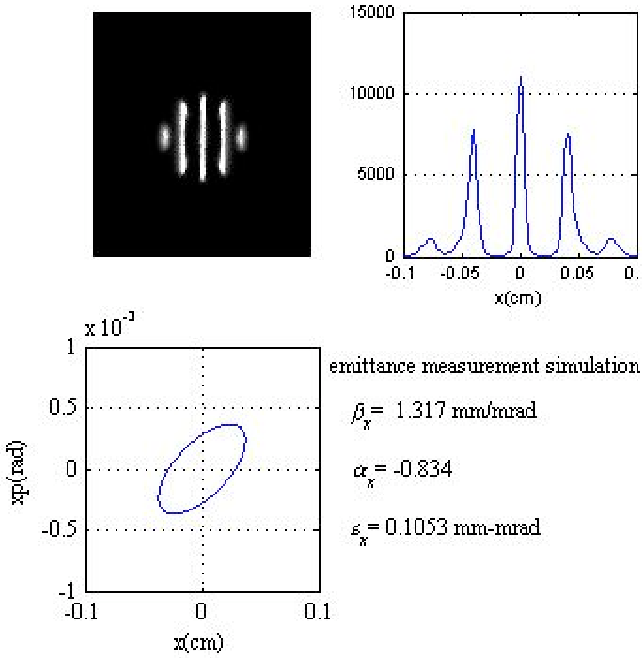

Figure 3.38. *Output of the MATLAB program analysing the PARMELA distribution on the output screen(L=20 cm).*

The image file has been acquired and analyzed by a MATLAB based program that retrieves the intensity distribution of the beamlets and computes the rms emittance (non normalized) and the Twiss parameters. The relative output is presented in figure 3.38

showing the screen image, the reconstructed intensity distribution, the computed beam ellipse and the retrieved phase – space parameters. Using the same approach we span the *z*-region around the beam waist between 120 and 150 cm from the cathode.

In Fig. 3.39 and Table 3.9 the PARMELA values of the rms un-normalized emittance are compared with the values obtained simulating the multi-slit mask using the phase distribution predicted by PARMELA. The calculations were done in all cases switching off the space charge in the region from the mask plane to the output screen. The maximum error in this region is 7%. Only in one point (z=150 cm) we repeated the calculation with the space charge on, in order to estimate the error due to the residual space charge. The increase of the measured emittance is negligible, around 1.4%.

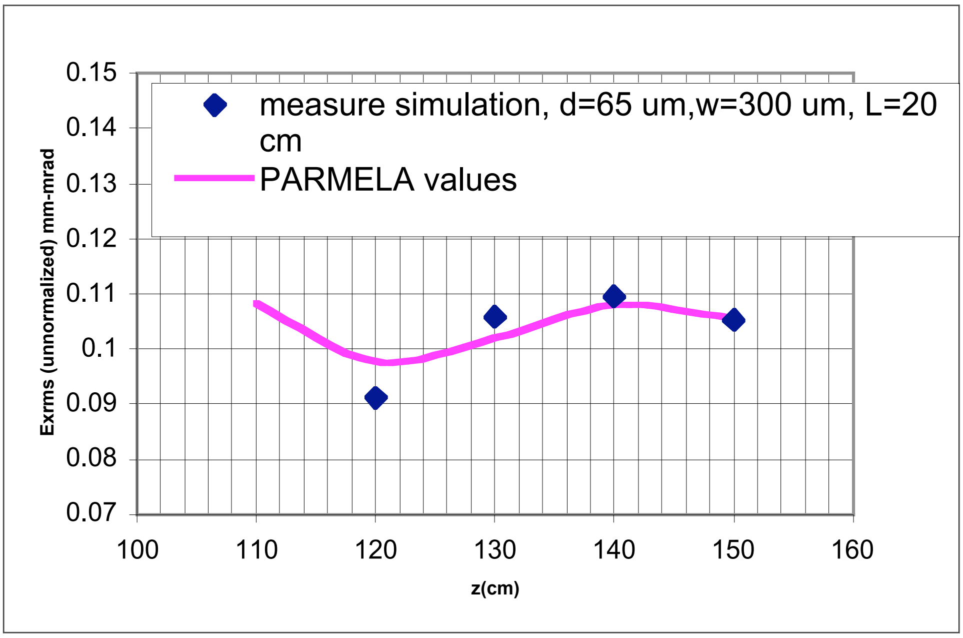

Figure 3.39 *RMS geometrical (un-normalized emittance) vs z.*

TABLE 3.9

z (cm)	ϵ_{rms} (mm mrad) (PARMELA value)	ϵ_{rms} (mm mrad) (retrieved value from virtual measure) *space charge off*	ϵ_{rms} (mm mrad) (retrieved value from virtual measure) *space charge on*
120	0.0977	0.0912	
130	0.102	0.1058	
140	0.108	0.1095	
150	0.1055	0.1053	0.1068

3.7.2 Wake field effects in the bellows

When the emittance measurement slit array is shifted downstream the drift, the beam must propagate inside an increasingly longer bellows assembly. The bellows' convolutions generate wake fields that may affect the measurement results by degrading the beam's emittance and the energy spread [37]. In this section we briefly discuss a study of the wake-fields induced in the bellows. An analytical model [38] due to Bane and Sands is compared with numerical simulations made with the code ABCI, and a preliminary evaluation of the wake-induced effect is presented.

The analytical model (based on pill-box corrugations) for the bellows impedance uses the following geometric notation: *g* is the corrugation length, *a* is the beam pipe radius, *b* is the corrugation depth. The maximum extension of the bellows envisioned in the experiment is 1.5 m with more than N_t~400 corrugations.

For a uniform distribution charge the longitudinal and transverse loss factors per period are:

$$k_{\parallel} = \frac{4}{3\sqrt{2}} \frac{Z_0 c}{\pi^2 a} \sqrt{\frac{g}{l}} \left[\frac{V}{C}\right] \tag{3.7}$$

$$k_{\perp} = \frac{2^{\frac{7}{2}}}{15} \frac{Z_0 c \sqrt{lg}}{\pi^2 a^3} \left[\frac{V}{Cm}\right] \tag{3.8}$$

The formulas showed above were obtained for one convolution. The total bellows wake is not simply the summation of all individual convolution wake; the wakes combine to reduce their individual wake as the beam moves along the bellows as

$$k_N = k \frac{2}{1 + \sqrt{N}}, \tag{3.9}$$

where k_N is the loss factor longitudinal or transverse for one convolution. Equation (3.9) is correct until the bunch reaches the N_{eq} convolutions, where

$$N_{eq} = \frac{a^2}{2g(\pi + \frac{2a}{\sigma})}. \tag{3.10}$$

From this convolution to the end of the bellows, the individual wake remains equal to the N_{eq} wake and the cumulative wake increases linearly with *N,* so the loss factor for all bellows is given by:

$$k_{tot} = \left(\sum_{n=1}^{N_{eq}} \frac{2}{1 + \sqrt{n}} + \frac{2(N_t - N_{eq})}{1 + \sqrt{N_{eq}}} \right) k \tag{3.11}$$

The plots in Fig. 3.40 represent the loss factor for two different longitudinal distributions: a Gaussian bunch and a uniform distribution bunch. It compares the analytical formula of Eq. 3.11 with results obtained with simulations made with the code ABCI for a Gaussian bunch and a squared and triangular shaped bellows. Excellent agreement is obtained between theory and numerical results, especially for the case of a Gaussian bunch.

Note that Eq. 3.11 for a gaussian bunch is quite close to the numerical simulation, while the case of a uniform bunch almost coincides with the asymptotic equation of a gaussian bunch.

These results have been used to examine some different choices of the bellows proposed for the SPARC project. For example, we may take a bellows with the following dimensions: *a*=51.25 mm, *b*=75 mm, *g*=0.90 mm (compressed) - 4.40 mm (extended), corresponding to 340 corrugations. The induced energy spread in case of maximum extension of the bellows in this case is high, around 1.2%.

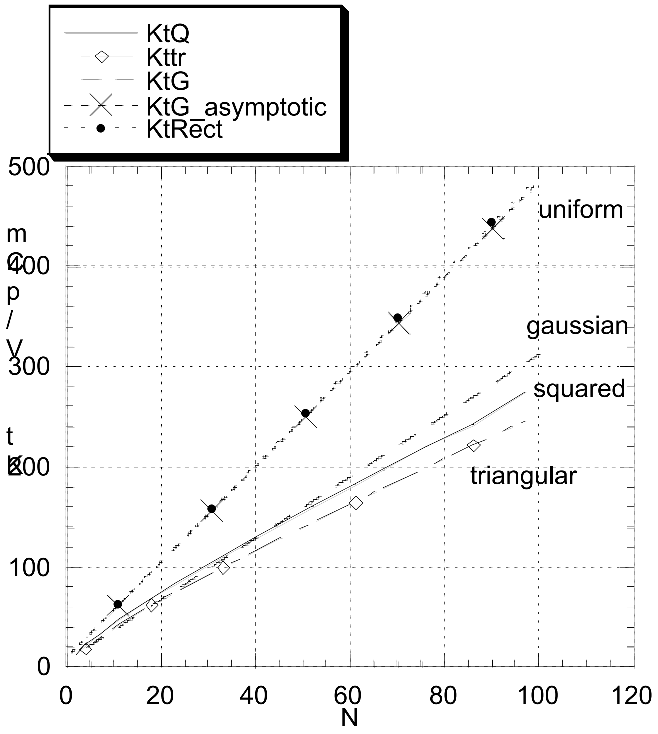

Figure 3.40: *Comparison between the transverse loss factor versus the number of convolutions, obtained with the code ABCI for a triangular and squared bellow and the analytical formulas of a Gaussian bunch. The plot represents also the transverse loss factor of a uniform bunch and a Gaussian bunch using the asymptotic analytical expression. The bellows being used has dimensions: a=1.6cm, b=2.5cm, g=0.5cm (extended). The bunch rms length is σ=1mm.*

The second choice results to be more effective to damp wake-field effects. Notice that the induced energy spread in case of maximum extension of the bellow of case two is of the order of 1.2%, the same order of the space-charge induced energy spread. The emittance degradation corresponding to these effects will be soon evaluated with an improved version of HOMDYN [32]. As to transverse effects, we can make an estimate for the moment by comparing the transverse space charge force with the transverse wake force for experimental conditions. It is found that the transverse wake for any reasonable offset is much smaller than the transverse space charge force at the edge of the beam, indicating that one may expect wake-fields to not interfere strongly with measurement of emittance compensation after the gun in Phase 1a.

3.7.3 High energy slice emittance simulations

The beam will be accelerated up to the final nominal energy 155 MeV by the three traveling wave structure and transported up to the undulator entrance in SPARC Phase 1b. Measurement of slice emittances after final compensation in the linac sections, will be at this stage one of the main experiments to do in view of obtaining the best FEL performances We discuss in this section the slice emittance measurement virtual experiment.

The emittance compensation with a solenoid field relies upon the alignment of the relative phase-space orientation of each temporally slice of the electron bunch. The high brightness beam in the gun occurs when the time sliced-emittance is nearly the same as the cathode thermal emittance and when the slices have nearly the same Twiss parameters. The measurement of the slice emittance is then a powerful tool for verifying and tuning the photoinjector performance.

The slice emittance is the transverse emittance of a short time interval (slice) of the microbunch. It can be measured using an energy-dispersed beam with a linear energy-time correlation or chirp. The chirp is then combined with the quadrupole scan technique to determine the emittance of the slices along the bunch [39,40,41].

In Fig. 3.41 the channel section involved in the measurement is shown: the third linac section is de-phased to produce the desired chirp. After the first triplet, a dipole deflects the beam into the test-line and a screen is placed at the dispersion maximum location. The first two quads after the linac sections are used for the quadrupole scan: the beam is scanned vertically while keeping the horizontal betatron function and thus the horizontal betatron beam size constant. The vertical beam size is measured at the screen vs the doublet strength variation to obtain the emittance of the beam.

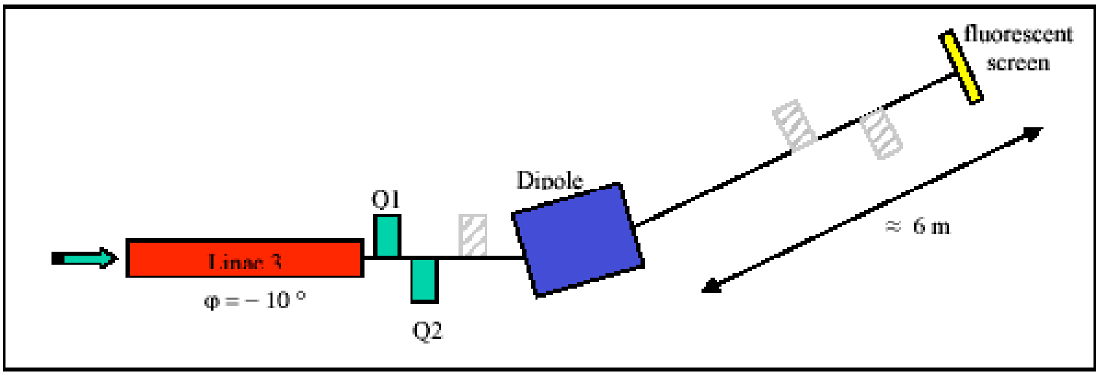

Figure 3.41: *Schematic layout of the slice emittance measurement set-up.*

The beam particles in the two-dimensional phase space are surrounded by the phase ellipse described by:

$$\gamma x^2 + 2\alpha x x' + \beta x'^2 = \varepsilon \tag{3.12}$$

where, α, β, γ are the Twiss parameters and ε is the beam emittance.

The equation of an ellipse can be written in the form:

$$\mathbf{u}^T \sigma^{-1} \mathbf{u} = 1, \tag{3.13}$$

where $\boldsymbol{u}$ and $\boldsymbol{u}^T$ are the coordinate vector and its transpose and σ is a symmetric matrix.

For the ellipse equation in the two dimensional case we obtain:

$$\sigma_{11}x^2 + 2\sigma_{12}xx' + \sigma_{22}x'^2 = 1, \tag{3.14}$$

and comparison with (3.12) defines the beam matrix by

$$\sigma = \begin{pmatrix} \sigma_{11} & \sigma_{12} \\ \sigma_{12} & \sigma_{22} \end{pmatrix} = \varepsilon \begin{pmatrix} \beta & -\alpha \\ -\alpha & \gamma \end{pmatrix} \tag{3.15}$$

from which we have

$$\sigma_{11}\sigma_{22} - \sigma_{12}^2 = \varepsilon^2. \tag{3.16}$$

By measuring the beam size under different focusing conditions, different parts of the ellipse will be probed by the beam size monitor and the beam emittance can be determined through fitting of the data.

In matrix formulation the ellipse parameters transform from a starting point $s = 0$ to any other point $s \neq 0$ by the transformation:

$$\begin{pmatrix} \beta \\ \alpha \\ \gamma \end{pmatrix} = \begin{pmatrix} R_{33}^2 & -2R_{34}R_{33} & R_{34}^2 \\ -R_{33}R_{43} & \left(R_{33}R_{44} - R_{34}R_{34}\right) & -R_{34}R_{44} \\ R_{43}^2 & -2R_{44}R_{34} & R_{44}^2 \end{pmatrix} \begin{pmatrix} \beta_0 \\ \alpha_0 \\ \gamma_0 \end{pmatrix} \tag{3.17}$$

where $\mathbf{R}$ is the transport matrix from 0 to s. If we want to determine the beam matrix at a point P_0, we consider downstream a beam transport line up to a beam size monitor, e.g. a fluorescent screen, and we have for the beam size at the screen location,

$$\sigma_{11} = R_{33}^2 + 2R_{34}R_{33}\sigma_{12} + R_{34}^2\sigma_{22}. \tag{3.18}$$

By varying the focusing of the transport line, we have for each focusing condition and the relative beam size measurement at the screen:

$$\begin{pmatrix} \sigma_{1,11} \\ \sigma_{2,11} \\ \vdots \\ \sigma_{n,11} \end{pmatrix} = \begin{pmatrix} R_{1,33}^2 & 2R_{1,33}R_{1,34} & R_{1,44}^2 \\ R_{2,33}^2 & 2R_{2,33}R_{2,34} & R_{2,44}^2 \\ \vdots & \vdots & \vdots \\ R_{n,33}^2 & 2R_{n,33}R_{n,34} & R_{n,44}^2 \end{pmatrix} \begin{pmatrix} \sigma_{11} \\ \sigma_{12} \\ \sigma_{22} \end{pmatrix} \tag{3.19}$$

Fitting of the parameters σ_{11}, σ_{12} and σ_{22} to match the measured curve, the beam emittance can be determined from (3.16). To measure the slice emittance each beam picture collected at the screen is “sliced” along the horizontal axis, and for each slice the beam size is determined for each different focusing condition of the line. The emittance of each slice is then obtained fitting the beam matrix parameters for each measured curve.

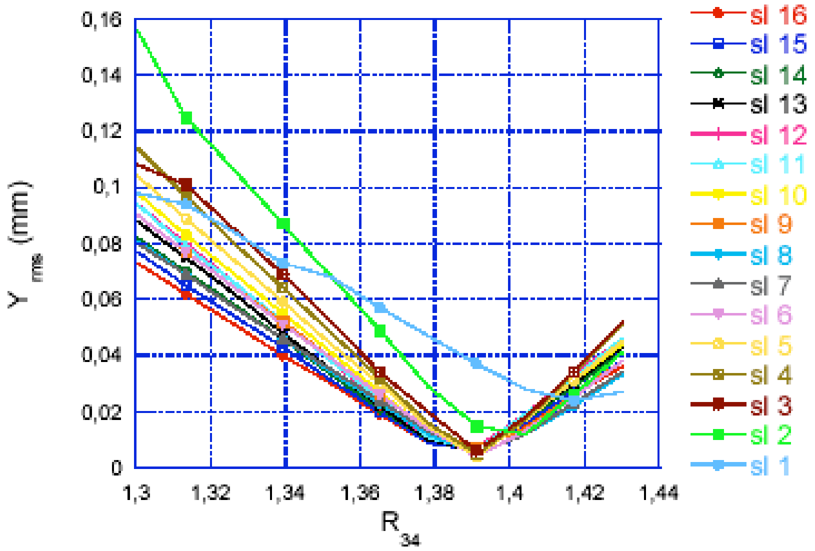

Figure 3.42. *Quadrupole scan results: the vertical beam size is reported vs. the transport matrix element R_{34}*

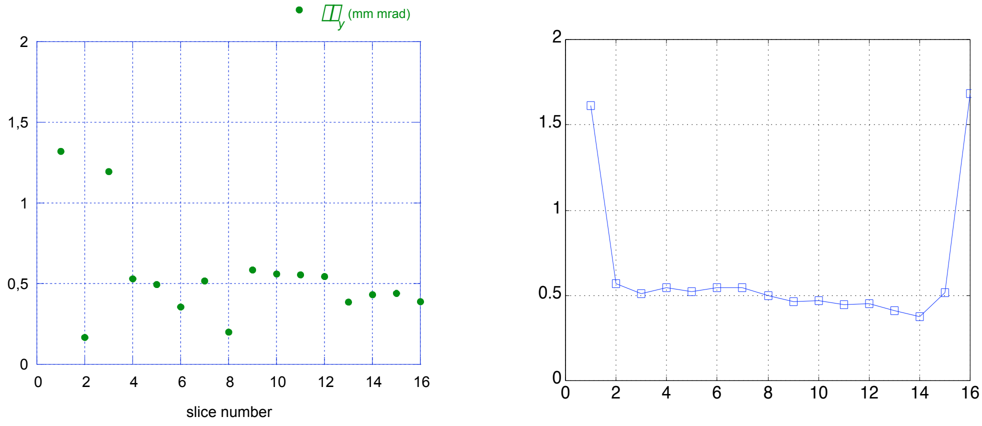

a) **b)**

Figure 3.43 - *The results of the quadrupole scan simulation are reported in figure a). The time analysis of the unperturbed beam is shown in fig b).*

The slice emittance measurement has been simulated with the ELEGANT code; the first results are reported. The 150k particle beam obtained with PARMELA, at the end of the second linac section, is tracked into the third one with a phase delay of 10 deg and a reduction of energy less than 1 MeV. For each set of the doublet upstream the deflecting dipole, the final distribution of the beam, as collected on the screen, is analyzed. With the help of a Matlab code the *x*-*y* distribution is divided into 16 slices equally spaced along the horizontal axis; for each slice the vertical rms size is determined. In Fig. 3.42 the results of the quadrupole scan is reported for each slice.

The three parameters σ_{11}, σ_{12} and σ_{22} are obtained by fitting the curve; the emittance is obtained with Eq. 3.16, the results obtained for each slice are reported in Fig. 3.43(a). In Fig. 3.43(b) the time analysis of the unperturbed beam is reported for comparison. Further simulation work is in progress for the measurement setup tuning, in order to achieve the best conditions for the resolution and precision of the results. It is notable that the simulated virtual measurement does not automatically produce accurate results (*e.g.* when the beam envelopes of all of the slices are not measured about both sides of the minimum in the variable parameter), and in doing so gives us insight into how to avoid errors in the actual measurement.

3.7.4 Simulations of RF deflector-based longitudinal and transverse diagnostics

While the “time-dependent” measurement of slice emittance outlined in the previous section seems to be a powerful tool for use at SPARC, it suffers from reliance on knowledge of the relationship between the beam’s slice energy and its longitudinal position. In practice, since one does not know in detail the effects of longitudinal space-charge and wakefields, which can significantly change the slice energy, this method has some inherent uncertainty in practice.

The difficulty attached to purely dispersive time-slice measurements can be circumvented with the use of an RF deflector. This is in fact a very versatile device, as allows measurement the bunch length, and also, if one uses the orthogonal (non-deflection) direction, one may perform a wide variety of time-slice measurents. In direct opposition to the limitations of the purely dispersive systems, by adding a dispersive system after the deflector, longitudinal beam phase space can be completely reconstructed. The longitudinal beam distribution can be projected along a given transverse coordinate at a detector flag, and using the orthogonal transverse coordinate distribution, both the horizontal and vertical beam emittances can be measured with the quadrupole scan technique. Note that in combination with the dispersive method, one may simultaneously measure the emittances in both transverse planes. Finally, one may use a narrow collimator in the deflection plane to create an ultra-short, low charge (but high current) beam. A schematic layout of the measurement is reported in Fig. 3.44.

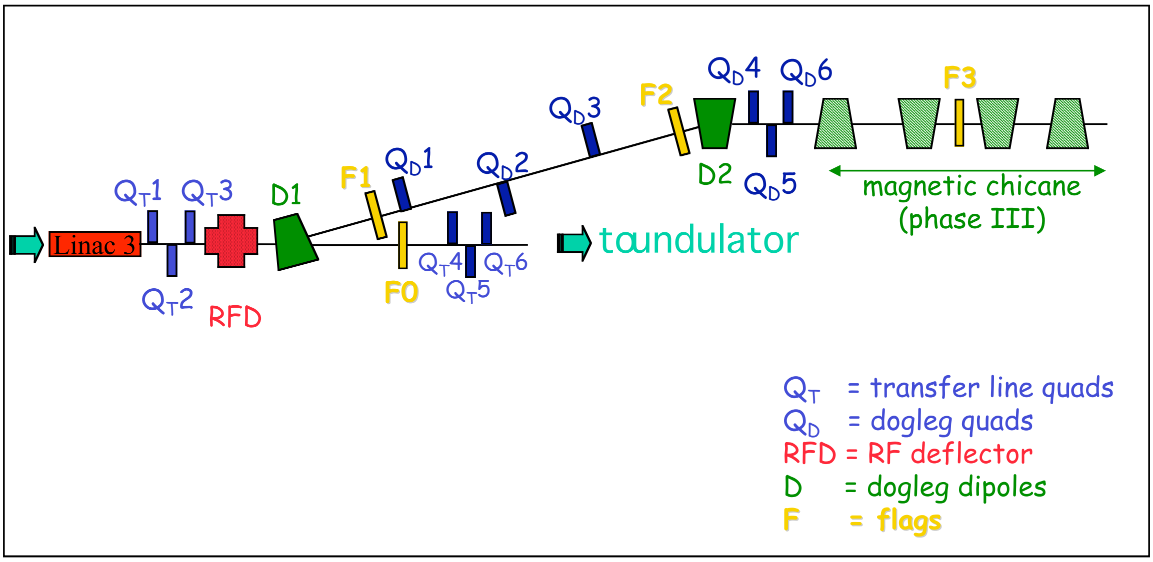

Figure 3.44*: SPARC measurement layout for high energy beam characterization.*

In Fig. 3.45 the effect of the RF deflector is illustrated; the RF deflector voltage (the integrated transverse kick) is null in the longitudinal center of the bunch and gives a linear transverse deflection to the bunch itself. If we consider, the beam distribution a drift space of length L after the deflector, the transverse kick results in a transverse displacement of the centroid of the bunch slice. This displacement proportional to the slice longitudinal offset L_B, and RF voltage according to the expression

$$x_B = \frac{\pi f_{RF} L L_B V_\perp}{cE/e} \qquad (3.20)$$

where f_{RF} is the frequency of the deflecting voltage, $V_\perp$ is the peak transverse voltage, and E/e is the beam energy in eV units. More complicated expressions result when one considers magnetic components instead of a simple drift space between the deflector and detector. Equation 3.20 shows that the transverse bunch distribution can be obtained by measuring the transverse bunch distribution at the position z_s.

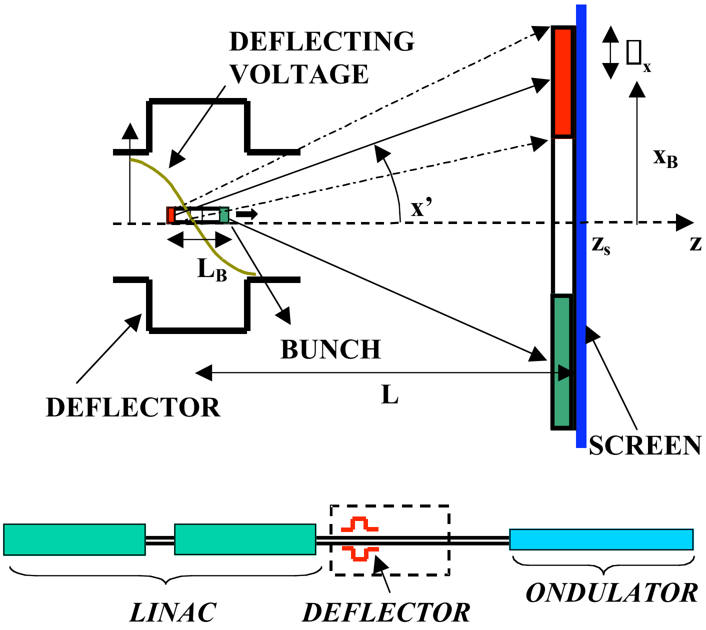

Figure 3.45: *Bunch length measurement schematic setup using an RF deflector.*

As illustrated in Fig. 3.45, the transverse distribution of the bunch at the position z_s is the convolution between the displaced slices and the proper transverse slice sizes at the position z_s. In order to measure the bunch length with the proper accuracy, the displaced position x_B has to be bigger than σ_x. The resolution length (L_{res}) can be defined, therefore, as the relative slice longitudinal position that gives, on the screen, an x_B equal to σ_x. By use of Eq. 3.20 we can calculate the transverse voltage $V_\perp$ necessary to achieve a certain resolution:

$$V_\perp = \frac{\sigma_x cE/e}{\pi f_{RF} L L_{res}}. \qquad (3.21)$$

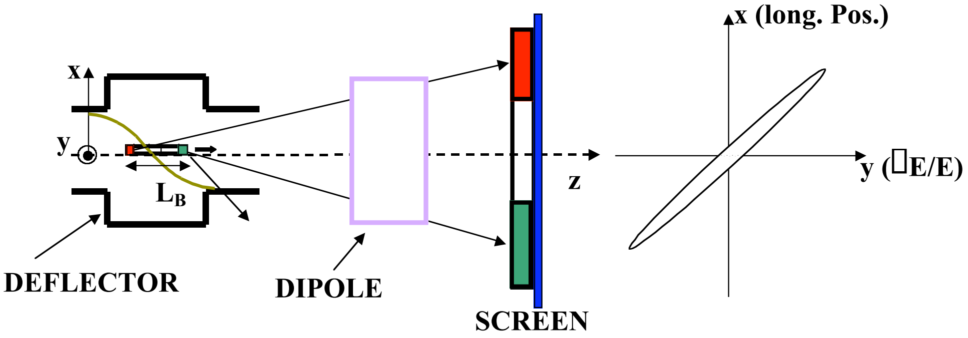

Figure 3.46: *Longitudinal phase space measurement setup using an RF deflector and a dipole magnet.*

A sketch of the complete longitudinal phase space measurement setup is shown in Fig. 3.46. In this scenario, the bunch is vertically deflected by the RF deflector and horizontally by a magnetic dipole. The dispersion properties of the dipole allow to completely characterize the energy distribution of the slices and the total longitudinal phase space can be displayed on the screen.

A full transverse phase space characterization is obtained measuring the beam slice emittance in both the transverse planes. The slice emittance can be measured as discussed above, using a beam with known approximately linear energy-time (dispersive method), or as we discuss below, transverse position-time (RF deflector) correlations. Using the RF deflector the horizontal slice emittance $\Box_x$ can be measured either on the transfer lines or on the dogleg, at the flags F0 and F3, respectively.

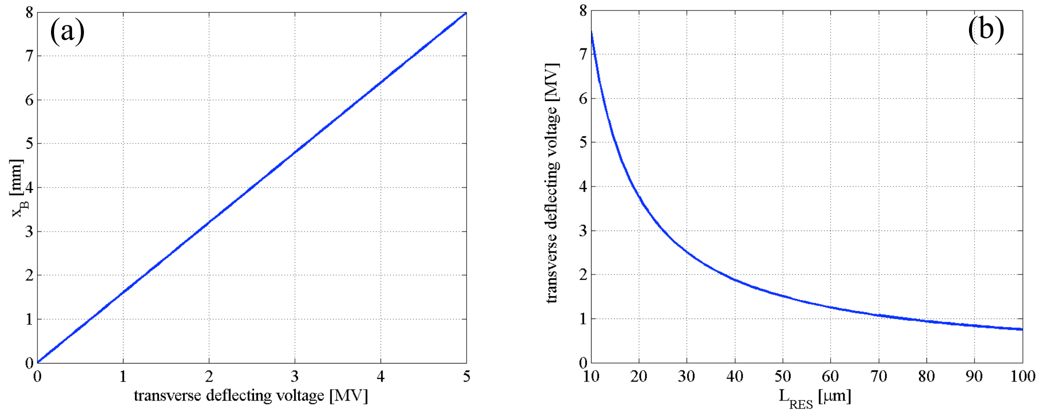

Figure 3.47: *(a) total transverse dimensions of the bunch as a function of the deflecting voltage* $V_{\Box}$*; (b) deflecting voltage* $V_{\Box}$ *as a function of* L_{res}*.*

The first two quads after the linac sections, Q_{T1} and Q_{T2} , are used in this case for the quadrupole scan: the beam horizontal size at the the screen (F0,F3) is varied while keeping the vertical size constant. The measurement results are again fit following the prescription of Eqs. 3.18 and 3.19.

With the dispersive system the same two quads are used to vary the vertical beam size at the location of the flag F2 with an opportune value of the horizontal dispersion. The third linac section is dephased to about 30∞ off crest to produce the desired energy chirp. The measured values of the rms vertical beam size are fit to obtain the vertical beam slice emittance.

Using Eqs. 3.20 and 3.21 it is possible to calculate the total transverse dimensions of the bunch as a function of the deflecting voltage $V_{\Box}$ and needed deflecting voltage $V_{\Box}$ as a function of L_{res}. The results are plotted in Figs. 3.47(a) and 3.47(b), assuming L_B=4 mm, E/e=150 MV, L=2 m and $\Box_x$ =30 □m.

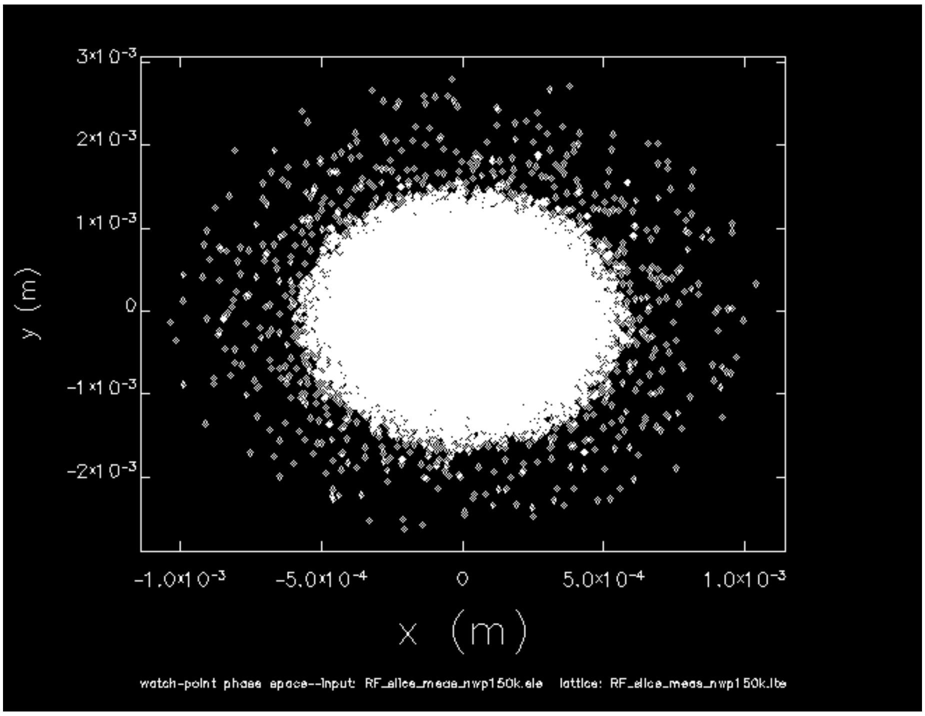

Figure 3.48: *Bunch transverse distribution at the RF deflector location.*

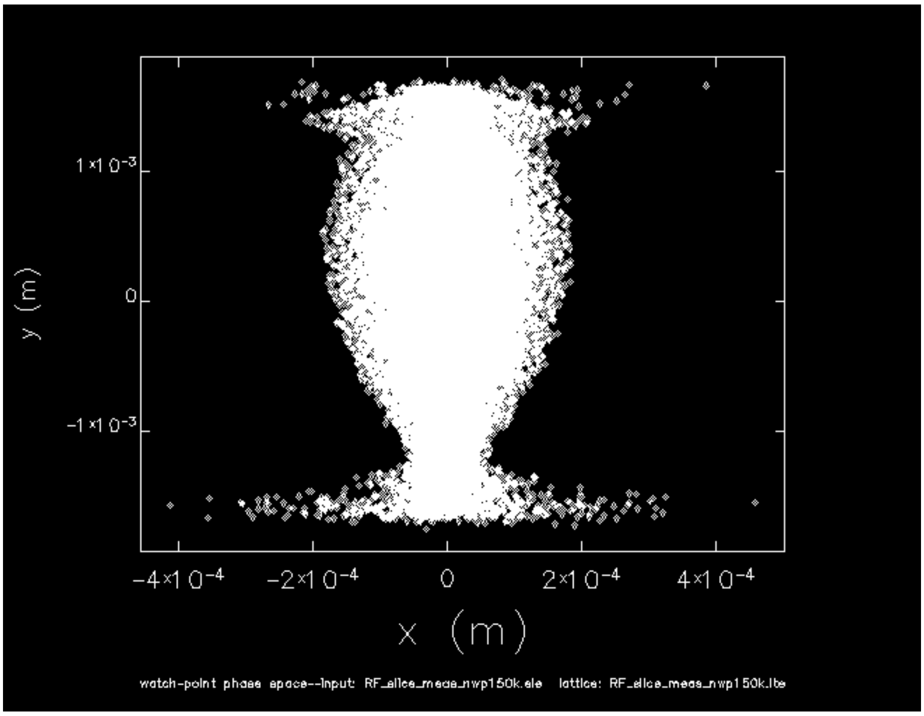

Figure 3.49: *Bunch transverse distribution at F0.*

From these considerations, as well as a desire to mitigate the total power needed, a voltage $V_{\square}$= 1.0 MV (see Section 4.6.3 for details of the electromagnetic characteristics of the deflector) has been chosen for the RF deflector. A 150k particle beam obtained from PARMELA simulation at the end of the linac section has been tracked with the ELEGANT code along the SPARC transfer lines. The images of the beam obtained at the RF deflector location and at the screen location, F0, are shown in Figs. 3.48 and 3.49.

The results of the data analysis are shown in Fig. 3.50 where the vertically projected and the longitudinal distributions of the bunch are displayed. The value of σ_z as obtained by applying Eq. 3.20 and by the longitudinal analysis of the raw data obtained from ELEGANT tracking agree with an error less than 1%.

The images collected on the dogleg at the screen located in F1 show the complete reconstruction of the longitudinal phase space as shown in Fig. 3.51 - 3.52 where the time-energy (*t,p*) distribution is replicated to a fairly good approximation in the transverse plane (*y,x*). It is apparent from the reconstruction that it is difficult to reproduce the nearly filamentary distribution in phase space; some blooming of the narrow "line" in phase space shown in Fig. 3.51 is to be expected.

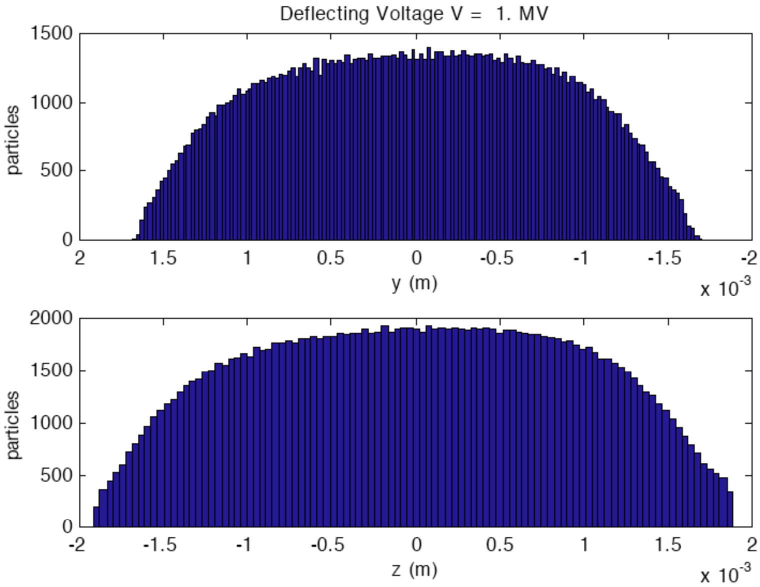

Figure 3.50: *Above: the longitudinal bunch distribution as projected by the RF deflector on the vertical coordinate of the screen F0; below: the same bunch longitudinal distribution vs. time.*

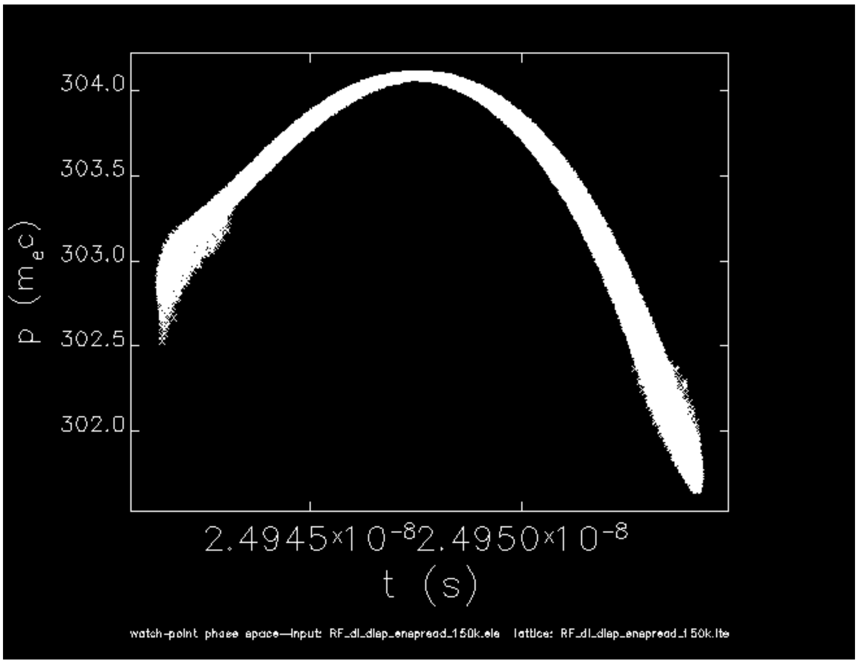

Figure 3.51*: Bunch longitudinal distribution vs time at F1.*

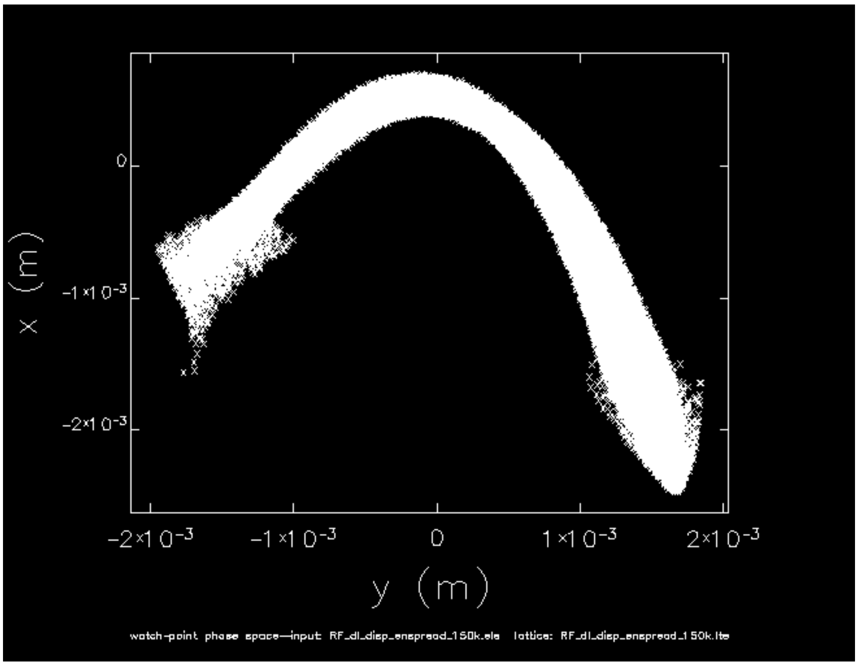

***Figure 3.52**: Bunch transverse distribution at F1.*

To measure the beam slice emittance in the horizontal plane the RF deflector can be used scanning the beam rms size at the screen locations F0 and F3, where two different values of image resolution can be achieved for the minimum horizontal rms size reconstruction. For the vertical emittance the dispersive system can be used with the beam image being examined at the screen location F2.

In Figs. 3.53 and 3.54 the optic functions of the SPARC transfer lines and dogleg are reported for the measurement setup of the horizontal emittance.

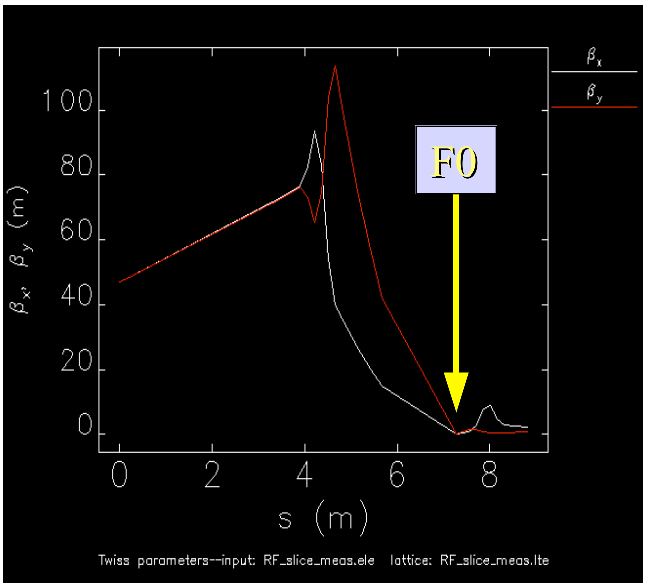

***Figure 3.53:** SPARC transfer lines optic functions for the horizontal quad scan at F0. The origin of the longitudinal coordinate corresponds to the exit of the second linac section.*

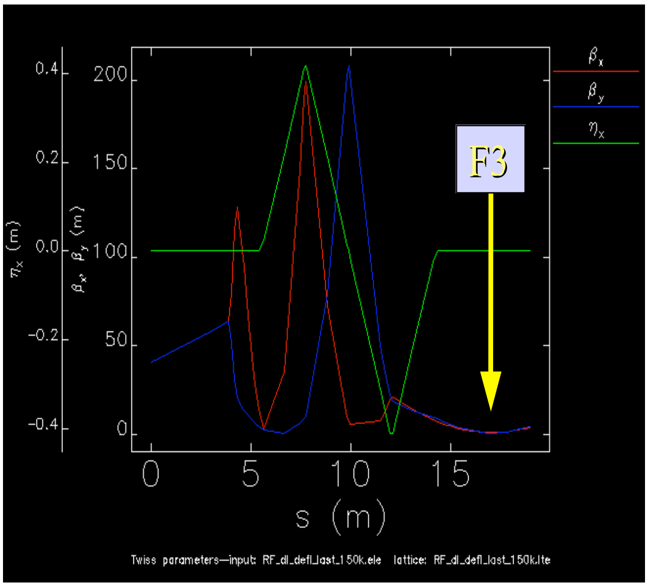

Figure 3.54: *SPARC dogleg optic functions for the horizontal quad scan at F3. The origin of the longitudinal coordinate corresponds to the exit of the second linac section.*

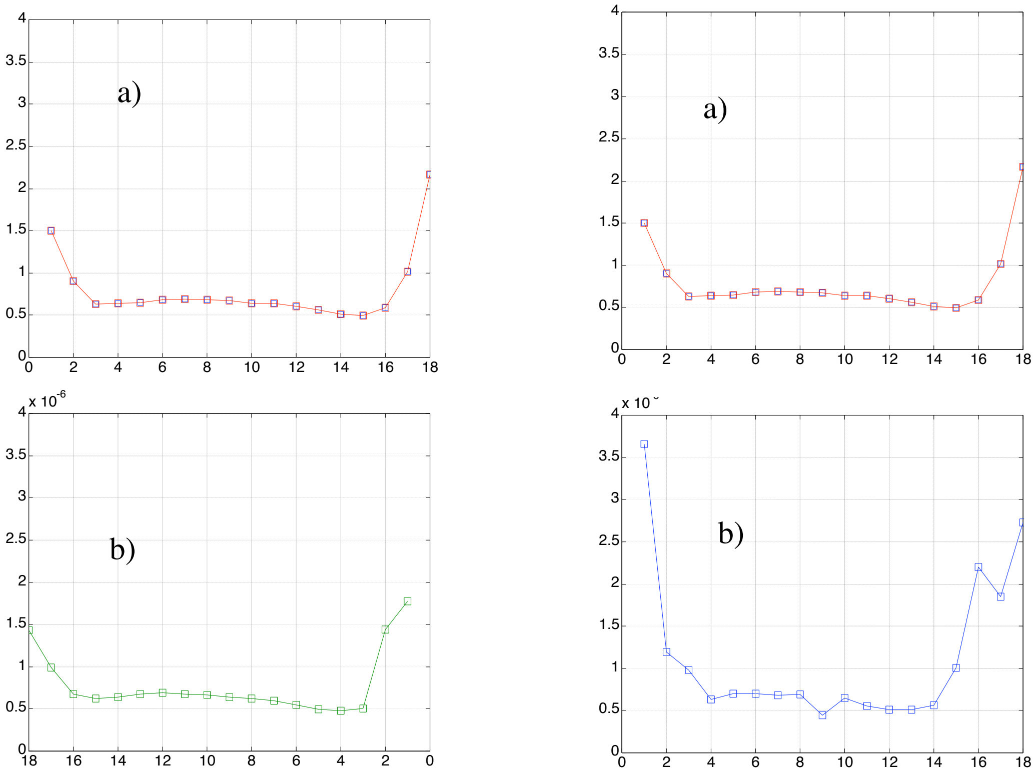

***Figure 3.55**. Reconstructed horizontal beam slice emittance (in mm-mrad) as a function of slice number with the beam size scanning at F0 (left), and at F3 (right). The a) curves (above) is the horizontal emittance as calculated by slicing the beam along the temporal coordinate, the b) curves (below) are the result of the two quadrupole scan at the two screen locations.*

In Fig. 3.55 the beam horizontal slice emittance is given for the two simulated measurements at F0 (left) and F3 (right), respectively. For the top figures, the result of the temporal analysis of the raw data is reported for the two cases; those below show the reconstructed horizontal slice emittance. The main difference between the results obtained scanning at F0 or F3 is the minum value of the rms beam size as can be seen in Fig. 3.56, where the curves refer to the new SPARC working point. This aspect provides a tool to investigate a wide range of beam emittance values without loosing the measurement accuracy.

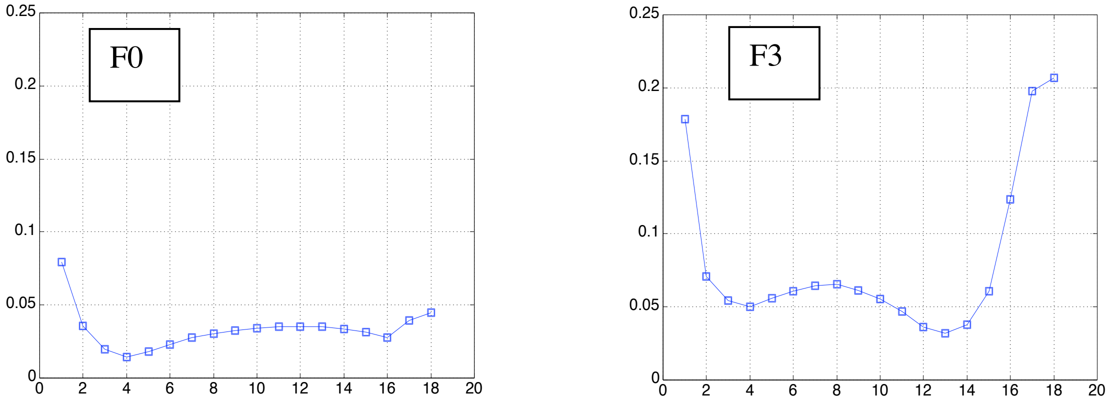

Figure 3.56. *Minimum horizontal rms beam size (cm) at the two screen locations: F0 (left), and F3 (right) during the quadrupole scan.*

3.8 HIGH PEAK CURRENT EMITTANCE COMPENSATION (PHASE 2)

SPARC Phase 2 will be mainly devoted to beam dynamics studies related to bunch compression systems. Two possible schemes will be compared, as shown in Figure 3.57. A standard magnetic chicane will be installed in a parallel beam line, while a new technique based on the so-called velocity bunching (VB) scheme will make use of the first linac sections to provide longitudinal focusing [42]. We discuss in this section the design principles and the layout for both options.

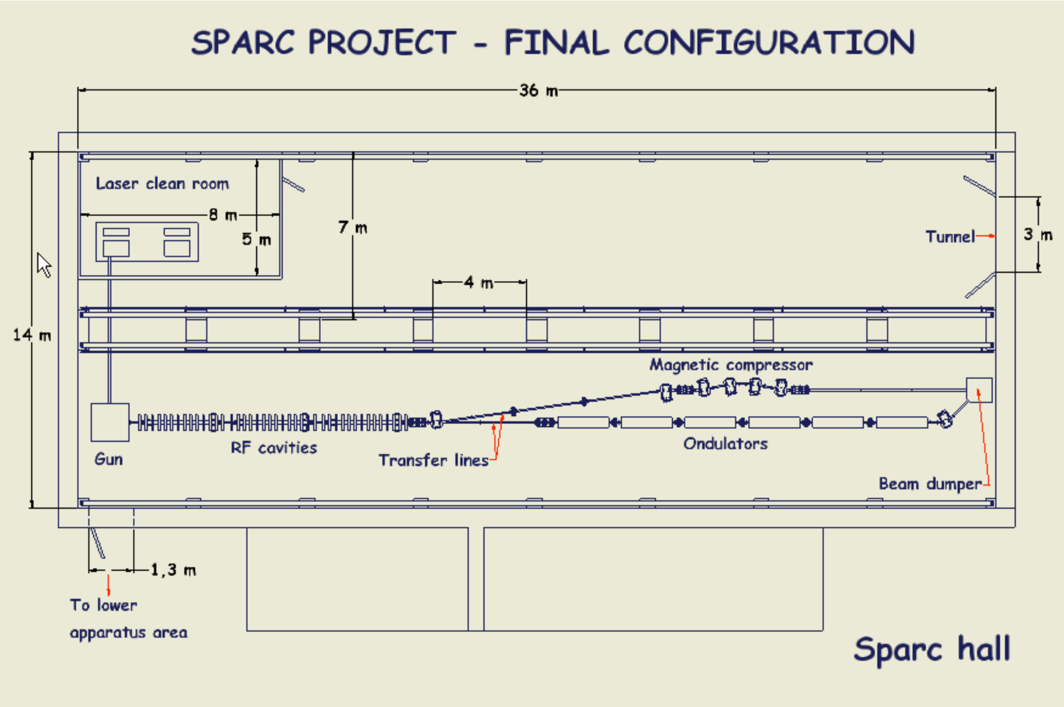

Figure 3.57: *Schematic of SPARC – Phase 2*

3.8.1 Dog leg and bunch compressor line

The main transfer line connects the linac to the undulator on a straight line; a bending magnet after the first triplet deviates the beam into a line used for diagnostics, in particular for energy spread and slice emittance measurements. In Phase 2 it is foreseen to expand this section in order to have a parallel line for beam studies and a magnetic chicane for bunch compression experiments.

The first part of the line is a dogleg made of two bends and three quadrupoles which are used to cancel the dispersion function. A small bending angle (11°) has been chosen to minimize the perturbation on the beam; the distance between the parallel line and the main line is 1.67m, which allows access between the two lines. The distance between the first dogleg quadrupole and the main line is only 0.41 m; a layout drawing is needed to check for space availability.

A matching triplet is inserted between the dogleg and the magnetic compressor to adjust the minimum of the beta functions inside the compressor. The bunch compressor has a value of R_{56} = .141 m and of T_{566} = -.218 m. The dogleg contribution to R_{56} is negligible, R_{56} = -.003, but the contribution to T_{566} is large, T_{566} = -*.48*. The effects of second order terms on the bunch compression have been studied by simulations, and found to be insiginificant.

From PARMELA simulations the expected rms bunch length and relative energy spread are: σ_l = 1 mm and σ_δ = 0.2%. The chosen value of R_{56} produces full compression of the bunch for a correlated relative energy deviation δ lower than 1%. The displacement of the beam in the chicane is 0.30 m. In order to use the compressor between zero and the maximum, the design of a chamber with bellows and movable dipoles has to be studied.

The magnetic elements after the first dipole are described in Table 3.10, the first triplet is part of the main line. The beta and dispersion functions along the line are shown in Figs. 3.58 and 3.59. The horizontal and vertical rms beam sizes are shown in Fig. 3.60 together with the beam envelope for an energy deviation δ = 1%. The initial conditions for the plots are: energy 150 MeV, rms normalized emittance 0.5 μm, $\beta_{x,y}$ 71 m and α_{xy} –4.

Table 3.10 *- Magnetic elements after the first dipole*

	Number	Length (m)	Angle	B (T) @150 MeV	G_{max} (T/m) @150 MeV
Dog leg dipoles	2	.26	11°	.37	
Compr. Dipoles	4	.26	14°	.47	
Quadrupoles	9	.15			3.2

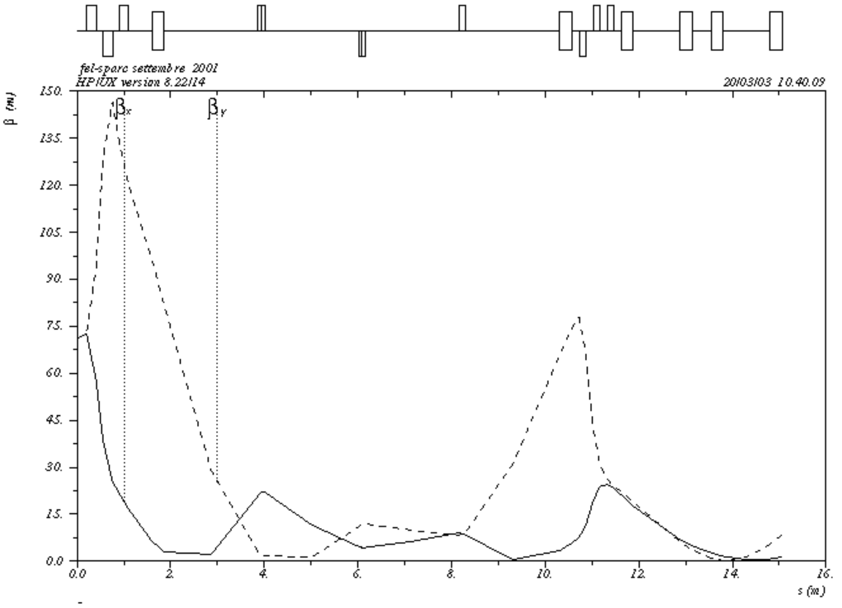

Figure 3.58*: Beta functions along the injector beamline.*

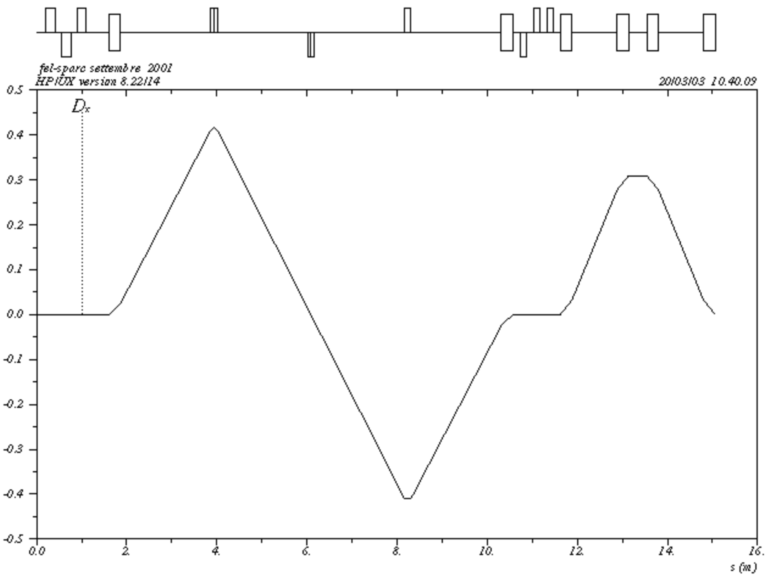

Figure 3.59: *Dispersion function along the dogleg line.*

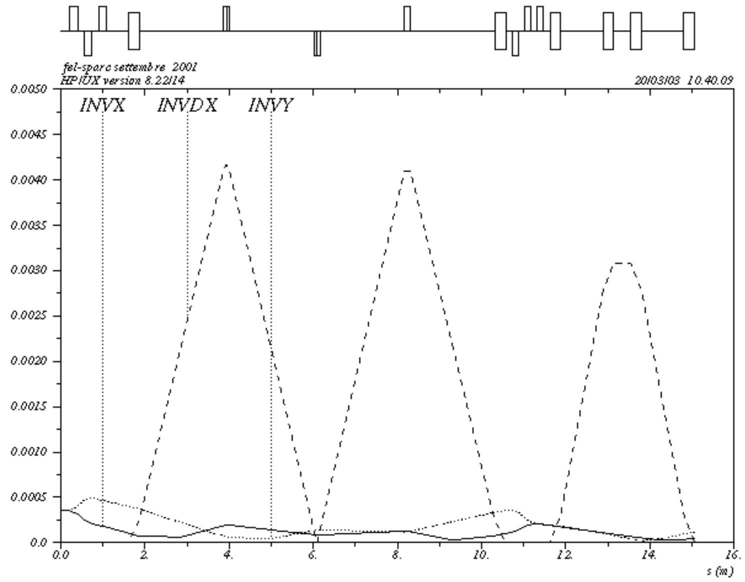

Figure 3.60: *Beam envelope along the line: $\square_x$ (solid), $\square_y$ (dotted), $D_x\square$for $\square$= .01 (dashed).*

3.8.2 Velocity bunching design principles

The impact of magnetic compressors on the beam quality is quite relevant, with tendency to cause a serious emittance growth due to coherent synchrotron radiation [43] effects in their bends. The VB method, able to compress the bunch at moderate energies (tens of MeV) on rectilinear trajectories and integrated in the emittance compensation process, is in principle free from this source of emittance degradation. The theoretical model explaining velocity bunching is based on a Hamiltonian treatment as follows.

The interaction of a beam with a RF wave given by $E_z = -E_0 sin(\omega t - kz + \psi_0)$ is described by a Hamiltonian:

$$H = \gamma - \beta_r \sqrt{\gamma^2 - 1} - \alpha cos\xi \tag{3.22}$$

where γ is the normalized electron energy, $\xi = kz - \omega t - \psi_0$ is its phase with respect to the wave, while $\alpha \equiv eE_0/mc^2k$ is the dimensionless vector potential amplitude and $\gamma_r = 1/\sqrt{1-\beta_r^2}$ is the resonant gamma of the wave (conventional traveling wave structures operate at $\beta_r = 1$, $k = \omega/\beta_r c$).

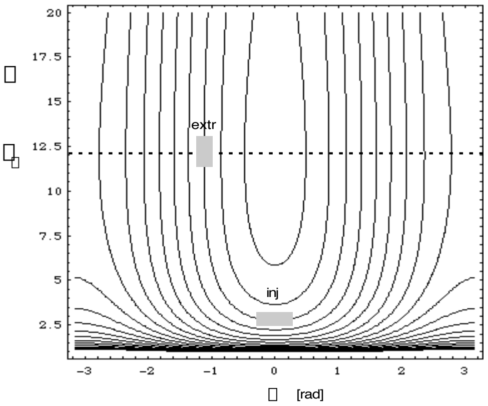

***Figure 3.61** –Phase space plots of a slow RF wave (γ_r finite) showing the basics of phase compression in a linac.*

A wave whose phase velocity is slightly smaller than *c*, so that $k = \omega/c + \Delta k$, is characterized by $\beta_r = 1 - c\Delta k/\omega$, $\gamma_r = \sqrt{\omega/2c\Delta k}$ (assuming $c\Delta k/\omega << 1$).

The basic mechanism underlying the rectilinear compression effect is illustrated in Fig. 3.61, where the contour lines of the Hamiltonian associated to a slow RF wave having γ_r= 12 (*i.e.* β_r = 0.9965 and Δ_k = 0.0035 ω/c) and α = 0.2 are plotted. If the bunch is injected into the wave at zero phase (*i.e.* when the field of the wave is not accelerating) at an energy lower than the synchronous one (which corresponds to γ_r), it will slips back in phase and go up in energy (being accelerated by the wave). By extracting the beam from the wave at the time it reaches the resonant γ_r, *i.e.* when it becomes synchronous with the wave, we make the bunch undergo one quarter of synchrotron oscillation. In doing that the beam is compressed in phase as depicted in the figure.

In order to preserve the beam transverse emittance we have to integrate the longitudinal dynamics of the RF compressor with the process of emittance compensation, which is achieved for a beam at constant current by matching it on the invariant envelope, as discussed in Section 3.3. The analytical model is basically an extension of the invariant envelope theory [14], to the case of currents growing together with energy along the RF compressor [44]. The analysis reported in Section 3.3 is valid only for beams carrying constant peak current *I* , as usual in photoinjectors when no compression mechanism is. In order to extend the model to the case of RF compression, where *I* grows by large factors, we have assumed that the current grows in the compressor at the same rate as the energy, *i.e.* $I = I_0\gamma/\gamma_0$, where I_0 and γ_0 are the initial values for the current and the energy, respectively, at injection into the compressor. This assumption is derived by observations performed in several simulations of the RF compressor, indicating that best results in terms of final beam brightness are achieved under this condition of adiabaticity, which indeed gives rise to a new beam equilibrium.

The new exact analytical solution of the rms envelope equation becomes:

$$\square_{RFC} = \frac{1}{\square\square\square}\sqrt{\frac{I_0}{2I_A\square_0}} \qquad (3.23)$$

i.e. a beam flow at constant envelope (instead of $1/\sqrt{\square}$ as for the invariant envelope). This is dictated by a new equilibrium between the space charge defocusing term (decreasing now as $1/\square^2$) and the focusing and acceleration terms (imparting restoring forces to the beam): while for the invariant envelope equilibrium is achieved even in absence of external focusing , i.e. at $\square = 0$, in this case we need to provide external focusing. A possible VB scheme is discussed in the next section.

3.8.3 Velocity bunching optimization for SPARC Test

The main purpose of the VB experiment at SPARC is to demonstrate the capability to increase the bunch peak current without degrading the emittance. As discussed in section 3 the emittance compensation process has to be tuned until the bunch goes from the laminar regime to the emittance dominated regime. SPARC phase 1 was in fact optimised for a 90 A beam up to 150 MeV. Operating the first TW structure in the VB mode and the other two TW structures in acceleration mode (on crest at maximum gradient 25+15 MV/m) will result anyway in a lower energy gain, about 120 MeV, still below the transition energy. For this reason we decided not to push the VB performance to its ultimate possibility (~ kA) [45] but to get experience of the emittance compensation process during bunching with a low compression ratio: 200 A at 120 MeV. Higher compression ratio will be also tested, even if the emittance compensation process won't be totally accomplished. In Figure 3.62 are shown the possible VB working points versus the injection phase in the first TW structure.

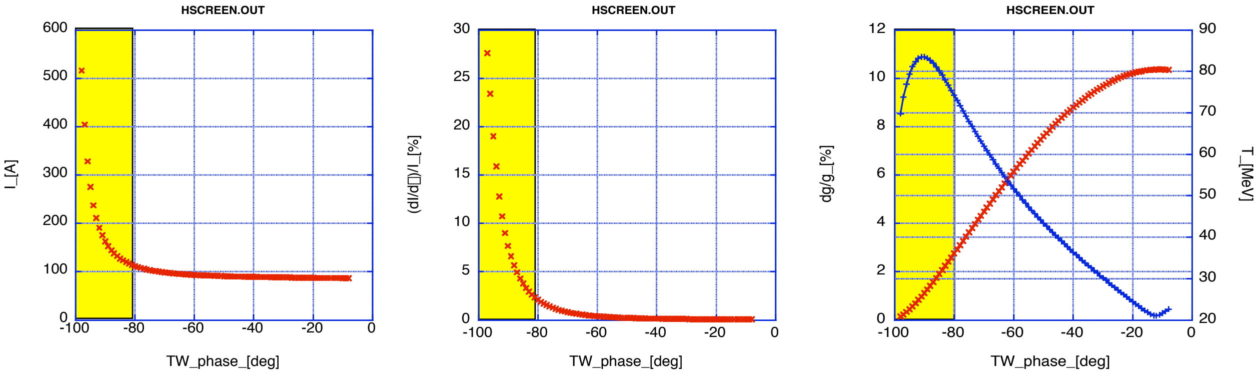

Figure 3.62: *Peak current (left plot), sensitivity to ± 0.5 deg phase jitter (central plot), rms energy spread (blue line, left plot) and energy gain (red line, left plot) versus injection phase in the first TW structure working at 25 MV/m accelerating field.*

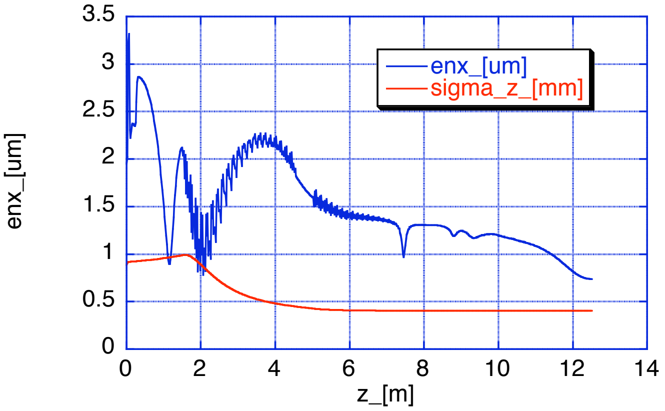

Figure 3.63: *The rms normalised emittance and rms bunch length evolution along the beam line, injection phase at around –92 deg.*

Figure 3.63 shows the rms normalized emittance and rms bunch length evolution along the beam line for the –92 deg injection phase option. The bunching effect (a factor 2 as measured by the rms value) of the first TW section, working at 25 MV/m, is clearly visible. The emittance compensation process requires now a more careful optimisation: during this experiment the three TW sections will be all embedded in solenoid fields (600-700 Gauss) to properly tune the beam plasma frequency as predicted by theory. At the exit of the third TW structure the emittance has reached a significantly lower value of 0.8 μm. The slice analysis shown in Fig. 3.64 shows that the slices carryng the higher peak current have also the best emittance. The rms energy spread results to be 1.8 % without any optimization.

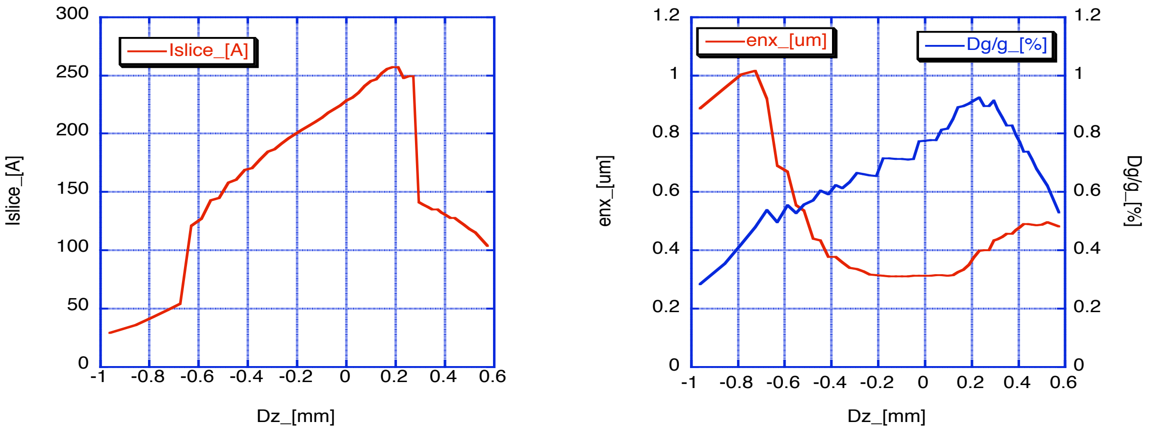

Figure 3.64: *Peak current (left plot), rms norm. emittance and rms energy spread (left plot) along the bunch at the exit of the linac, computed within 300 μm long slices.*

Sensitivity to phase jitter is one of the main areas of investigation one must address in order to integrate the VB technique in a larger scale FEL experiment, like the SPARX proposal. In the previous case simulations show that a phase jitter of ± 0.5

deg in the gun, would result in 10% fluctuation in the peak current at the exit of the linac. It has been shown that extending the bunching process over more than one TW structure working at a lower gradient is much better in terms of phase sensitivity [45]. In the next section a reduced gradient VB design is presented together with its possible integration in the SPARX design.

3.8.4 Integration of velocity bunching in SPARX: □-jitters effects

An injector design based on VB may be more suitable to drive a larger scale FEL experiment, and its integration in a 2 GeV linac [46], is discussed in this section. Higher brightness is achieved by increasing the compression ratio and with a more gentle emittance compensation by means of lower gradient TW structures embedded in stronger solenoid fields. In order to obtain slow bunching of the beam and to increase the focusing magnetic field with the current during the compression process as prescribed by theory, we used the first two sections as compressor stages. The RF compressor parameters set is shown in Table 3.11. PARMELA calculations, done for a 1 nC 10 psec long (FWHM) bunch with a rise time of 1 psec, and 1 mm radius, show that with a proper setting of accelerating sections phase and solenoids strength it is possible to increase the peak current up to 300 A while preserving the beam transverse emittance (Fig. 3.65).

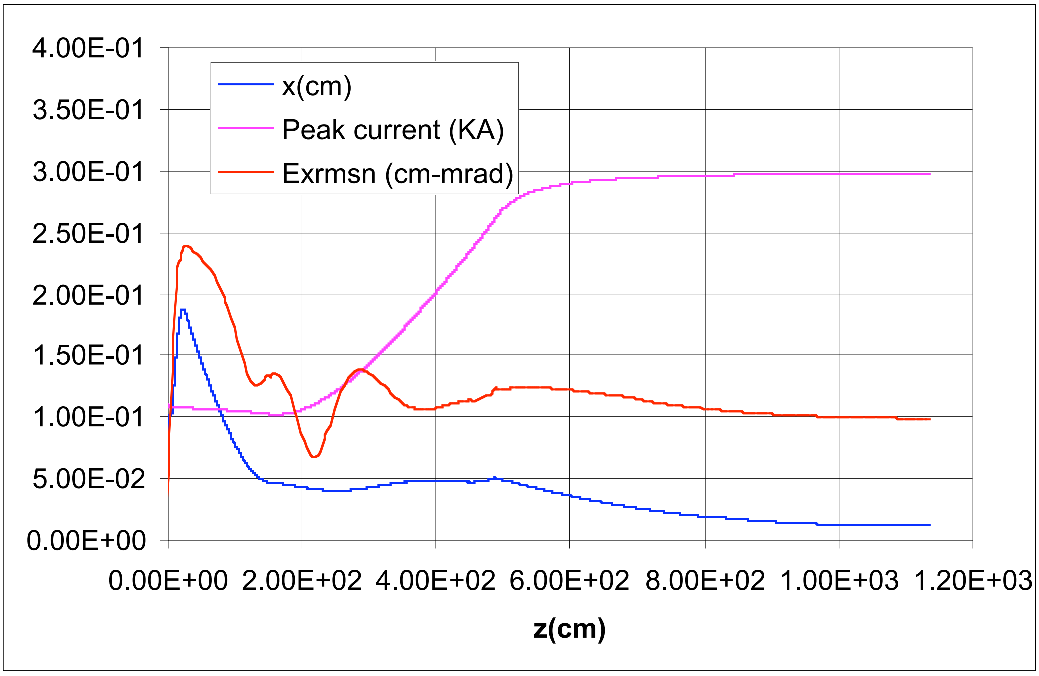

Figure 3.65: *Envelope, peak current, rms normalized emittance vs z.*

The slices analysis (Fig. 3.66) of the output beam shows that the larger contribute to the projected emittance is given by the head and the tail of the pulse, while the emittance of the central part of the bunch is limited to 0.5 □m. In addition it can observed that the bunch temporal distribution tends to a triangular shape: so the value of 300 A, that is simply scaled with the rms bunch length, is in reality an average current in the bunch corresponding to a larger value in the peak (about 500 A).

***Table 3.11**. Linac/solenoid design parameters for velocity bunching at SPARX.*

TW section	***I***	***II***	***III***
Gradient (MV/m)	15	25	25
Phase (deg)	-86	-37	0
Solenoid field (G)	1120	1280	0

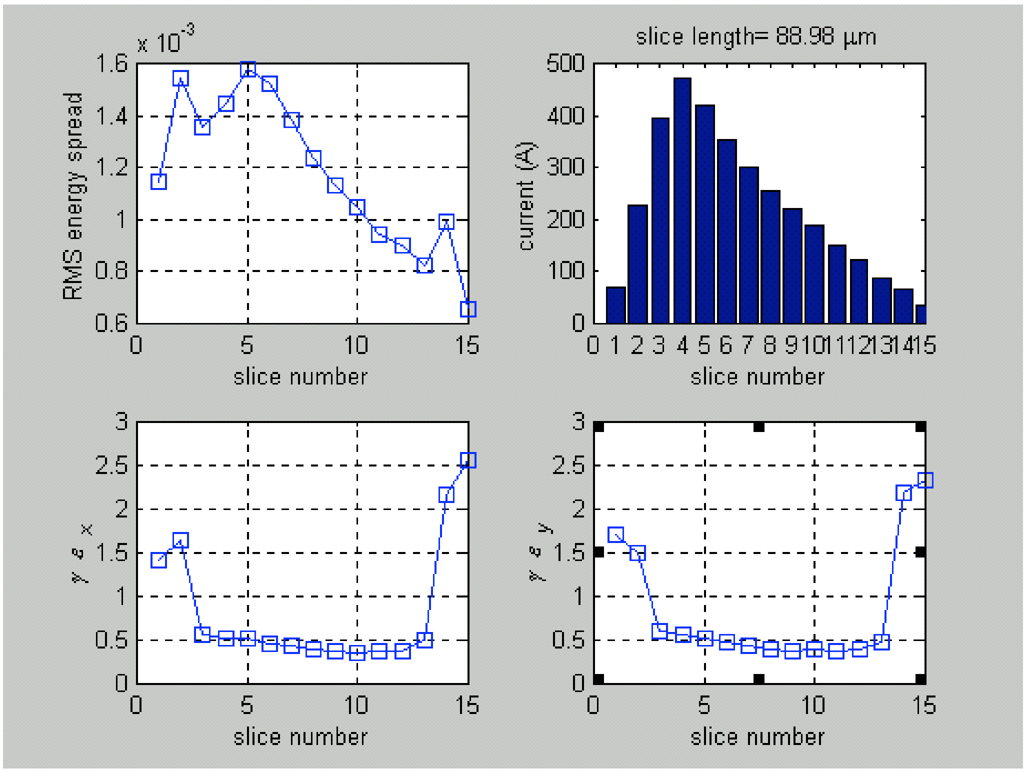

***Figure 3.66.** Slice analysis of the SPARX beam after the compression.*

A study of the sensitivity of peak current and emittance to phase jitter was done changing of ±1° the phase of the first TW structure. From the results shown in Table 3.12 it can be seen that changing the phase of ±1° produces a maximum variation of 13% in bunch length and 16% in normalized rms emittance.

***Table 3.12**. Velocity bunching phase fluctuation sensitivity.*

Phase of TW section I	**$\square_z$ (□m)**	**Norm. rms emittance (□m)**
-87	251	1.16
-86	289	1
-85	324	0.87

One of the relevant aspects of the velocity bunching integration in the SPARX project is the phase jitter sensitivity of the combined VB and magnetic chicane compression system.

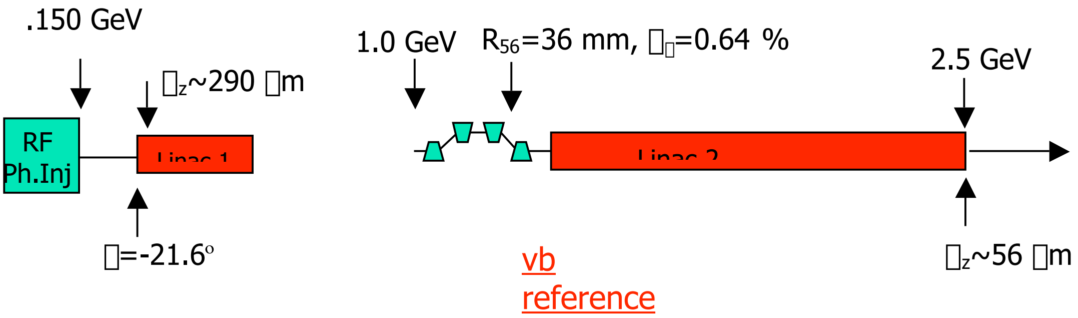

Figure 3.67. *Reference channel for the SPARX project.*

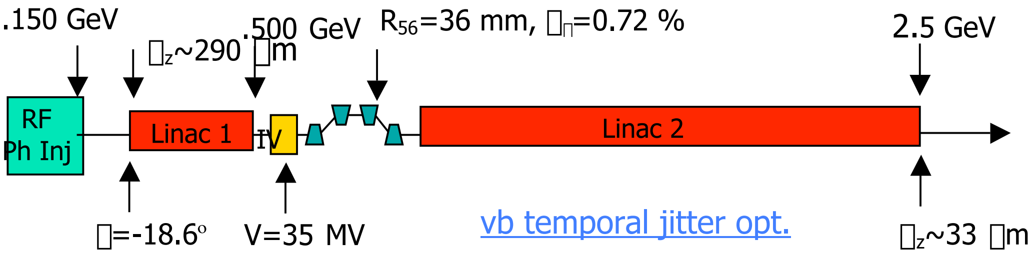

Figure 3.68: *Second layout with the temporal jitter optimization.*

The analysis has been performed dividing the channel in two parts: the RF compression stage and the rest of the channel that includes the high energy magnetic chicane. The first analysis has been devoted to the study and optimization of the channel downstream the RF compression system. Starting from the first channel layout, called “reference”, shown in Fig. 3.67, an “optimized “ channel has been developed that includes an X-band cavity to linearize the beam distribution before the second high energy magnetic compression stage, Fig. 3.68.

The goal was to find a setup of the channel that even with a timing error of 1 ps (1 deg) could reach the same final bunch length, Table 3.13 refers to the longitudinal analysis and optimization of the channel. With the help of the X-band cavity an increase in the bunch compression can be achieved without affecting the transverse emittance final value.

Table 3.13 *Optimization results for the velocity bunching SPARX channel.*

X_{band} Voltage (MV)	R56 (mm)	□ (°)	Energy@chicane (GeV)	□z (□m)	□z (□z=0.3 mm)	□□z (%)
35.0	37.28	18.6	0.51	30.5	30.6	0.5

The effect of a 1 ps temporal jitter, i.e. the laser pulse timing jitter, on the RF compressor has been analyzed first with the Parmela code, as discussed before, then the Parmela outputs have been tracked with Elegant on both the reference and the optimized channel and the results are reported in Tables 3.15 a) and b).

Table 3.15 a) *Summary table for the temporal jitter analysis on the optimized channel*

	$\square_z$(□m)	$\square_\square$(%)	$\square_{nx}$(□m)	$\square\square_z/\square_z$ (%)		
0	33.1	.15	3.0			
-1ps	31.8	.12	2.1	-3.9		
+1ps	36.0	.18	4.8	8.7		

Table 3.15 b): *Summary table for the temporal jitter analysis on the reference channel.*

	$\square_z$(□m)	$\square_\square$(%)	$\square_{nx}$(□m)	$\square\square_z/\square_z$ (%)		
0	56.0	.09	1.5			
-1ps	54.9	.11	1.0	2		
+1ps	57.9	.09	1.7	3.4		

These preliminary results show that the integration of a VB device in a higher energy linac with a second magnetic compressor stage do not cause additional concerns about the phase jitters. A more systematic analysis is under way in order to explore the full potentiality of such a hybrid scheme.

References

[1] M. Borland et al., “Start to end simulation of SASE FEL from gun through the undulator”, Nucl. Instr. & Meth. A 483 (2002) 268-272.
[2] J. Billen, “PARMELA”, LA-lUR-96-1835, 1996.
[3] E.Colby, “Design, Construction and Testing of a Radiofrequency Electron Photoinjector for the Next Generation Linear Collider, PhD Thesis, UCLA 1997.
[4] M. Ferrario et al. “Multi bunch energy spread induced by beam loading in a standing wave structure”, Particle Accelerators 52, 1 (1996)
[5] L. Giannessi, M. Quattromini, Phys. Rev. ST Accel. Beams 6, 120101 (2003)
[6] Y. H. Chin, “Advances and applications of ABCI”, Proc of PAC 93, Washington D.C. 1993.

[7] M. Borland, "elegant: A Flexible SDDS-Compliant Code for Accelerator Simulation" LS-287, ANL, Argonne, IL 60439, USA.
[8] CERN Report CERN/SL/90-13 (AP) (1995)
[9] S. Reiche, Nucl. Instrum. & Meth. A429,243 (1999).
[10] R. A. Jong, W. M. Fawley, and E. T. Scharlemann, "Modelling of induction-linac based free-electron laser amplifiers," in Modeling and Simulation of Laser Systems, Proc. SPIE 1045, pp. 18–27, 1989.
[11] S.G. Biedron, H.P. Freund, S.V. Milton, "3D FEL code for the simulation of a high-gain harmonic generation experiment, in: Harold E. Bennett, David H. Dowell (Eds.), Free-Electron Laser Challenges II, Proc. SPIE 3614, (1999).
[12] L. Giannessi, http://www.perseo.enea.it
[13] ENEA Report RT/INN/93/09 (1993).
[14] L. Serafini, J. B. Rosenzweig, "Envelope analysis of intense relativistic quasilaminar beams in rf photoinjectors: a theory of emittance compensation", Phys. Rev. E **55** (1997) 7565.
[15] J. Clendenin et al., "Reduction of thermal emittance of rf guns", SLAC-PUB-8284 (1999)
[16] S. G. Anderson and J. B. Rosenzweig, "Non-equilibrium transverse motion and emittance growth in ultrarelativistic space-charge dominated beams", Phys. Rev. ST Accel. Beams 3, 094201 (2000).
[17] M. Ferrario et al., "HOMDYN Study For The LCLS RF Photo-Injector", Proc. of the 2nd ICFA Adv. Acc. Workshop on "The Physics of High Brightness Beams", UCLA, Nov., 1999, see also SLAC-PUB-8400.
[18] Linac Coherent Light Source (LCLS) Conceptual Design Report, SLAC-R-593 (2002).
[19] M. Ferrario, K. Flöttmann, B. Grigoryan, T. Limberg, Ph. Piot, "Conceptual Design of the TESLA XFEL Photoinjector", TESLA-FEL 2001-3.
[20] ORION Technical Design Study, ORION006.
[21] M. Ferrario et al., "Recent Advances And Novel Ideas For High Brightness Electron Beam Production Based On Photo-Injectors",to be published in The Physics & Applications of High Brightness Electron Beams, J.Rosenzweig and L.Serafini ed., -World Sci.
[22] J. Yang et al., "Low-emittance electron-beam generation with laser pulse shaping in photocathode radio-frequency gun", J. of App. Phys. V 92, N. 3, 1608, August 2002.
[23] J. B. Rosenzweig et al.," Re-examination of the working point for the SPARC injector and SASE FEL", **SPARC-BD-03/004.**
[24] L. Giannessi, L. Mezi, C. Ronsivalle, M. Biagini, M. Migliorati, G. Di Pirro, "SPARC Transfer Line", **SPARC-FEL-03/006**
[25] F. Ciocci, G. Dattoli, L. Giannessi, "SPARC Undulator parameter set", **SPARC-FEL-03/003**
[26] F.Ciocci, G. Dattoli, A. Doria, G.P. Gallerano, L. Giannessi, E. Giovenale, G. Messina, L. Mezi, P.L. Ottaviani1, L. Picardi, M. Quattromini, A. Renieri, C. Ronsivalle, "SPARC FEL Working Point And Undulator Configuration" **SPARC-FEL-03/001**
[27] M.E. Biagini, M. Boscolo, M. Ferrario, V. Fusco, M. Migliorati, C. Vaccarezza, L. Giannessi, L. Mezi, M. Quattromini, C. Ronsivalle , S. Reiche, J. B. Rosenzweig, "Sparc Injector Working Point Optimization", **SPARC-BD-03/007.**

[28] S. Reiche, “Review of Application to SASE-FELs”, in Proceedings of the ICFA Workshop “The Physics and Applications of High Brightness Electron Beams” Chia Laguna, Sardinia, July 1-6, 2002
[29] A. Tremaine, et al., "Experimental Characterization of Nonlinear Harmonic Radiation From a Visible SASE FEL at Saturation", *Phys. Rev. Lett.* **88,** 204801 (2002)
[30] C. Limborg, “New optimization for the LCLS photo-injector”, Proc. Of EPAC-02
[31] C. Ronsivalle,” Study Of Tolerances And Sensitivity To Errors In The Sparc High Brightness Photo-Injector”, **SPARC-BD-03/008.**
[32] M. Ferrario, V. Fusco, M. Migliorati, B. Spataro, **SPARC-BD-03/009.**
[33] F. Zhou, I. Ben-Zvi, M. Babzien, X. Y. Chang, A. Doyuran, R. Malone, X. J. Wang, and V. Yakimenko , “Experimental characterization of emittance growth induced by the nonuniform transverse laser distribution in a photoinjector”, Phys. Rev. ST Accel. Beams 5, 094203 (2002).
[34] R. Carr et al., “Visible-infrared self-amplified spontaneous emission amplifier free electron laser undulator”, Phys. Rev. ST Accel. Beams 4, 122402 (2001).
[35] S. Anderson, J.B. Rosenweig et al. “ Space-charge effects in high brightness electron beam emittance measurements”, Phys. Rev. Special Topics – Acc. and beams, Volume 5, 014201 (2001).
[36] M. Zhang “Emittance Formula for Slits and Pepper-pot measurement”, FERMILAB-TM-1998
[37] D.H. Dowell “Bellows-Induced Wakes in the Pepper Pot Experiment”, private communication.
[38] K.Bane M. Sands, “Wake Fields of Very Short Bunches in an Accelerating Cavity”,SLAC-Pub-4441
[39] D.H. Dowell *et al*, “Slice Emittance Measurements at the SLAC Gun Test Facility”, SLAC-PUB-9540, September 2002
[40] J.F. Schmerge *et al*, “Transverse-emittance measurements on a S-band photocathode RF electron gun”, Nucl. Instr. & Meth. A 483, 2002, pp. 301-304
[41] X. Qiu *et al* ,”Demonstration of Emittance Compensation through the Measurement of the Slice Emittance of a 10- ps Electron bunch”, Phys. Rev. Lett. 76, 20, 1996, pp. 3723-3726.
[42] L. Serafini, M. Ferrario, “Velocity Bunching in PhotoInjectors” , AIP CP 581, 2001, pag.87.
[43] P. Emma, “Accelerator physics challenges of X-rays FEL SASE sources”, Proc. Of EPAC-02, Paris 2002.
[44] M. Boscolo et al., "Beam Dynamics Study of an RF Bunch Compressor for High Brightness Beam Injectors", Proc. of EPAC2002, Paris.
[45] L. Serafini, M. Ferrario, A. Bacci, “Ultra-Short Electron Bunch Generation with Rectilinear Compressor” Proc. Of PAC 01, Chicago 2001.
[46] D. Alesini et al., “Conceptual Design of a High-Brightness Linac for Soft X-ray SASE-FEL Source”, Proc. Of FEL Conf., Chicago 2002.

4. Injector Components

4.1 OVERVIEW

The SPARC system will be constructed in an existing hall of LNF, following the general scheme given in the drawings presented in the appendix to this document. The layout of technical components will be shown in detail in the SPARC Injector Technical Layout, which is now under preparation. The main technical components are: the SPARC advanced photoinjector with S-band RF system, the UV laser, the laser room, a bypass line for beam diagnostics and magnetic compression, a 15 m long undulator for FEL-SASE experiment, a control room, and RF power plant area. These subsystems are discussed in this chapter. The SPARC hall and nearby auxillary rooms must be equipped with adequate water and power infrastructure, which are described in a later chapter.

4.2 RF GUN

The RF photocathode gun and associated systems are meant to reliably produce, at the most critical point in the injector, the extremely high quality beam demanded by the SPARC project. As such, it must be based on technology that is both proven and at — but not beyond — the cutting edge. These same considerations apply to a critical accompanying component, the photocathode drive laser. In order to acquire this type of technology in the case of the RF gun and its associated emittance compensation solenoid, we will rely on the UCLA Particle Beam Physics Laboratory, or PBPL, group (SPARC collaborator J. Rosenzweig, director) to produce the device itself. The PBPL group has produced nine previous versions of the high-gradient 1.6 cell 2856 MHz RF gun (the BNL/SLAC/UCLA design), and thus has a proven track record in producing such high performance devices.

In this section, we review the RF gun and solenoid assemblies; the photocathode drive laser is discussed in the following section, and most of the beam simulations relevant to gun and solenoid design are presented in the previous Beam Dynamics section. We discuss below the overall philosophy of the gun design, and details of the design including photocathodes, gun manufacturing and tuning methods, and the emittance compensation solenoid design that allows for flexibility not only in the focusing strength of the magnet, but in its longitudinal center.

***Table 4.1**- SPARC RF Gun characteristics*

Peak electric field on cathode	120-140	MV/m
Beam pulse duration (full width)	3-12	ps
Output energy	7	MeV
Frequency	2856	MHz
Repetition (max)	10	Hz
RF pulse duration	4.5	μs
RF peak power	15	MW
RF average power	700	W
Temperature	45	°C
Vacuum (RF on)	10^{-9}	Torr
Cathode insert diameter	12	mm
Laser spot diameter	2	mm
Cathode material	Cu (Mg)	
Q.E. @ 266 nm	10^{-5} (10^{-4})	
Charge	1	nC
Laser pulse energy	500	μJ (50 μJ)
Laser incidence angle	72	deg
Peak solenoid field	3.1	kG
Solenoid current (0.6 mm H_2O cooled winding)	200	A
Solenoid dissipation	4	kW

4.2.1 Performance parameters

The parameters of the SPARC RF gun are shown in Table 4.1. These parameters are consistently derived from both previous experience at existing labs that have used versions of the 1.6 cell gun (UCLA Neptune, BNL ATF, BNL SDL, SLAC GTF, LLNL PLEIADES), and from detailed simulations that are discussed in the Beam Dynamics section.

The parameters given need some additional clarifying comments, in that many of them represent outer envelopes of expected performance. For example, the RF gun peak field is listed as 140 MV/m (the nominal LCLS injector), while the present plan for SPARC running is only at the 120 MV level. Further, the maximum power foreseen for exciting the gun (15 MW) is based on this maximum quoted field. This peak power yields an average power at the design duty cycle (repetition rate limited by the laser system) which is well within the standard 1.6 cell gun design thermal handling capabilities.

The other notable parameter that has a wide built-in safety margin is the quantum efficiency (QE) of the photocathode, which in the case of both single-crystal copper and magnesium, is one order of magnitude below that achieved under careful conditions, and in fact represents the lowest ever QE observed for these materials, even under fields well below those specified, where it is expected that the Schottky effect can lead to large enhancements of the QE.

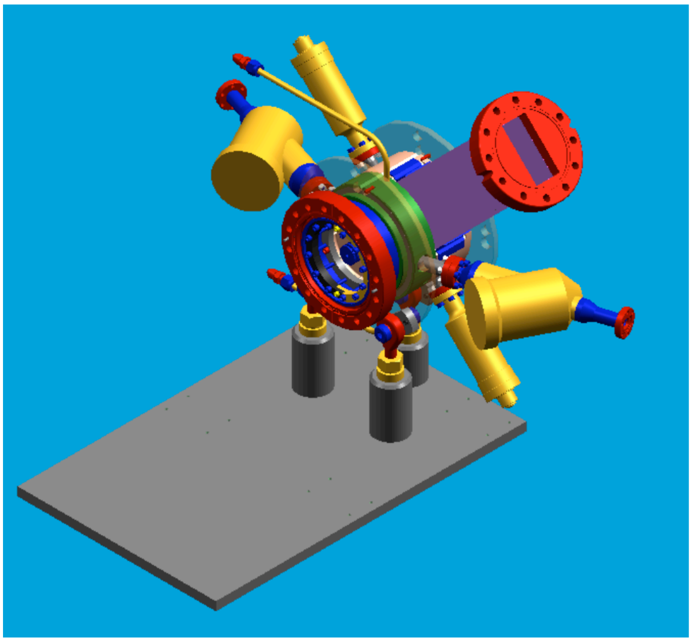

Figure 4.1: *Three-dimensional rendered drawing (rear view) of ORION version of the 1.6 cell RF photocathode gun and related vacuum and waveguide components and ports. All access flanges removed for viewing purposes. (courtesy D. Palmer, SLAC ARDB)*

4.2.2 The 1.6 cell high-gradient RF photocathode gun

Figure 4.1 shows a schematic 3D rendered drawing of the most recent generation of 1.6 cell S-band RF gun, a model developed for the ORION project that corrects some known deficiencies in previous performance of the original BNL/SLAC/UCLA version. The RF power waveguide, visible on the upper right, is coupled to the full cell, and vacuum is pumped through a symmetrizing port. Also symmetrically placed in the full cell are the two tuners, at 90 degrees with respect to the waveguide (the upper one is visible), and the entrance and exit laser ports, half way between waveguide and the vacuum ports. The beam exit port is on the front of the picture. The symmetry of the structure determines that of the electromagnetic field distribution, and it is important to avoid dipolar excitation components; the lowest perturbation of the RF mode is limited to quadrupole, with negligible effect on the beam dynamics.

The photocathode insert is centered on the wall of the flange that terminates the half-cell. In the first phase of the project it is planned to use a single-crystal Cu cathode insert, a material with well proven photo-emissive behavior that guarantees improved uniformity of the emission distribution over the spot illuminated by the laser. Its drawback is the low emission efficiency, which entails large laser pulse energy. The Mg cathode foreseen for use in the later phase of the project has larger emission efficiency but lower distribution uniformity and it is more difficult to handle.

Both types of cathodes demand very good vacuum, at the level of 10^{-9} Torr during high gradient operation, which typically implies that the vacuum without RF be one order of magnitude better in the absence of rf power. These demands are to be met by stringent control of the gun manufacturing process, and by implementing as much pumping on the gun as possible: through the direct pumping port, through the waveguide, at the beam port, and behind the cathode plate through an array of small pumping holes. In addition, it is foreseen that both cathode materials must be laser cleaned *in situ*, a process which was pioneered at BNL, and entails a scan of the laser over the cathode surface at sub-damage-threshold powers. This process has now been well documented, and may be relied upon to vastly improve the quantum efficiency, and its spatial uniformity.

Laser injection is accomplished through the 70 degree ports shown in Fig. 4.1. This scheme requires time-of-flight correction of the laser pulse, but simplifies the beam-line downstream of the RF gun, allowing more room for pumping and beam diagnostics, and improving the vacuum by removing laser optics (also allowing more effective bake-outs to be performed).

The ORION version of the 1.6 cell gun shown in Fig. 4.1, jointly developed by UCLA and SLAC, represents a recently implemented effort to improve the performance of the device. As the RF fields are very large, control over the alignment of the electromagnetic axis in the gun is critical; small errors in position lead to large errors in alignment. By using brazed-on stainless steel holding rings to attach to a three-point kinematic support, much more rigorous control over the gun positioning is obtained. In addition, a complete review of tuner design (a source of breakdown in some previous guns) and machining/brazing procedures has been performed in the ORION gun design and manufacturing effort.

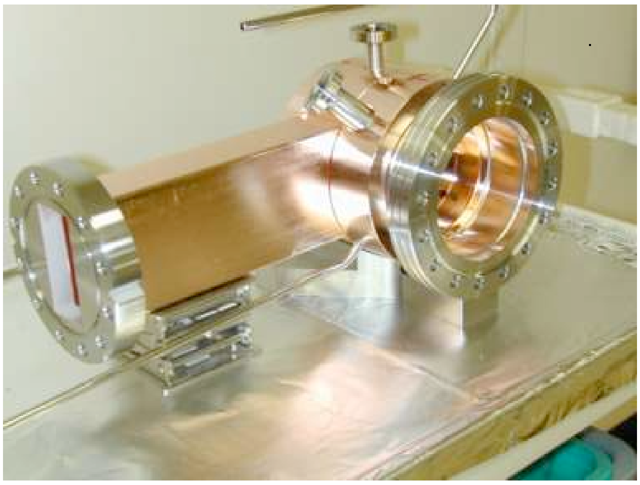

Figure. 4.2: *UCLA Neptune spare RF gun after recent (10/02) final brazing at SLAC.*

It should be noted that the process used in producing the ORION gun, as well as many of the previous versions of the gun, will be replicated for the SPARC gun: machining and all RF testing will be performed at UCLA, while the brazing is to be undertaken at SLAC (see Fig.4.2). UCLA has extensive network analyzer and related RF testing facilities that have been built up for RF cavity production. It is planned that

INFN collaborators come to UCLA to participate in the tuning process, and learn techniques such as field balancing (see Fig. 4.3) that may be needed upon substitution of cathode plates.

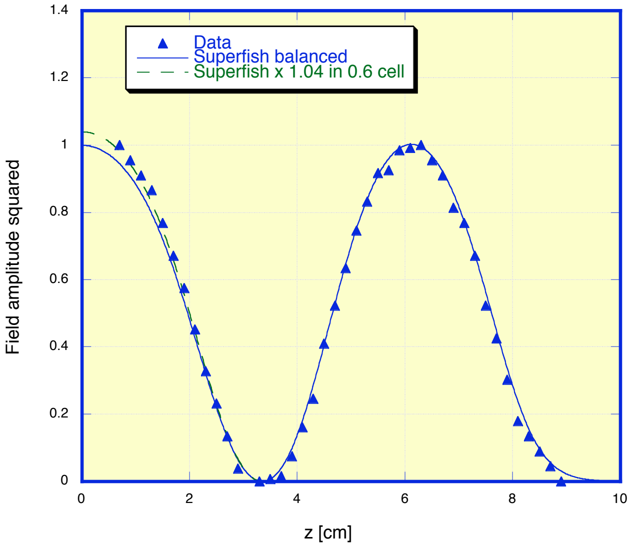

Figure 4.3: *UCLA Neptune spare RF gun field balance data, from bead-drop technique, and comparison to SUPERFISH model, showing 2% field imbalance between full and 0.6 cells. (Courtesy J. Rosenzweig, UCLA)*

UCLA is expected to provide, under contract from the INFN, the RF gun hardware up to, but not including the RF window at the waveguide, and also including the gun supports. The engineering drawings of the gun will be provided by UCLA to document the gun fabrication and modification/tuning process. This will enable INFN to make subsequent improvements or changes to the gun as needed, and help build up the local SPARC team expertise in high gradient RF cavity development.

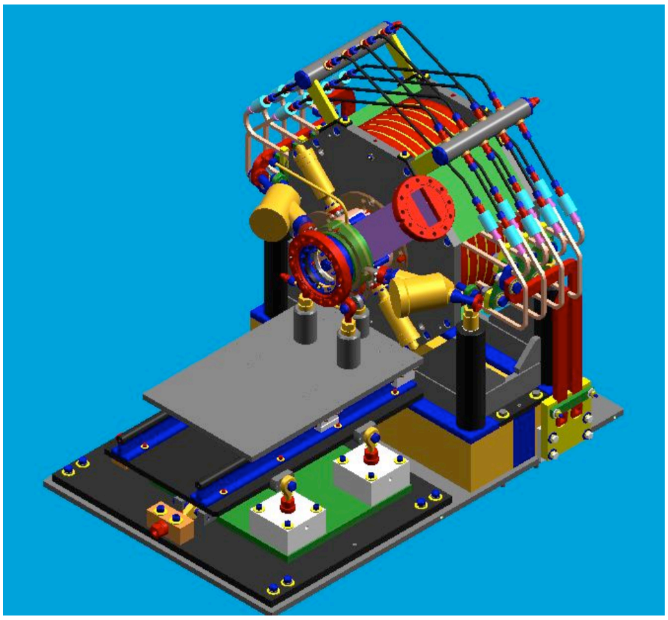

Figure 4.4*: Three-dimensional rendered drawing (rear view) of ORION 1.6 cell RF gun assembly, with downstream solenoid and associated supports.*

4.2.3 The emittance compensation solenoid

In terms of active beam-manipulation components, the RF gun is followed by the emittance-compensation solenoid, as shown for the ORION case in Fig. 4.4. The solenoid assembly is a large, multi-coil (8 pancake device) with field-stiffening inserts, and is bulky and expensive to build. For the SPARC project it has been decided by UCLA and INFN to explore a new solenoid design that, unlike the gun design, has not been re-examined in the past six years. The reasons for this change are both in the SPARC beam dynamics experimental program, which requires the possibility of adjusting the longitudinal position of the solenoid field, and in practical construction considerations. The design philosophy for BNL/GTF/LEUTL/ORION solenoid, as originally proposed by X. Wang of BNL, was originally adopted to produce a very spatially uniform solenoid field. It has been found that there is no beam dynamics advantage to obtaining such a uniform field, which in any case can be obtained in a simpler way, using fewer coil modules. Further, the heavy assembly does not easily lend itself to placement on a precision mover.

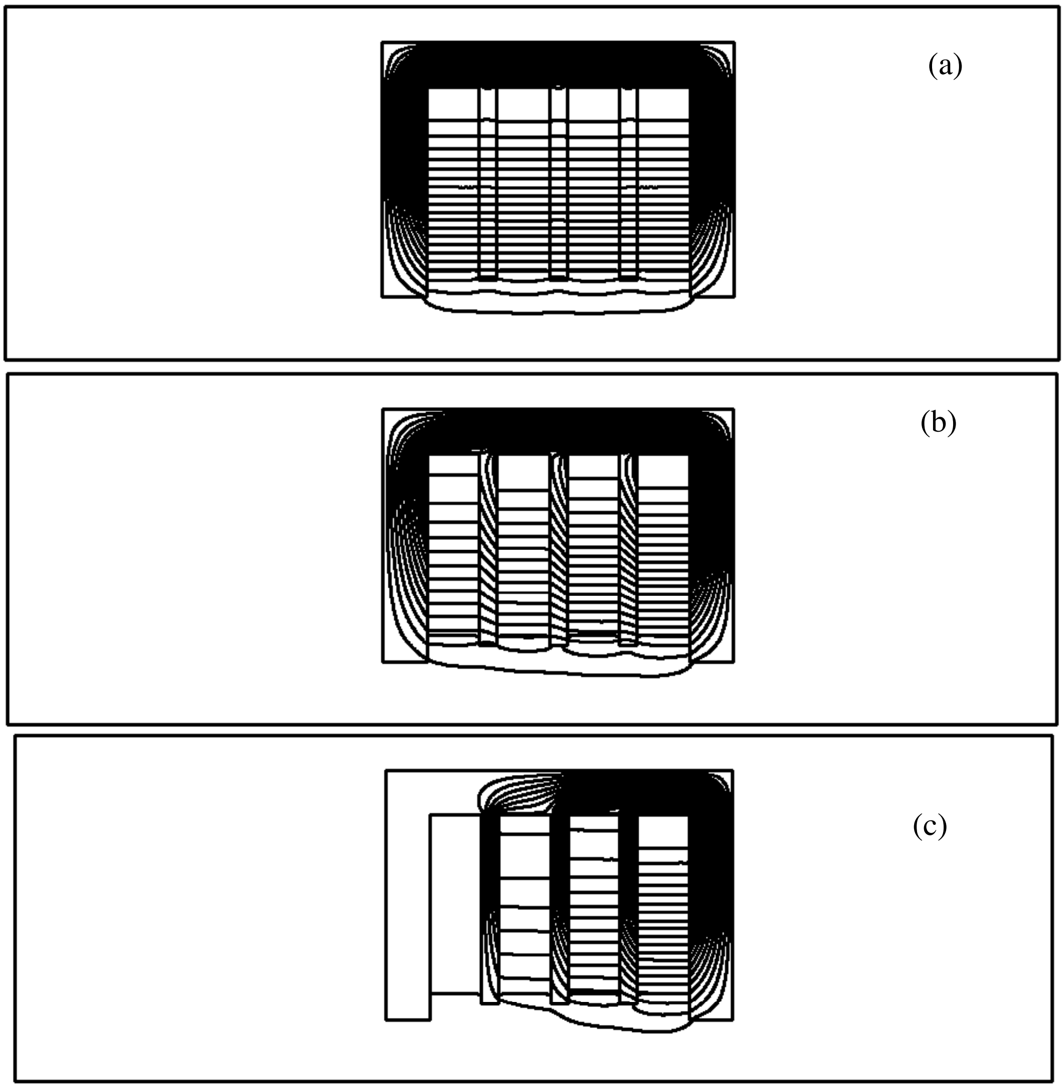

***Figure 4.5**: The proposed four-coil solenoid, with (a) flat field profile excitation, (b) 38% excitation difference across the magnet, and (c) 100% difference.*

This design can be made more robust and more appropriate for SPARC, by going to a four-coil assembly, as shown in the POISSON output of Fig. 4.5. The four-coil assembly has three field-stiffening inserts, which allow production of a very flat field, as seen in Fig. 4.5. This assembly can reproduce the field flatness of the now-standard BNL design (Fig. 4.6) which is important for benchmarking experimental results from SPARC against similar facilities —recall that the beam dynamics for SPARC are nominally nearly identical in Phase I to the LCLS (GTF) photoinjector, being based on the Ferrario working point. It can be seen that the field profile for the two designs are nearly identical, with the new design actually being slightly more uniform, due to use of smaller end-cap inner radius in the SPARC case. Simulations indicate that the two designs are functionally equivalent from the beam dynamics viewpoint.

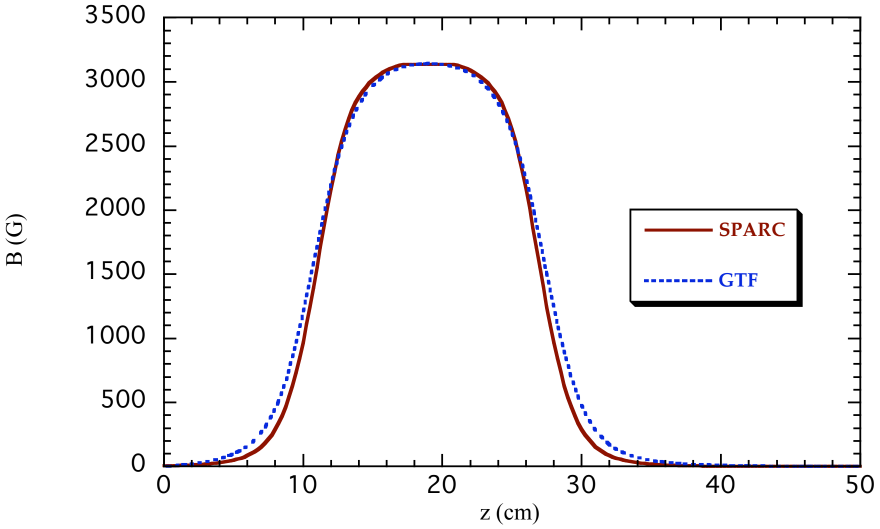

Figure 4.6*: Comparison of four-coil solenoid (SPARC) against standard BNL-style GTF solenoid (GTF), with new solenoid run at current of 120 A for 120 MV/m gun operation.*

The most compelling feature of this new design is in fact adjustability of the longitudinal position of the lens center, however, in which case we introduce unequal currents in each coil, linearly ramping them up or down in *z*. This scheme was originally introduced in the Neptune photoinjector using two iron-separated coils. The gradient in currents may limited by the saturation of the field stiffeners, but this is avoided in the proposed design, and one may obtain 100% variation from beginning to end. The fields produced by the flat, ramp-up and ramp-down excitation (with only 38% current variation in the coils) of the four coils are shown in Fig. 4.7. They produce a shift of over 2.2 cm in the center of the lens (as weighted by the focusing strength $K \quad B^2$) for the relatively modest asymmetry in the coil currents.
Introduction of this type of tunability by physically moving the entire solenoid assembly was studied, but the adopted scheme was found to be more flexible, and more robust from the viewpoint of maintaining gun EM axis to solenoid magnetic axis alignment.

We note further that the beam dynamics indicated by this approach to moving of the lens appear to be robust, as shown in the HOMDYN simulations of Fig. 4.8. These simulations represent a first pass at a study of emittance compensation using this solenoid scheme. They show that a notable tuning of the emittance compensation dynamics can be obtained through this field centroid variation (which held the integrated field constant). This tuning is functionally equivalent to moving the solenoid, but implemented by a simpler, less expensive method. It is also, notably, faster, which is a key advantage in making parametric scans during experiments.

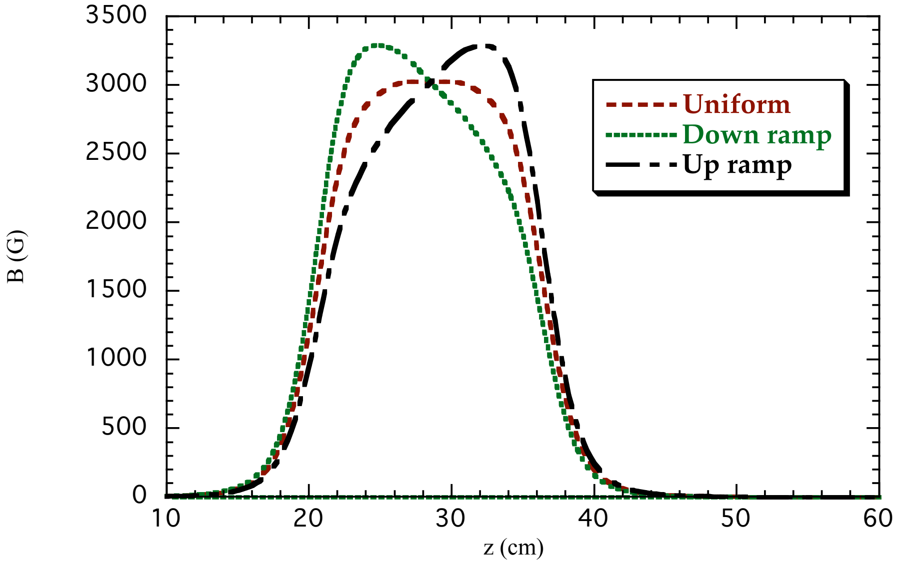

***Figure 4.7**: Comparison of the field profiles obtained from the flat, ramp-up and ramp-down excitations of the proposed solenoid concept, with 60% increase in current excitation between minimum and maximum strength coils.*

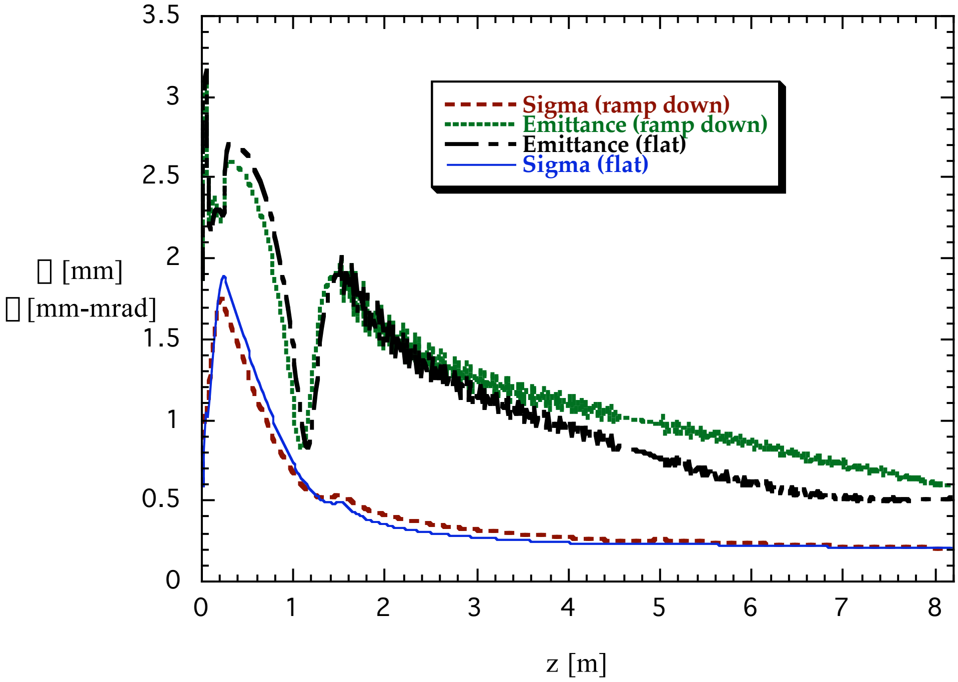

***Figure 4.8**: Comparison of the rms beam size and emittance evolution in the SPARC injector (no velocity bunching), between flat and ramp-down solenoid settings.*

While this design is still being finalized at UCLA, it seems that it is reasonable from the iron and coil points of view. The coils are envisioned to be 0.625 cm square, water-cooled, and run at 120 A for the flat-field case, and below 200 A in the 100% variation of current case (up-ramp case), which is still within tolerances for the maximum current. The ramp-down case would not be able to access 100% variation, because one needs more focusing when it is effectively closer to the gun. This is not viewed as a problem for the experimental operations, as there is no scenario where one expects to need such extreme variation in the lens effective position in any case.

A fully engineered system based on this design philosophy is now underway at UCLA, which is also expected to produce (under contract with the INFN) the iron portion of the solenoid, and the support assemblies, and procure the water-cooled coils and their water manifolds. Engineering drawings of the solenoid and support assemblies will be produced for fabrication use and also delivered to INFN. Particular attention will be paid to relative alignment of the solenoid; this task will be based on the previous work done for the ORION and UCLA Neptune solenoids and guns. It is anticipated that a pre-measurement of the solenoid using pulsed wire techniques should allow determination of the solenoid magnetic center with good accuracy. The solenoid will then be mechanically aligned using monuments on the iron to the remainder of the downstream beamline. Initially steering measurements on the beam using two BPMs after the solenoid based on variation of the solenoid current should allow determination of the gun axis misalignment with respect to the solenoid. With this information, small changes in the rf gun alignment will be performed as needed. This process may be iterated as necessary.

4.3 PHOTOCATHODE DRIVE LASER SYSTEM

Photocathode drive lasers for high brightness electron beam applications must have very specific capabilities driven by two major considerations: (1) the low photo-emission efficiency for robust photocathodes requires high UV pulse energy given the needed charge; and (2) the emittance compensation process is most successful with uniform temporal and spatial laser energy distribution. Additionally, low amplitude and time jitters from pulse-to-pulse, as well as pointing stability are needed to assure repeatable SASE-FEL performance. The laser pulses have to be synchronized with the SPARC master oscillator, in order to extract electrons at the specified phase of the RF wave. The allowed variations in parameters concerning the laser system and its relationship to the rf system have been specified with the aid of the PARMELA and HOMDYN simulation codes, as discussed previously in Chapter 3.

The drive laser supplies photons that are absorbed by electrons within the RF gun cathode, producing via the photo-electric effect emitted electrons if their kinetic energy exceeds the material's work function. The energy per laser pulse U (J) needed to produce a bunch of charge Q (C) using photons of energy E_γ (eV) incident on a cathode surface with quantum efficiency η (electrons emitted per incident photon), is given by $U = QE_\gamma/\eta$. A cathode's quantum efficiency depends on many conditions, such as material, preparation, excess of photon energy over the work function, RF field and vacuum levels. Nevertheless, we may extrapolate the needed performance of the photocathode drive laser from previous experiment at other labs. Assuming a typical value of $\eta = 10^{-5}$ for copper, 50 μJ is required to produce a 1 nC bunch; allowing for a energy overhead of one order of magnitude, this implies 500 μJ of laser energy. This required value at the photocathode must be considerably larger at the harmonic-generation crystal exit, as light will be absorbed by various optical elements needed for pulse shaping transport to the photocathode.

4.3.1 SPARC laser performance

The laser system for SPARC is required to deliver a 500 μJ pulse of 266 nm wavelength photons to the photo-cathode at a repetition rate of 10 Hz. According to theory and simulation, the emittance compensation scheme requires a laser pulse with transverse and longitudinal profiles that are as uniform as possible. In fact, temporal and spatial flat top laser energy distribution on cathode has been demonstrated to reduce the emittance in recent experiments as well. Additional demands are placed on the longitudinal (time) laser profile by the demand for the capability of changing the pulse length over a range from 2 to 10 ps to control the charge and peak current.

In order to define in details the operational performances of the laser we carried out beam dynamic simulations. Using the PARMELA code we have investigated the effects of non-ideal characteristics of the laser pulse on the emittance growth. PARMELA simulation on the effects of non zero rise-fall has been performed starting from a thermal emittance of 0.3 mm-mrad, a peak field on cathode 120 mV/m and a magnetic field 0.27 T. As shown in Fig 4.9 at the end of the photo-injector (8 m), with a 1 ps (10-90%) rise and fall time, the emittance grows to 1 mm-mrad, which still an acceptable value. Slice emittance analysis points out that the SASE saturation is achieved within 10 m undulator length for 81% of the beam for 1 ps rise-fall time, and 94% in the case of no rise time.

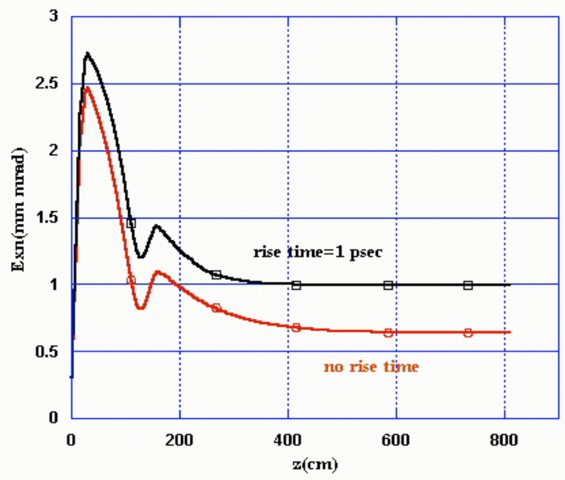

***Figure 4.9**: Emittance evolution along the photo-injector for 1 ps rise-fall time (upper curve) and no rise time laser pulse shape.*

The correlation between the emittance performance and the variation from ideal parameter, such as energy jitters, elliptical laser spot on cathode, time jitters, were also studied with the aid of HOMDYN code. The working point was set at 1 nC, 35° of the accelerating field phase, and circular 1 mm radius spot on cathode. In terms of amplitude jitter, the results show that the emittance growth is limited to 4% and 7% for charge variation of 5% and –5% respectively. The linear dependence between laser UV energy and extracted charge means the same value for the pulse-to-pulse UV energy jitter tolerance. Simulations on timing jitter have demonstrated that the emittance variations are 4% for 1 ps time jitter between RF phase and laser pulse. The issue of timing jitter becomes more critical when one considers magnetic and velocity bunching, however.

It has been proven that laser beam's grazing incidence on metallic cathode improves its quantum efficiency by 4-6 times[1]. For off-normal incidence the circular laser spot becomes an ellipse on the cathode, losing the symmetry with the electric field in the gun. As reported in the beam dynamic chapter the emittance grows up to 10% and 50% respectively, for 10% and 20% of the ratio between the ellipse axes. That implies the necessity of an optic compensation to maintain the circular distribution on the cathode.

Other important operational demands are high energy and pointing stability for repeatable SASE-FEL performances. To meet the requirements for the SPARC injector the pointing jitter tolerance should to be less than 50 µm in order to guarantee electron beam trajectory errors at the 1▯ level.

In Table 4.2 we summarize the requirements for the laser parameters.

Table 4.2. *Laser requirements on cathode.*

Parameter	Requirement
Operating Wavelength	260 nm
Pulse energy on cathode	500μJ (□$=10^{-5}$)
Energy jitter (in UV)	5 % rms
Temporal pulse shape	Uniform (20% ptp)
Transverse pulse shape	Uniform (20% ptp)
Pulse rise time (10-90%)	< 1 ps
Pulse length	2-10 ps FWHM
Repetition rate	10-20 Hz
Laser-RF jitter	< 1ps rms
Spot diameter on cathode	Circular 1 mm radius

4.3.2 Laser system description

The optimum choice that we have found for satisfying the required laser performances is to use a commercial, frequency-tripled Ti:Sa laser. In fact the Ti:Sa (Ti:Al_2O_3) crystal is able to produce a bandwidth large enough to perform the time pulse shaping, and can support the high energy required in SPARC application. The Ti:Sa crystal has the optical absorption peak between 490 and 540 nm, which sets the pump requirements. The emitted wavelength can be tuned with optical filters on a large fluorescence band of the material (700 to 1100 nm) but the most efficient wavelengths are between 780 and 800 nm. The bandwidth of the emitted pulse depends on the set-up of the oscillator cavity. Since the duration of the emitted pulse is inversely proportional to the bandwidth, the Ti:Sa laser is capable of producing pulses from 10 fs to picoseconds.

The proposed layout for the SPARC laser (Fig. 4.10) consists of a frequency-doubled CW 10 W diode-pumped Nd:YVO_4 to pump the Ti:Sa oscillator. The oscillator is chosen to work in a mode locking regime at 780 nm, with 100 fs transform-limited pulses. The typical energy per pulse is 10 nJ at the exit of oscillator. The repetition rate of the oscillator is chosen by varying the cavity length; we propose to use an optical cavity length of 1.8 m with a repetition rate of 79.333 MHz. This frequency corresponds to the 36th sub-harmonic of the S-band RF accelerating field. A dedicated synchronization system must lock the repetition rate to an external master clock moving the oscillator's end mirror. Two Ti:Sa amplification stages are needed to enhance the energy up to 20 mJ at the 780 nm wavelength, with a gain approaching 10^8 when one takes into account losses in phase manipulation (as reported later) and stretcher-compressor. In fact, we have estimated that the losses from 3rd harmonic generation, the transfer line and the following pulse manipulations reach 97.5%, giving maximally 0.5 mJ on the cathode. This value is an order of magnitude larger than the specification, thus allowing even for unanticipated losses and/or anomalously poor quantum efficiency.

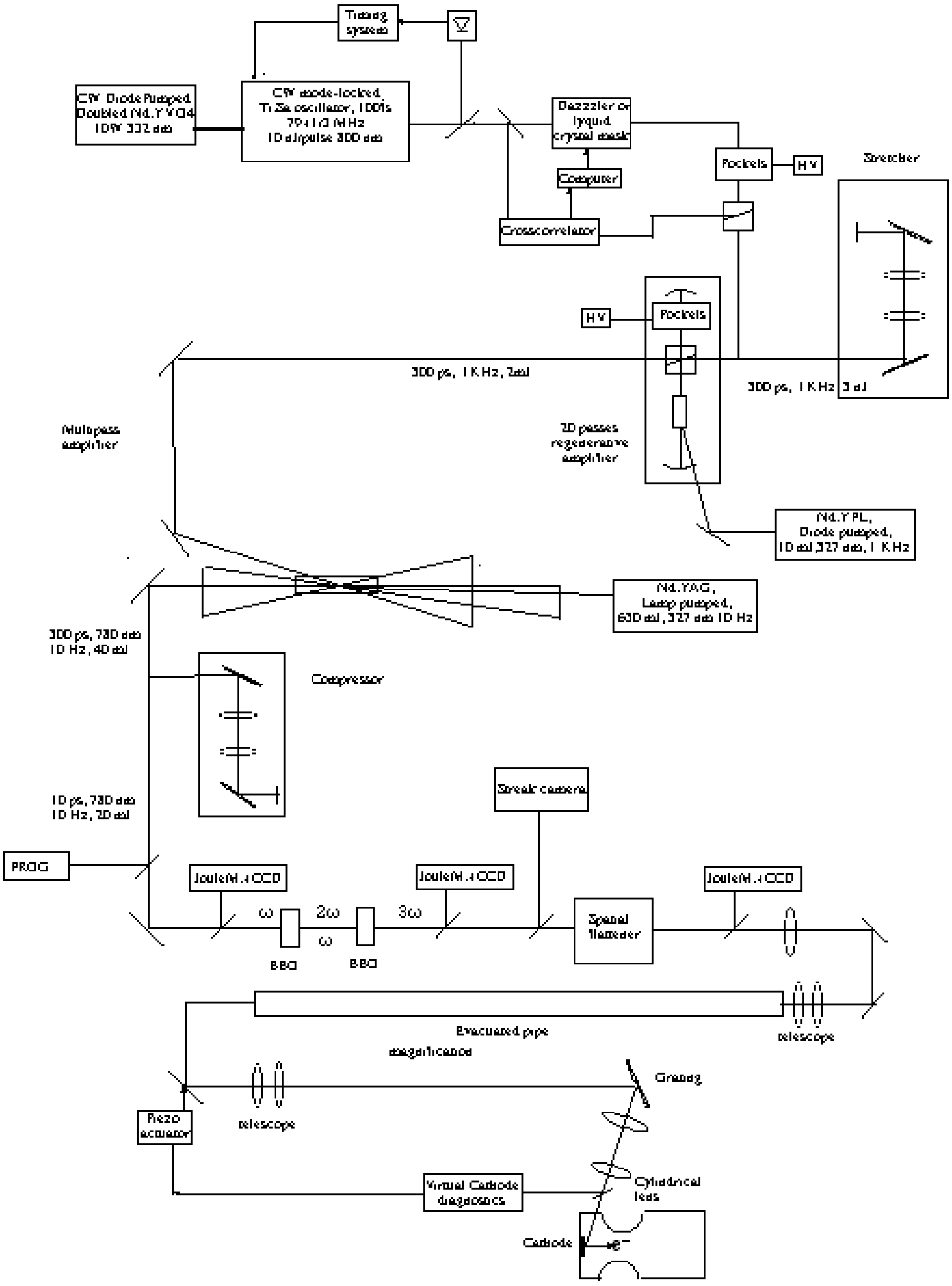

Figure 4.10. *Laser system layout.*

A regenerative pre-amplifier and a multipass stage compose the most reliable scheme for the high power section of the laser system. A 1 KHz 10 mJ and a 10 Hz 600 mJ green pumps may be used to excite these amplifiers. The maximum repetition rate of the regenerative and the multipass amplifiers are limited at 1KHz and 10 Hz, so that a pulse picker between these two stages is needed. The pulse-to-pulse energy jitter produced by commercial high-energy amplifier is limited to 1.5% rms. In amplifiers for sub-picoseconds pulses, the peak power must be limited to avoid damage to optical components using chirped pulse amplification. For this purpose, a grating pair is used to introduce a high linear dispersion for the different frequency components of the pulses. In this way, the 10 ps from the pulse shaper can be stretched to 500 ps. After the amplifiers a grating pair in parallel arrangement provides complete compensation of the dispersion introduced by the stretcher. At the exit of the compressor the pulse has the same duration as at the input. Because of the high diffraction orders generated by the grating the compressor introduces a 50% energy loss. The commercial laser systems provide a pointing stability less than 2 μrad per hour with proper temperature stabilization.

4.3.3 Manipulation of the Pulse Energy and Distribution in Time

As discussed earlier, the need to minimize nonlinearities in the space charge field of the electron bunch, in particular during the early stages of acceleration from the photo-cathode surface, leads to a request for shaping the temporal profile of the laser pulse as it strikes the photo-cathode - the required shape is a uniform intensity distribution in time, often termed a flat-top time distribution. The transverse intensity distribution has to be uniform as well; this can accomplished by aperturing (perhaps with soft aperture techniques), and relay imaging, or by use of nonlinear focusing schemes, as are discussed in the following section. Beam dynamics simulations, discussed in Chapter 3 show that flat-top profile should exhibit very sharp edges in the head and tail of the pulse: the associated rise times must be at least shorter than 1 ps, with 0.5 ps being a desirable optimum value.

The 100 fs pulses delivered by Ti:Sa laser oscillator naturally display a Gaussian temporal profile. It is possible to manipulate the spectrum such a pulse, producing in the frequency domain f a $sin(2\pi Tf)/f$ function that corresponds to the required flat-top (square wave) time-profile with duration T. The devices performing this manipulation typically have high insertion losses and low damage thresholds: therefore this pulse manipulation, as well as the whole laser pulse shaping procedure, has to be applied before amplifying the laser pulse in the amplifier chain (regenerative + multi-pass). In this layout only phase modulation can be performed to preserve the entire bandwidth and maintain the stretcher efficiency. As a matter of fact, if amplitude modulation were applied, filtering out spectral components and reducing the spectral bandwith, for T=10 ps the spectrum of the $sin(2\pi Tf)/f$ would be reduced by two orders of magnitude, and in order to amplify the laser pulse a stretcher as long as tens of meters would be needed. On the other hand, applying just phase modulation makes possible to retain the full spectral bandwidth of the laser pulse produced by the oscillator. Phase modulation is applicable because only the intensity profile of the output pulses must be specified: this is actually the only important factor since the phase profile has no consequence in electron photoemission. Preliminary simulations seem to indicate that the required profile can be obtained with only a phase modulation system. A Pockels cell and a polarizer are used after the pulse shaper to deflect a 1 KHz pulse train to the regenerative amplifier and all other pulses to the diagnostic system.

In order to perform such a phase manipulation two different techniques are envisioned, using a liquid crystal mask or an acousto-optic birefringent crystal [2-3]. The phase modulation is achieved by varying the optical path of different spectrum components. A liquid crystal mask in the center of two gratings in the focal plane of a 1:1 telescope can introduce controlled phase delays to different spatially dispersed frequencies. The commercial liquid crystal consists of an array of 100 μm vertical cells that introduce a delay that is proportional to a DC voltage applied to its sides. The space between the cells is 3μm and the number of the pixels is 128 or 512. With computer addressing is possible to produce a large set of waveforms. Recently some results on pulse shaping using a 128-pixel liquid crystal mask have been reported[4].

Fourier-domain pulse shaping is a robust and well-know technique for the generation of complex waveforms for single femtosecond laser pulse. The method is based upon the application of phase or/and amplitude filtering to the pulse spectrum in the Fourier plane of a 4-f grating-lens apparatus, as shown in Fig. 4.11. The phase-only filtering is energetically more efficient (*i.e.*, results in minimal power loss), and it is easier to implement. However if the spectral amplitude is fixed, designing an appropriate spectral phase mask typically requires computer-assisted optimization through the use of iterative genetic algorithm (GA). This optimization procedure generates a random phase change at each iteration and the change is accepted if it produces a better approximation of the target pulse and rejected otherwise. With the GA we are able to obtain the rectangular pulse with a rise time less than 1ps and a good flat top also in 3rd harmonic, as shown in Fig. 4.12 and Fig. 4.13.

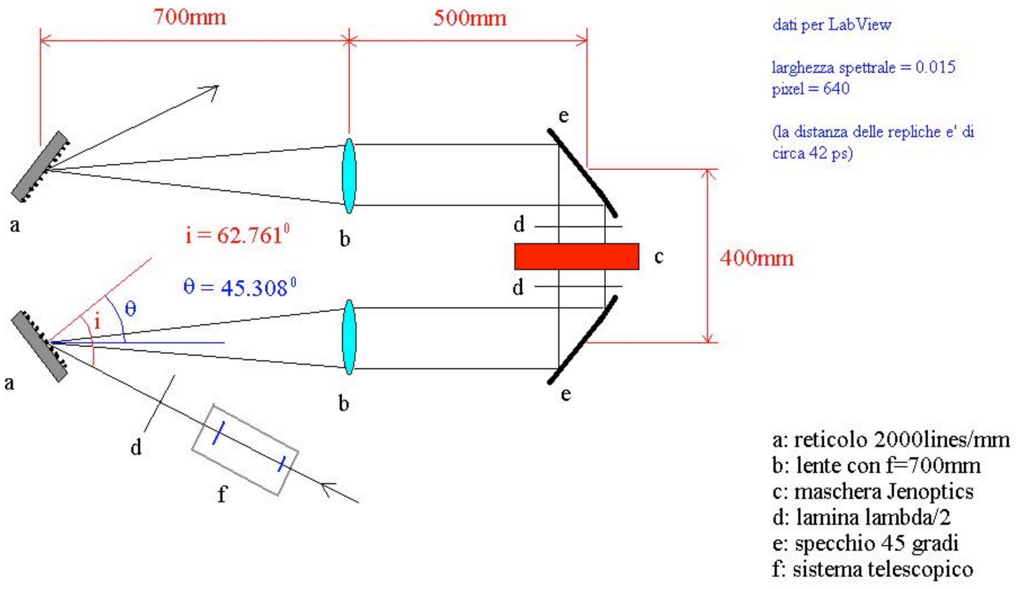

Figure 4.11: *Arrangement for the liquid crystal phase mask.*

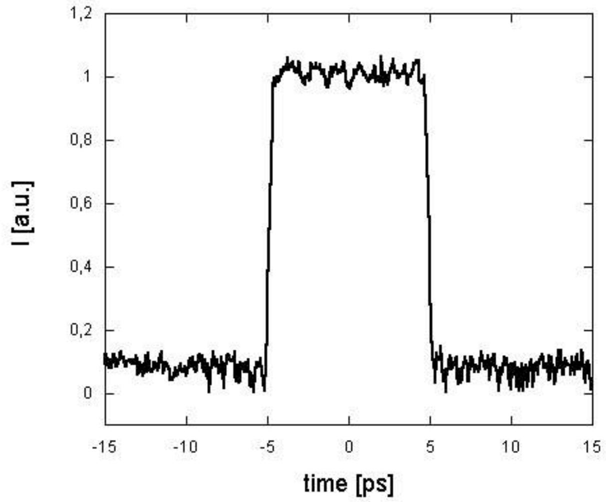

Figure 4.12: *Optimum pulse shape as predicted by a GA algorithm on the fundamental.*

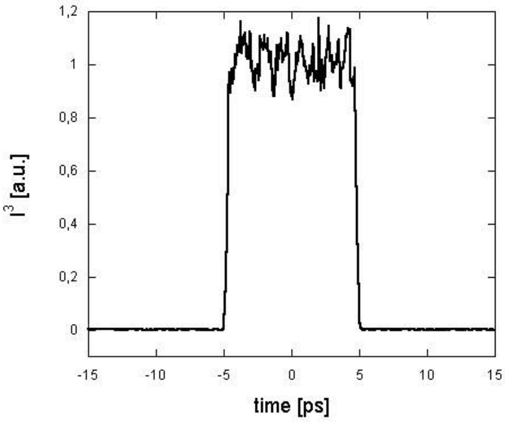

Figure 4.13: *Optimum pulse shape as predicted by a GA algorithm on the third harmonic.*

It is possible to test the GA simulation code, and the feedback system that has to be implemented to control the laser pulse shape on-line, in a mode-locked Nd:Yag laser oscillator in operation at the Milan INFN laboratory, where pulses as short as 80 ps (rms) have been measured, as shown in Fig.4.14. By injecting such pulses, carrying typically 10 nJ of energy and being transform limited, into a non-linear optical fiber one can achieve a spectral band-width up to a few nm, which is enough to compress down to a few ps rms pulse lengths. This would allow the study on how to implement the GA code into a real feedback system in the context of a laser system already in operation.

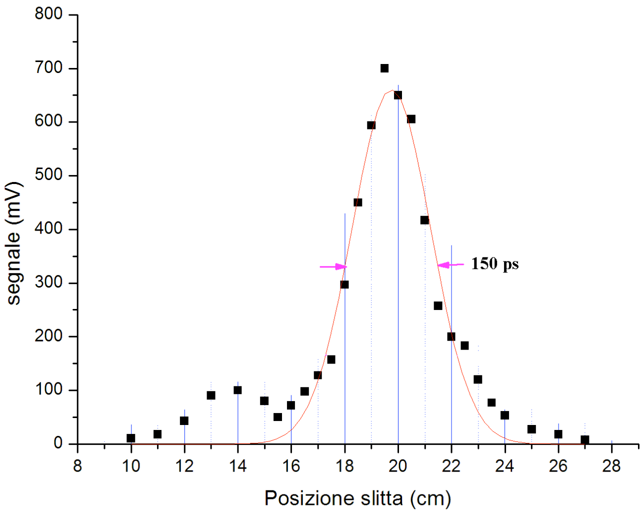

Figure 4.14: *Laser pulse intensity profile of a mode-locked Nd:Yag oscillator.*

As for the acoustic-optic technique, a chirped acoustic wave and the optic pulse linear polarized interact in a TeO_2 crystal. The acoustic-optic interaction occurs for different optical wavelengths, at different depths, where the phase matching condition is satisfied. The matching rotates the ordinary axis linear polarization toward the extraordinary axis polarization. The refraction index along the extraordinary axis is different from that along the ordinary one and thus a frequency dependent phase delay is obtained. A radio frequency generator (with spectrum between 40 and 55 MHz) drives a piezo-transducer to produce the acoustic wave in the crystal. The acoustic-optic pulse shaper has capability of phase modulation on a bandwidth up to 200 nm.

In Fig. 4.15 and in Fig. 4.16 we display the simulations of the pulse profile at the exit of the third harmonic generator using a 2.5 cm long acoustic-optic shaper. The simulations were performed starting from a transform-limited pulse at 780 nm 10 fs pulse from the oscillator[5]. As shown in the figures the rise time and the ripple are inversely proportional quantities. This behavior is due to the finite bandwidth of the input signal. The truncation of the square pulse spectrum introduces ripples and overshoots; this is the well-known Gibb’s phenomenon[6]. Besides, it is well known that the spectrum of a real pulse, with smoothed and long rise time, has a faster decay at high frequencies than the perfect square signal. The finite bandwidth of the optical pulse from the oscillator gives rise to more dramatic distortions if the synthesized pulse approaches the square shape. In general, however, the shape satisfies the required characteristics of rise-fall time and ripple. By varying the compressor length one can easily change the pulse’s duration.

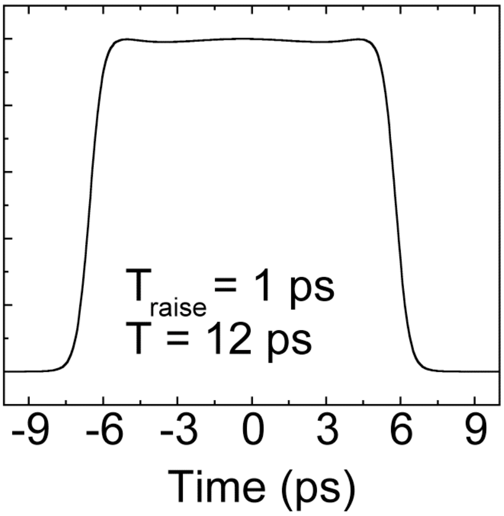

Figure 4.15: *Time profile simulation after the third harmonic generator, with acoustic-optic pulse shaper.*

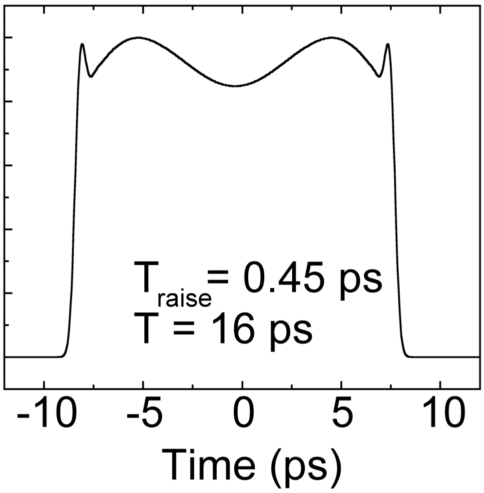

Figure 4.14. *Time profile simulation after the third harmonic generator with acoustic-optic pulse shaper.*

A comparison between the two techniques shows that the acousto-optic solution performs a continuous frequency modulation, and is able to allocate a bandwidth one order of magnitude larger than the capability of liquid crystal technique. The alignment of acousto-optic crystal is less critical than liquid crystal mask. Both the types of shaper can be driven dynamically by measuring the pulse profile after the amplifier to pre-compensate gain and conversion distortions.

Recently, in collaboration with the Milano Politecnico ultrafast laser laboratory, we have conducted a series of tests to demonstrate the pulse shaping with the Dazzler. The preliminary results are of interest to the SPARC laser pulse shaper design.

The Dazzler crystal has been placed near a mirror and the optical laser pulse sent through the crystal for two passes, as seen in Fig. 4.15. This was prompted by the fact that the Dazzler can introduce a stretching only up to 6 ps in a single pass, a limitation caused by the length of the crystal. The obtained temporal intensity was measured by sampling the flat top pulse with the 20 fs reference pulses, delayed varying the optical path length by a translation stage with 100 nm resolution. The very short reference pulse assures a highly precise measurement of the shaped pulse. The shaped and unshaped pulses overlapped in a BBO non-linear crystal, producing a frequency-doubled pulse proportional to the shaped pulse intensity. To improve the signal to noise ratio we used a light chopper at 472 Hz and a lock-in amplifier.

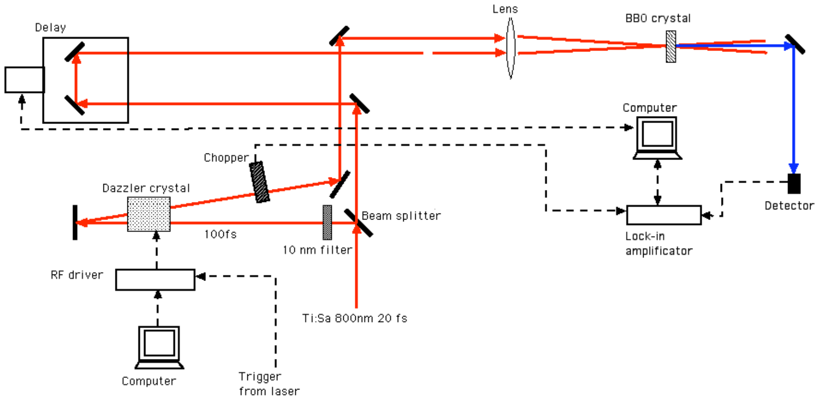

Figure 4.15: *Experimental setup used for pulse shaping with the acousto-optic crystal.*

An interferometric filter was used to reduce the bandwidth of the incoming pulse. In fact it turned out that the optimal input pulse for the acoustic-optics crystal should have 10 nm bandwidth. For larger bandwidth optical pulses the Dazzler crystal shows a reduction of the spectral resolution. In Figure 4.16 the measured cross-correlation profile of the unshaped pulses with the reference optical signal is shown. On the right side the input spectrum of the pulse is displayed. The pulse has clearly a Gaussian distribution with duration FWHM of 100 fs and the spectrum that is not a perfectly symmetric. With this pulse, we havce reproduced the pulse length of the SPARC laser.

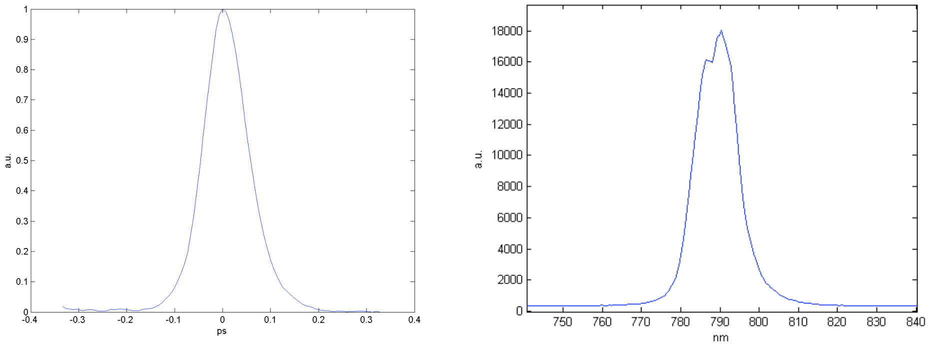

Figure 4.16: *Measured profile (left) and spectrum (right) of the pulse before entry into the Dazzler.*

For the pulse shaping we developed a software to calculate in real time the optimal amplitude and phase modulation, starting from the real spectrum of the pulse after the interferometric filter. This tool generated an input for the Dazzler software control. According with the simulations, the optimum pulse shape can be obtained with a super Gaussian amplitude mask and a S-like group delay of the pulse spectrum. The amplitude filtering removed only the tails of the energy spectrum. The measurements indicated that the acoustic optic crystal could produce pulse with duration up to 12 ps. Figure 4.17 reports the measurement of shaped intensity profile that approach the required pulse for SPARC photoinjector.

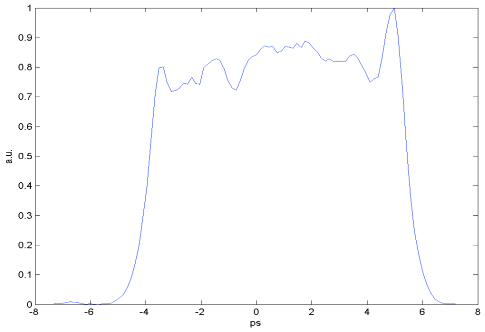

Figure 4.17: *Cross-correlation between the 10 ps shaped pulse and the reference 20 fs pulse.*

As shown in the plot, the pulse rise and fall time is less than 0.7 ps and the ripple peak to peak is around 25% and the pulse's duration is thereabouts 10 ps FWHM. The overshoot on the right edge is not completely optimized. We believe that this not-symmetric profile came out from a not perfect optimization of the dazzler spectral mask with the real characteristics of the input spectrum. A smaller ripple can be obtained by developing more precise simulations that include the exact spectral response of the Dazzler. These preliminary results are very promising for producing the flat top temporal profile required in the SPARC photoinjector.

4.3.4 Laser beam transfer line

We foresee the use of a pinhole and a position-dependent attenuation filter to reduce the Gaussian transverse profile usually produced by the commercial laser to a near-uniform profile. The use of micro-lens arrays are in fact not possible because this method reconstructs the uniform beam on a plane perpendicular to the beam axis. In the SPARC RF gun, however, it has been chosen to illuminate the cathode at near grazing incidence.

The photon frequency has to be tripled by two non-linear crystals to obtain photons with energy above the photoemission threshold for copper. The large bandwidth of pulse limits the efficiency of third harmonic conversion. In fact the bandwidth of the non-linear crystal is inversely proportional to its thickness. But the efficiency of the frequency conversion process is proportional to the crystal's thickness. The efficiency of a non-linear process is proportional to the power density of the optical beam. The damage threshold of the crystal is 5 GW/cm^2 and that means the laser spot's diameter has to be larger than 4 mm. Typically, with the maximum power density, the third harmonic conversion is 5% for KDP-BBO crystals, and 10% for two BBO crystals with large bandwidth pulses.

Additionally, the nonlinearity of the harmonic-generation process can enhance all initial energy jitters, as well as ripples in time or transverse spatial distribution. These considerations imply a more stringent set of parameters for laser system at the fundamental frequency. For instance the UV energy requirement corresponds to amplitude jitter of 1.5-2.5% at the fundamental frequency.

A dedicated design of the transfer line from the exit of the laser system to the cathode must be undertaken. Critically, the required performance of the laser on the cathode demands good compensation of the pointing instability. An evacuated beam pipe will be employed for laser transport to the gun for preservation of the spatial and temporal pulse profiles and suppression of steering jitter. Additionally, it has been demonstrated that Fourier relay optics can mitigate the effects of the angular jitter from the laser. We foresee to use a spatial flattener pinhole as the object plane. A lens of focal length f_l will be inserted a distance f_l from the pin-hole. At distance $2f_l$ will be placed a 1:1 telescope to collimate the beam just before the evacuated beam pipe. The compensation is obtained with a telescope and a second lens of focal length f_l at distance f_l before the image plane (the cathode). With ray tracing software the demagnification of the laser's angular jitter performed by the Fourier optics can be evaluated. Assuming the layout given in Fig. 4.18, the pointing jitter on the cathode is less than 30 μm for laser angular jitter at the object plane within 0.2 mrad.

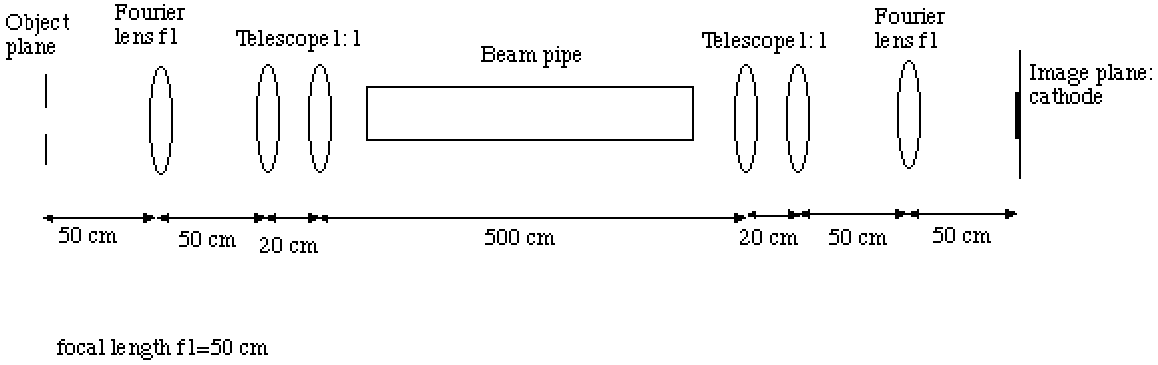

***Figure 4.85**: Optical transport of the Laser beam*

In the BNL/SLAC/UCLA gun the laser beam can impinge on the cathode at either normal and near grazing incidence. Our proposal is to take advantage of grazing incidence because the higher quantum efficiency, and removal of in-vacuum mirrors close to the electron beam, thus avoiding a potential wake-field source. The improvement of □ is due to the Schottky effect induced by p-polarization (the laser electric field is nearly normal to the cathode surface). Besides this effect, a metallic cathode has a lower reflectivity for 72° p-polarization laser beam. However the 72° incidence on cathode induces two unwanted effects: a circular beam at grazing angle becomes an ellipse and the cathode side closer to gun entry will emit 10 ps earlier. Corrections of both of these effects are required to minimize the emittance. With a proper cylindrical lens placed after the Fourier optics, the diameter can be focused in only one direction so that a circular spot can be imaged on the cathode with the ratio between the axes up to 0.98. Perfect circularity cannot be obtained because of the two sides of the beam are at different distances from the cylindrical lens' focus.

For time-skew compensation, a proper reflective blazed grating can be employed. The groove spacing and the blaze angle of the grating have to be chosen to impose the same optical length to the cathode at all the optical rays. Since gratings are lossy in the ultraviolet care must be taken to make the beam size on the grating large enough to avoid damage.

To improve the time and the energy stability of the system it is necessary to control the temperature of the environment. We plan to build a dedicated class 10^4 clean laser room with temperature stabilization to better than ±1 °C.

4.3.5 Diagnostic and feedback control of the laser system

The monitoring of the laser system's performance and active control feedbacks are a prerequisite for optimal laser operation. Here we report the measurements and controls that we intend to perform on the most important laser pulses' characteristics.

a) Time pulse profile

To measure the 10 ps flat top pulse's profile, a streak camera (one may be available from the INFN-LNF Dafne accelerator group on a non-permanent basis) can be used. This diagnostic tool allows the direct measurement of the temporal distribution of the photons from infrared to ultraviolet. Typically, the streak camera has 1 ps of resolution, but recently for expensive streak cameras the resolution has been increased to 0.5 ps. so this technique needs integration with single-shot optical-based diagnostic. Optical cross-correlation and auto-correlation techniques can be used to obtain resolutions down to 100 fs. The correlation signal is obtained by mixing two collinear and delayed replicas in a non-linear material (such as a thin piece of fused silica) to produce a doubled frequency pulse. Starting from the correlation signal, information on the input signal can be obtained with numerical calculations. If the two replicas are produced by splitting the same pulse one obtains the autocorrelation signal. Instead if the pulse is mixed with a short reference pulse the result is the cross-correlation signal. With the autocorrelation technique it is not possible to detect the asymmetry of the pulse and, assuming the input pulse shape, only the duration can be calculated. The cross-correlation allows the signal reconstruction by numerical calculation if the reference beam is short enough.

We plan to use a cross-correlation between the 100 fs pulse from the oscillator and the 10 ps square pulses at the amplifier input. Downstream of the compressor we also plan to perform single-shot FROG autocorrelation[7] (**F**requency **R**esolved **O**ptical **G**ating) on the infrared amplified pulses. The FROG autocorrelation can completely reconstruct the phase and the time distribution of the pulse. In the FROG layout two pulses overlap in the non-linear medium at fixed angle and the autocorrelation detector is followed by a spectrometer. So the result is a two-dimensional pulse representation: the intensity temporal distribution and the spectrum. This technique cannot measure the time profile at wavelengths less than 400 nm because of the lack of appropriate nonlinear materials for output wavelengths less than 200 nm. So for the frequency-tripled pulse diagnostics we propose the streak camera triggered by the RF master clock. The measurement of the temporal profile before the amplifiers, on the other hand, will allow feedback control on the pulse shaper.

b) Energy

To satisfy the energy amplitude requirements on the cathode it is mandatory to control the pulse energy in different points in the laser system and the transfer line. The pulse energy can be measured with pyroelectric joulemeter or calibrated photodiode on a fraction of the laser beam reflected by a beam splitter. Joulemeters and photodiodes will work from infrared to ultraviolet, and show linear response over up to two orders of magnitude. The pulse energy will be monitored at the exit of the oscillator, after the third harmonic generator and on the virtual cathode. To change the pulse energy on the cathode, a proper choice of variable neutral density filter can be adopted.

c) Spatial profile

For the diagnosis of the laser spatial characteristics, CCD cameras at different positions are useful tools. Special care must be given to the measurements of the centroid position of the transverse profile, and spot diameter jitter at the cathode's conjugate plane. Commercial CCDs without the usual UV-protective windows can be used for the UV pulse. A computer with a digital frame grabber can be used to record the video image and calculate the centroid location and the dimensions of the beam. The resolution of the spatial measurements is set by the pixel dimensions. The commercial CCDs have an active area 4 by 10 mm and the pixel dimensions are 8 by 11 μm. A quadrant photodiode in the virtual cathode is useful for fast feedback for spot centroid control. The feedback loop will drive the piezo-actuators of the last mirror.

d) Time Jitter

The laser time jitter is mainly introduced within the oscillator. To measure it a fast PIN photodiode (a sandwich of intrinsic semiconductor between n- and p-doped semiconductors) will be placed just after the oscillator. The fastest photodiode are available with time response down to 7 ps rise time. Using an equivalent-time oscilloscope triggered by the RF system it is possible to increase the resolution to 3 ps. This means that one must use other techniques for less than 1 ps time jitter diagnostic and compensation. The synchronization system is based on a phase locked loop (PLL) to control the oscillator frequency. The 79.333 MHz repetition rate pulses will be detected with an InGaAs diode with a bandwidth of 3.5 Ghz. The 100 fs pulses contain harmonics up to a very high order that allow extract the 2856 MHz with a band-pass filter. The frequency difference with respect to the RF can be measured by mixing with the RF signal. The frequency error will drive the end mirror by a piezo-electric actuator and a picomotor. On the other hand, the phase error between optical pulse and RF oscillator will control the RF phase shifter. With this technique a resolution of hundreds of fs can be obtained. The time jitter that will be introduced by the amplifiers and the transfer line will be measured just before the gun. Because here the pulse repetition rate is 10 Hz a dedicated diagnostic system has to be developed. An indirect measurement of the laser pulse jitter with respect to the RF system is also possible at a BPM or resonant cavity on the beam line after the gun.

References for 4.3

1 A. M. Wiener, D. E. Leaird, J. S. Patel and J. R. Wullert *Opt. Lett.* **15**, 326 (1990).
2 F. Verluise and al, *Opt. Lett.* **25**, 572 (2000).
3 J. Yang and al. J Appl. Phys. **92**, 1608 (2002).
4 S. Stagira and al. Laser pulse shaping for electron photoinjection by an acousto-optic dispersive filter, Proceeding Workshop on Laser Isssues for RF Photoinjector, SLAC 2002.
5 D. A. Davis PhD Thesis, Univ. Rochester, Dept. of Physics and Astronomy, 1999, UR-1573, pp. 23 and 151.
6 A. M. Wiener, D. E. Leaird, J. S. Patel and J. R. Wullert *Opt. Lett.* **15**, 326 (1990).
7 F. Verluise and al, *Opt. Lett.* **25**, 572 (2000).
8 J. Yang and al. J Appl. Phys. **92**, 1608 (2002).
9 S. Stagira and al. Laser pulse shaping for electron photoinjection by an acousto-optic dispersive filter, Proceeding Workshop on Laser Isssues fo RF Photoinjector, SLAC 2002.
10 A. Papoulis, *The Fourier Integral and Its Application*, MacGraw-Hill 1962.
11 D. J. Kane and R. Trebino, Opt. Lett. 18, 823 (1993).

4.4 RADIO FREQUENCY SYSTEM

The SPARC injector will at its early state only a high power RF gun and rf phase-locked injection laser as far as radio-frequency components. Eventually, three very high power linac sections will be added.

Additional relatively high power microwave demands arise from the planned RF deflector ultra-fast beam measurement system. We will present a discussion of the needed modifications to the RF system that are necessary to support the operation of this device in Section 4.6.3.

We review in this section the gradient and power requirements for the gun and accelerating sections, and discuss the solutions which have been chosen to address these requirements. Tracing back from the high power components, and especially their phase requirements, we then discuss the low level rf system and associated feedback systems.

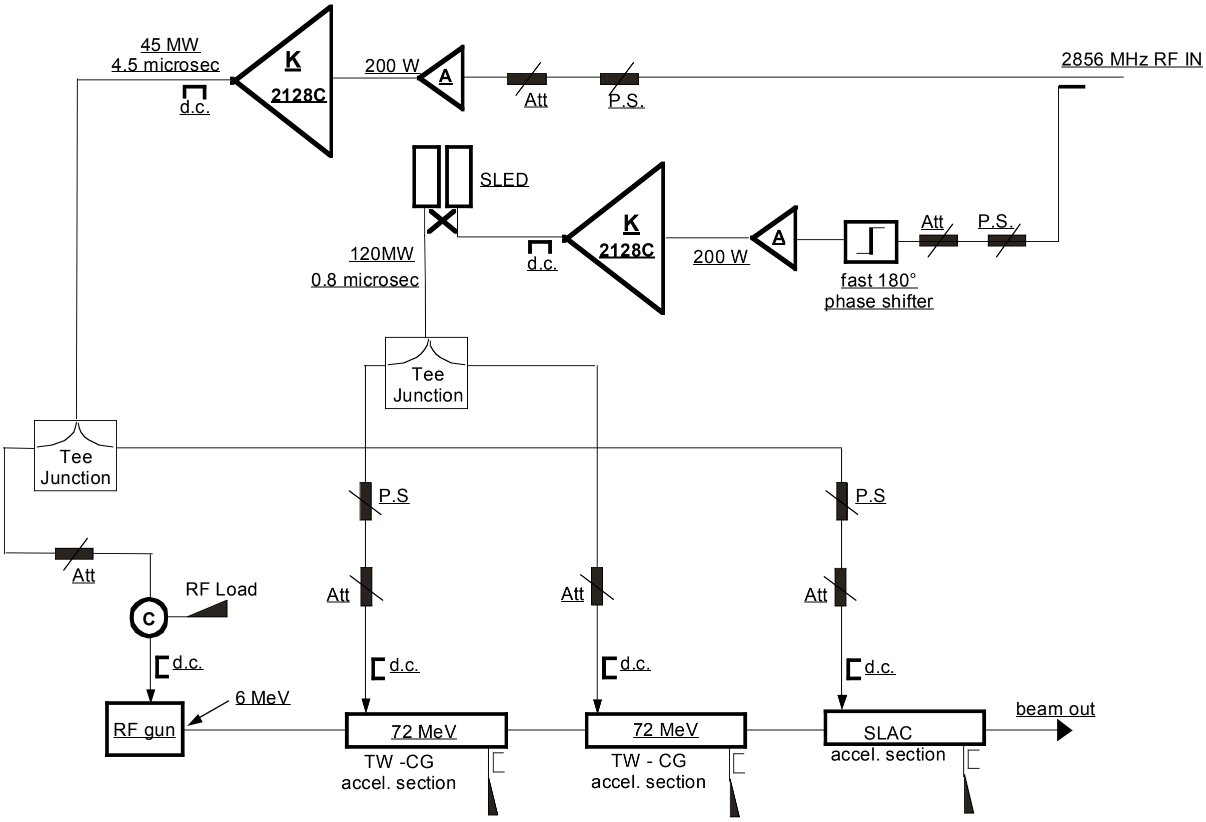

Figure 4.19. *The SPARC-Injector rf system, schematic layout emphasizing needed high power components.*

4.4.1 High Power System Requirements

The rf photocathode gun, which will demand up to 15 MW (11 MW nominal) of power to produce a beam at 6 MeV or above, has been discussed in a previous section. After the rf gun, post-acceleration is provided by two travelling-wave constant-gradient accelerating guides operating at 2856 MHz and composed by 86 cavity cells coupled in the $2\pi/3$ mode. These accelerating sections are known as the SLAC-type structures. To reach the required nominal energy of 150 MeV and in consideration of the initial RF gun 6 MeV energy, the SLAC-type section must provide at least 72 MeV each. The beam loading is negligible due to the very small average beam current (energy extracted by the beam is 70 mJ per section, stored energy in each section is 50 J). For the SLAC-type sections the following expression holds:

$$E_{(\mathrm{MeV})} \approx 10\sqrt{P}_{\mathrm{in}\ (\mathrm{MW})}, \tag{4.1}$$

where E is the energy gained by the beam when travelling through the section and P is the input RF power. Thus, an input power per section of 52 MW is required to achieve the final output energy of 150 MeV. This request set the important parameter of the electric field gradient in the accelerating sections at 25 MV/m. This is a rather high value for the SLAC-type sections, and as such demands careful manufacturing, excellent internal surface finishing and cleaning treatments, and good vacuum performance. However we have identified several industrial vendor which can develop and guarantee high gradient accelerating units. Figure 4.19 shows the schematic layout of the SPARC injector from the viewpoint of the RF system, with emphasis placed on the high power components.

4.4.2 High Power System Components

The linac will use two Thales TH2128C klystrons as high power RF power sources. These sources can generate RF pulses of 45 MW saturated power for 4.5 μsec at 50 pps, a duty cycle that comfortably exceeds SPARC injector requirements. The LNF Accelerator Division has already had considerable positive experience with these sources in the e^+/e^- DAFNE Linac. The TH2128C, shown in Fig.4.20, is a five cavity, single output source, with single focusing coil.

***Figure 4.20**. The 45 MW peak, 2856 MHz klystron TH2128C, from Thales.*

Klystron pulsing will be achieved by 2 high-power pulsed modulators that convert the AC line voltage in the multi-kV range to be applied to the klystron cathode. An existing power station of a S-band klystron like those needed for SPARC is shown in Fig. 4.21.

The modulators must generate pulses of 100 MW peak and 4.5 μsec flat-top (310 kV-330A) at the rep. rate of 10 pps. It has been decided to order to the industry, two modulators of conventional type (pulse forming network) which appear the best solution in terms of cost and ease of design. The more crucial parameter of the power modulators is the stability of the flat-top voltage which influences the klystron beam transit time and hence the RF phase jitter, in addition to amplitude jitter. The klystron RF phase jitter is specified by the manufacturer as 2° per kV of the modulating voltage. Thus, the required modulator voltage stability is set at 1‰ which, over the 310 kV modulating voltage, means 0.6° of 2856 MHz period, *i.e.* less than two-thirds of a picosecond. This specification can be compared to the expected laser injection timing jitter, and they are nearly identical, with the RF phase jitter being somewhat more optimistic. While they have slightly different impacts on the beam dynamics, the fact that RF jitter can be controlled at this level is a positive statement. Further detailed beam dynamic studies will be made to see if incremental improvement on the power supply voltage control is necessary from this viewpoint. This question impacts mainly Phase II experiments.

Figure 4.21*. The power station of a S-band klystron, including high-voltage supply, pulse-forming network, and thyratron switch.*

The klystron's nominal gain is 54 dB, and thus the input RF power supplied to the tube must be about 200 W. Solid state amplifiers that are available from the industry, will be employed to drive the klystrons. The RF driver parameters must be carefully specified. The output pulse rise time should be kept well below 100 nsec; the RF phase stability must additionally be within 1 psec as well. TWT amplifiers have been also considered as klystron drivers but they are more expensive, and are probably unacceptably less RF phase stable.

An energy compressor system (SLED) will be used to increase the peak power for feeding the accelerating sections. An important specification of the SLED system is the peak power gain, which usually ranges around 7.4 dB with maximum values of 7.8 dB. The power at the SLED output can increase in average of a factor 3, but the pulse length is reduced to 0.8 μsec under this condition. The LNF accelerator division is again familiar with this technology - the existing spare SLED unit of the Frascati Linear Accelerator is shown in Fig. 4.22. A T-junction splits the SLED output power to feed the accelerating guides. The peak power per section of 52 MW should be achievable with this system.

Figure 4.22. *A SLED unit at INFN-LNF.*

The RF gun requires instead a full-length 15 MW RF pulse to achieve the maximum field, thus the klystron output is split, uncompressed, by a tee. One output is forwarded to the gun, which is a standing wave cavity, by means of a RF circulator to protect the klystron from the reverse power. The second tee output is dissipated on a dummy load and may be eventually utilized to feed an additional accelerating guide. This guide will be a standard section (given by SLAC on loan), or in Phase II, a custom slower than speed-of-light structure now under study in Milano. It should also be noted in this regard that spare rf power may be needed at the 1 MW level for use in rf deflection-mode cavities employed in sub-ps resolution beam sweeping diagnostics.

The RF power is distributed by a system of rectangular waveguides (WR284), operating in vacuum (10^{-8} Torr) to increase the dielectric breakdown strength and allow high peak power operation. To reduce RF phase drifts due to ambient temperature variation, the waveguides will be temperature stabilized at 45°C ± 0.1 by means of heated water control. Figures 4.23(a) and 4.23(b) give a likely schematic view of the waveguide system installation.

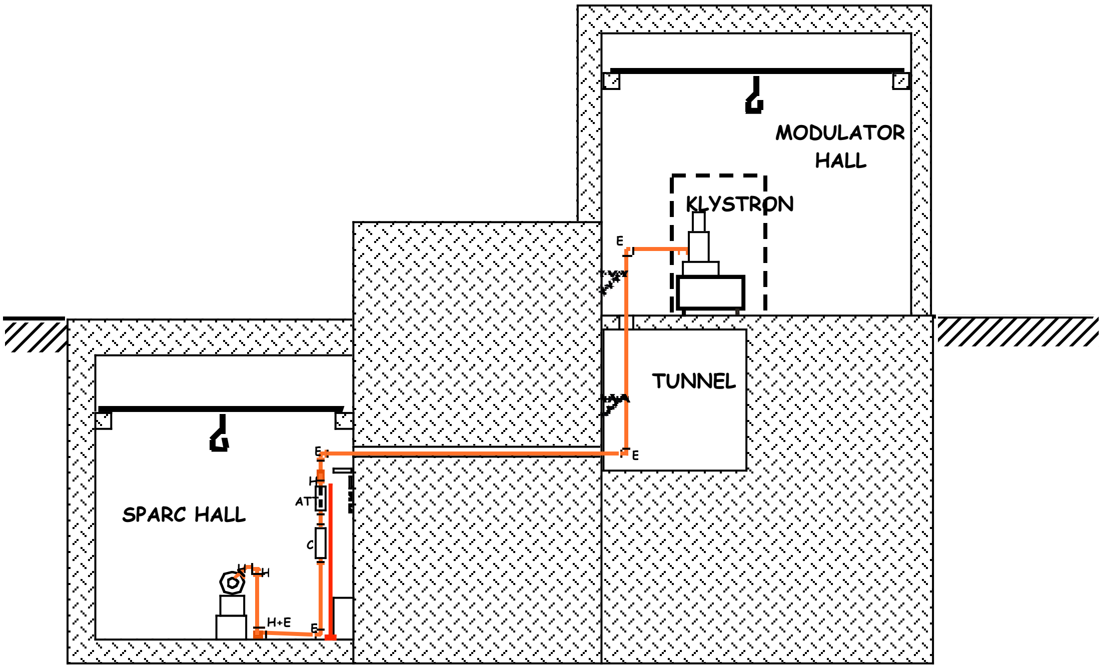

Figure 4.23(a) *Schematic layout of the SPARC-injector installation (side view), with waveguide run shown in red.*

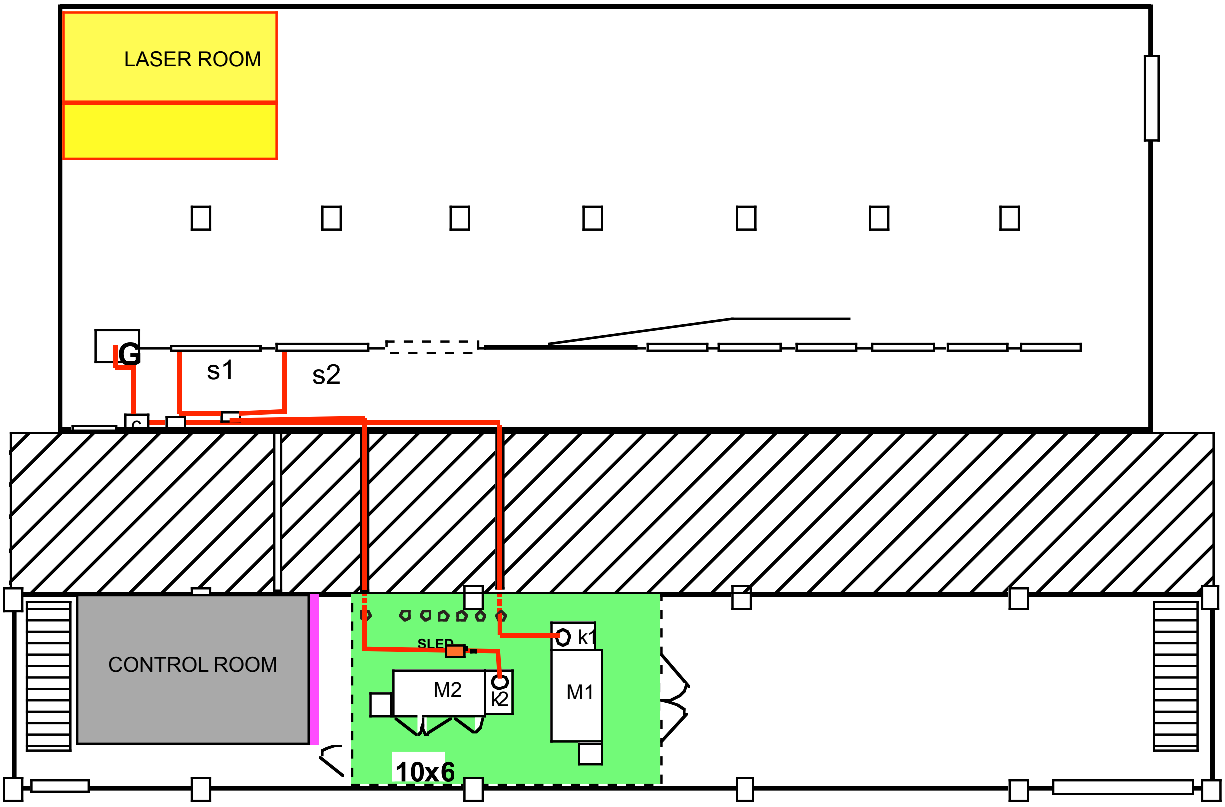

Figure 4.23(b). *Schematic layout of the SPARC-injector installation (plant view),with waveguide run shown in red.*

Continuously variable phase-shifters and attenuators will be used, to allow fully independent phase and amplitude variation of both the gun and the accelerating sections RF field. This option is critical in the optimization of the machine performance in general, and in providing all the capabilities needed for eventual velocity bunching and chicane bunching studies. The phase-shifter and attenuators located in the waveguide arms are high power devices capable of operating in vacuum, and are commercially available.

The total length of the waveguide path from the klystron output to the accelerating section input flange is about 32 meters. The RF loss of a rectangular WR284 copper guide at 2856 MHz in the propagating TE_{10} mode is 0.018 dB/mt. The RF power available at the first accelerating section input flange can reach 56 MW if the insertion loss of power phase-shifters and attenuators is limited to 0.1 dB each.

The RF circulator allows dissipation of the power reflected by the standing wave rf photocathode gun cavity on the 3rd port dummy load without damaging the klystron. RF circulators capable of handling 20 MW peak power at 10 pps are available from industrial vendors. However, due to the fact that these devices employ ferrite materials, they do not usually operate in vacuum but in pressurized atmosphere of *sulfur-hexafluoride* (SF6) to guarantee the required insulation. The waveguide vacuum system will be separated from the circulator SF_6 insulating system by means of RF ceramic windows. These type of windows will also be used to separate the accelerator and wave-guide vacuum systems.

A capillary distributed interlock/alarm system, managed by a complex of programmable logic controllers (PLC), will protect the linac and the RF stations in case of malfunction.

4.4.3 The Low Level RF System

The low-level RF control electronics for the SPARC project is mainly devoted to keeping the RF phases of the accelerating voltages in the RF gun and in the TW sections well locked each other, and to guarantee the synchronization between the whole linac and the laser pulse at the photocathode.

Preliminary beam dynamics simulations show that an overall stability $\Delta f \approx 1°$ S-Band ≈ 1 ps of the laser pulse centroid with respect to the linac RF is adequate for Phase I. The estimated emittance growth is $\Delta\varepsilon/\varepsilon \leq 10\%$ in this case. For Phase II, where RF compression will be experimentally tested, a tighter value is certainly needed ($\Delta f \leq 0.5°$), which may require that, as mentioned above, more attention be paid to high-voltage control in the klystron power supplies.

Feedback systems based on pulse-to-pulse sampling of the RF phases along the linac can be implemented to correct fluctuations in a band that is a fraction of the repetition rate (10 Hz). Thermal drifts can be corrected in this way. In particular, the slow fluctuations of the laser pulse timing respect to the master RF clock can be detected from pulse-to-pulse and compensated by moving the whole RF reference line of the linac to maintain the synchronization. Fast jitter (≥ 10 Hz) of the laser pulse timing cannot be actively cured and therefore it has to be limited by all technical means (see discussion in the previous section on the laser subsystems) to fit the mentioned requirements.

Fast jitter, coming from the harmonics of the 50 Hz line and from other sorts of electronic noise in the RF driver amplifiers and in the high power klystron-modulator complex can also affect the linac RF phases. To fit the stability specifications, measures have to be taken to limit the amount of fast jitter in the linac RF system.

An alternative way of approaching this problem is the implementation of real-time feedback systems capable to steadily lock the RF phase within a fraction of each single RF pulse. Being the pulse duration $t_{RF} \approx 4.5\ \mu s$ the necessary bandwidth of this kind of loops is ≥ 500 kHz that seems to be feasible although challenging. Real-time phase lock system should include the whole RF path up to the klystron outputs. The RF gun cavity may be possibly included depending of the physical length of the waveguide connection to the klystron; including also the TW accelerating sections, that will be fed through a SLED system and whose filling time is $\approx 1\ \mu s$, is probably unrealistic.

A sketch of a possible RF phase control layout is shown in Fig. 4.24. The RF reference line is movable with respect to the RF clock oscillator to follow the slow fluctuations of laser pulse arrival time. Slow changes of the laser pulse path length to the photocatode are also included in this compensation scheme. Real time phase lock feedback systems are proposed up to the RF gun cavity (detected in the full-cell internal rf monitor, where the phase response is a strong function of RF gun temperature) for klystron #1 and up to the klystron output (upstream of the SLED cavities) for klystron #2.

An experimental activity aimed to demonstrate the feasibility of this control scheme has been started. The necessary S-band low-level hardware has been ordered and a phase stability measurement campaign on the linac of the Frascati Φ-factory DAFNE to evaluate the amount and spectral structure of phase noise in a typical S-band accelerating complex is in progress.

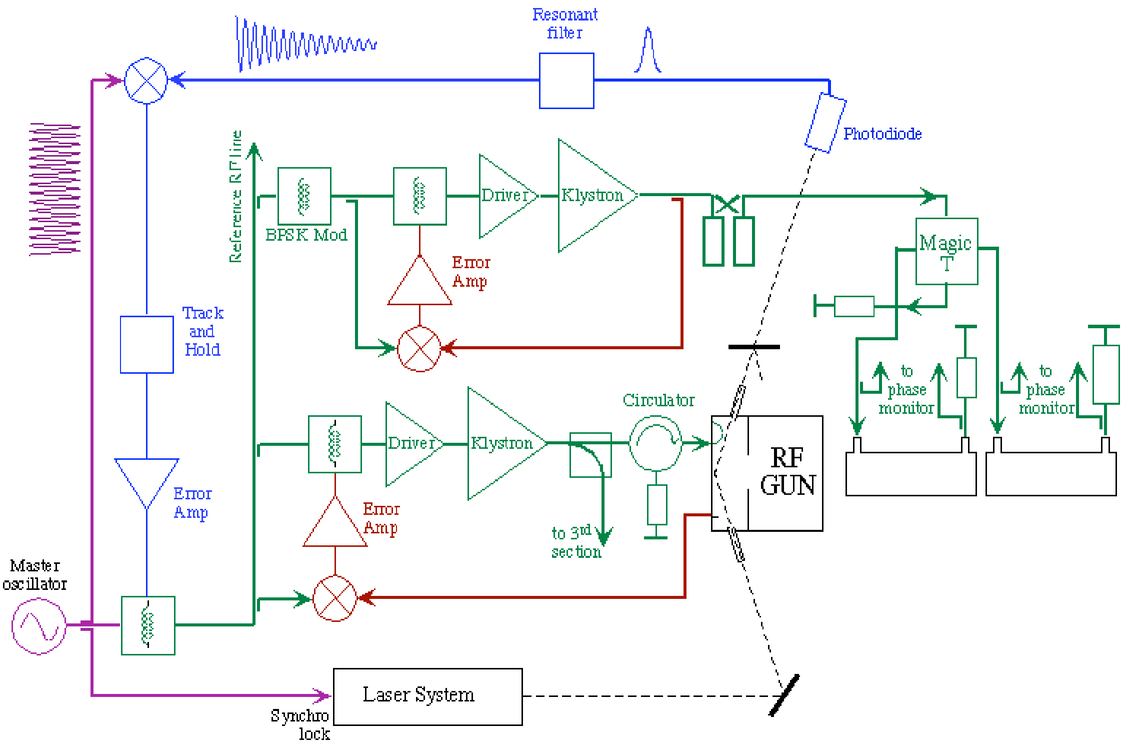

Figure 4.24. *Schematic layout of the SPARC-injector rf feedback system, including correction of the slow component of the laser timing/rf phase jitter.*

4.5 MAGNETIC SYSTEMS

The SPARC magnetic system is composed of the follow list, by type:

- Gun focusing solenoid
- Accelerating section focusing solenoids
- Dipoles
- Quadrupoles
- Steerings

Each type of magnetic element is described in the following sections. .

4.5.1 Gun Focusing Solenoid

This solenoid has been already described in the section concerning the gun. We do not repeat here its description refer the reader to the chapter dedicated to the gun.

4.5.2 Accelerating section focusing solenoids

These solenoids will be placed around the accelerating cavities to create a solenoidal focusing magnetic field to aid in emittance compensation. Only the first cavity will be surrounded by the solenoids in SPARC Phase 1.

The solenoid structure has been studied by means of the POISSON Code. Fig. 4.25 shows the structure under study, where only the last four coils are simulated, in a configuration without any fringing field shielding. It should be noted that in Fig. 4.25 the beam axis is vertical.

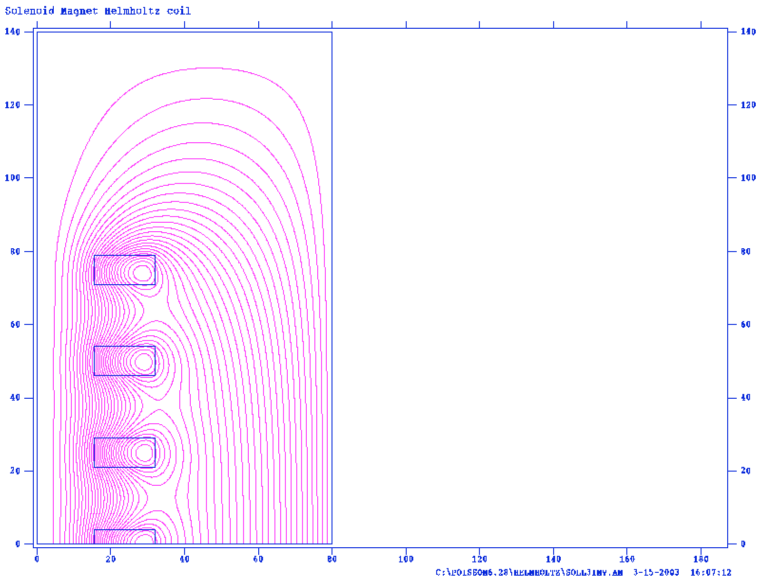

Figure 4.25. *Linac solenoid basic configuration.*

Figure 4.26 shows the magnetic field profile along the beam axis. This configuration has been explored using HOMDYN, and found acceptable from the beam dynamics point-of-view. The main drawback of such a structure is the fringing field that, at a distance of 80 cm, from the beam axis is still if 150 Gauss.

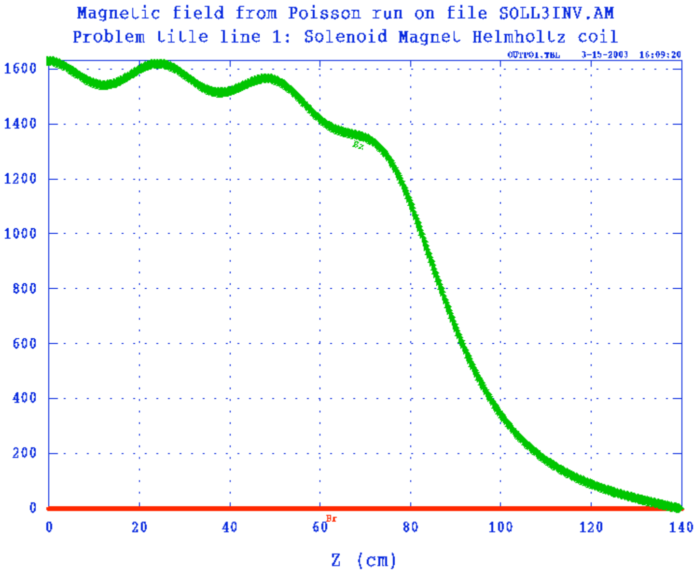

***Figure 4.26**. Magnetic field profile along the beam axis*

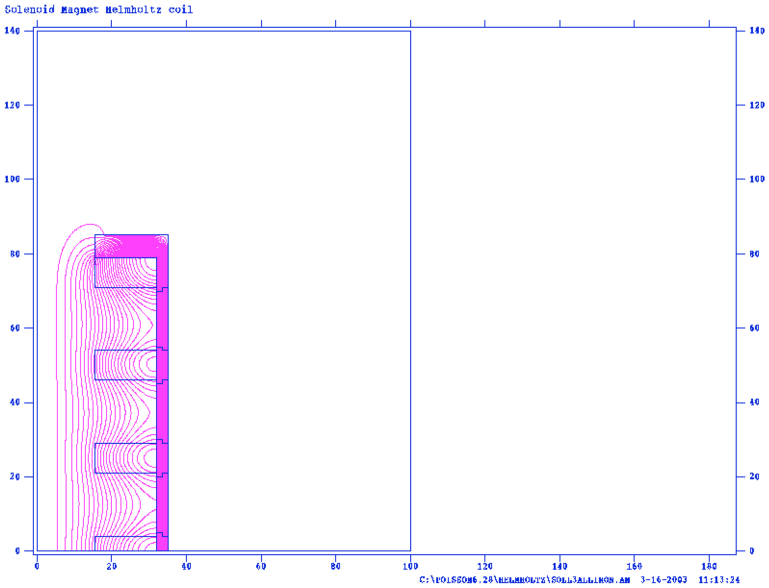

***Figure 4.27.** Solenoid configuration with a continuous iron shielding*

To overcome this problem we propose to put a de-mountable soft iron magnetic shield all around the solenoidal structure, as shown in fig. 4.24. So doing, a new magnetic field profile is obtained and it is shown in fig. 4.25.

The advantages of this configuration are:

- a higher magnetic field, about 1900 Gauss, as opposed to the 1660 G of Fig. 4.23, with the same number of Ampere-turns;
- a sharper magnetic fringe field tail;
- improved transverse alignability of the solenoid, as it will depend partially on machined iron, not simply on wound coils with dielectric coatings;
- no fringing field outside the structure; that means no constraints for materials, external apparata, and personnel safety;
- the iron shielding, realized by means of semi-annular rings, can be easily removed for checks, tests or other necessities;
- thermal confinement of the accelerating structure, that means less sensibility to ambient temperature variations.

The main parameters of each solenoid are summarized in the following table, 4.3. The number of solenoids given relates to Phase I, where only the first accelerating section will be immersed in the solenoidal field.

Table 4.3. *Linac solenoid focusing magnet characteristics.*

Quantity for phase I		12
Inner diameter	mm	308
Outer diameter	mm	632
Coil Cross Section(insulated)	mm^2	162*82
Nom. Cu Conductor Size	mm^2	7.5*7.5
Nom. Cooling Hole Diameter	mm	5
Turns per solenoid		200
Maximum Excitation Current	A	185
Current Density	A/mm^2	5.05
Maximum Voltage	V	30.15
Power per Coil	W	5580
Hydraulic Circuits per Coil		5
Water Velocity	m/s	0.9
Water Flow per magnet (4 coils)	m^3/s	9E-5
Water Temperature Rise	^{o}C	15
Pressure Drop per Circuit	MPa	0.19

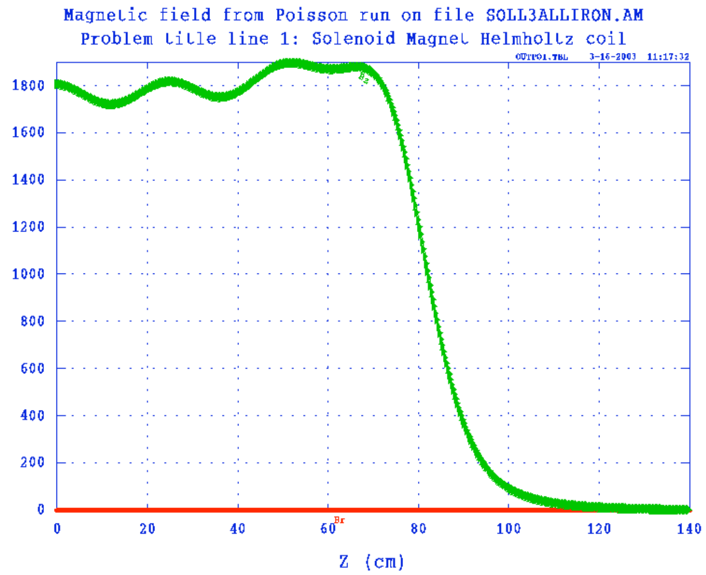

Figure 4.28 *Magnetic field profile along the beam axis in the new configuration*

4.5.3 Dipoles

Dipoles are needed to accomplish the following functions:

- as spectrometer, to drive the beam into the emittance measuring system;
- to drive the beam into the undulator by-pass line;
- to drive the beam into the beam dump;
- to drive the beam into the magnetic compressor in the final SPARC configuration.

It seems to be possible to reuse some existing dipole magnets from the Dafne program. Figure 4.29 shows one of these magnets, which is already available. The gap of the magnet is 50 mm and the maximum achievable magnetic field is 0.5 T, achieved with a current of 103 A. The dipoles will be powered in couple by means of four current stabilized power supplies that can deliver 110 A as maximum current with an output voltage of 60 V.

Figure 4.29 *Dipole magnet (available).*

Figure 4.30 *Quadrupole magnets (available).*

4.5.4 Quadrupoles

Quadrupoles are needed to focus the beam between the linac exit and the undulator entrance, and along the by-pass transfer line. A total of 19 quadrupoles are foreseen. It seems possible to reuse 10 existing quadrupoles which have a bore diameter of 53 mm, and a maximum gradient of 3.4 T/m. The other quadrupoles must be purchased. Figure 4.27 shows some of the existing quadrupoles as they were mounted on an old transfer line. To power the quadrupoles, 19 current stabilized power supplies, 20 A –10V, will be necessary.

4.5.5 Steering Magnets

The number and characteristics of these steering magnets have not yet been defined at this stage of the project. With high brightness beams, having low emittances but high current but potentially large chromatic and wake-field effects, one must steer the beam along the center of the very high field electromagnetic and magnetostatic devices very well. The exact number of steerers and their characteristics will be fixed as soon as the transfer lines between the linac exit and the undulator entrance, and all along the bypass transfer line will be defined, and therefore error studies can be enabled.

4.6 DIAGNOSTICS

The main goal of the SPARC project, the production of an electron beam of very high brightness, requires that a dedicated effort be placed diagnosing the beam, and monitoring of aspects of the system used to create and manipulate the beam. To obtain the highest brightness beam performance, many conceptually new and technically advanced aspects of the injector are to be implemented. It is clear from the experience of high brightness beam and FEL labs worldwide that in order to obtain cutting-edge level of performance that one must be able to "see inside" of the beam, to acquire detailed knowledge of not only nominal beam parameters (centroids and rms widths), but of configuration and phase space distributions as well. Given that the SPARC project, from the beam viewpoint, is essentially a marriage of the two coupled phase-plane manipulations — emittance compensation and bunching — the emphasis on beam diagnostics yielding the most detailed description of the beam is compelling.

The beam diagnostics included in the SPARC project are approached, therefore, with the following guidelines, that impact work in other groups contributing to the project, in mind:

- The need for diagnostics should be consistent with known beam dynamics processes such as emittance compensation and pulse compression (both velocity bunching and chicane-based bunching). Particular care should be taken to have diagnostics which can be used to tune the beam's phase space state; diagnostics should give as detailed information as possible in this regard.
- Because of the relatively low repetition rate single-shot diagnostics are also favored.
- Some beam dynamics-based properties (e.g. emittances) are known to change dramatically during beam manipulations. One must keep in mind that the beam state is described by local, not global quantities for most parameters that are to be measured.
- Simulations can be used to quantify not only the beam dynamics, but the expected performance of the diagnostics, as many proposed measurements depend on precise manipulations of the beam distribution or its sub-components. Particular care should be taken to evaluate collective effects such as space-charge, wake-fields, and coherent radiation in bends when examining the expected performance of the diagnostics.
- The diagnostics considered should be robust, both in the ease of their implementation, and in the interpretation of the resulting data obtained.
- Correction optics and correction algorithms, based on expected measurement capabilities, should be identified and studied using rigorous simulations.
- Many of the measured quantities are ultra-small (spatial information in the micron range) and ultra-fast (relevant time-scales extend below 100 fs). The resolution of proposed diagnostics should be rigorously examined.
- The layout of diagnostic positions,. while driven mainly by beam dynamics measurement and correction considerations, should also be linked tightly to the physical constraints of the beamlines. Possible interferences between the diagnostics, optics, and vacuum systems, as well as between the two beamlines of SPARC, must be investigated.

- Diagnostics need to be evaluated for their generation of halos and/or radiation, which may impact, for example, the undulator magnet in the FEL experiments. The need for collimators should be examined in this regard.

With these guidelines in mind, we discuss the diagnostics presently foreseen for SPARC. Where detailed simulations exist that support the implementation of the diagnostics, they are discussed in the beam dynamics chapter.

4.6.1 The emittance measurement at the exit of the RF gun

At a beam energy of 5-6 MeV, and with a peak current of 100 A, the beam dynamics the approximately 1 mm wide beam has space charge dominated beam dynamics. Therefore quadrupole scanning techniques are not generally applicable in this energy range, and the only proven accurate emittance measurement can be performed is by means of the pepper-pot method for 2D or slit-array in 1D. The schematic of the measurement layout is shown in Fig. 4.31.

To avoid technical difficulties associated with dual alignment of a pepper-pot in 2 dimensions, a double system of emittance slit-arrays, horizontal and vertical, will be used. Their distance from the cathode will be variable over 1.5 m range, covering the more interesting features as shown by the simulations. In particular the double emittance minimum should be clearly measurable, as well as the intermediate maximum. A fluorescent screen, positioned at a variable distance from the slit system, will follow the slit movement. Multi-slit apertures, for single shot measurements, and single slits for accurate emittance and phase space evaluations will be used, mounted on the same actuator. The use of the single-slit technique is obviously predicated on stable beam conditions, in particular the reproducibility of the charge and the steering of the beam centroid.

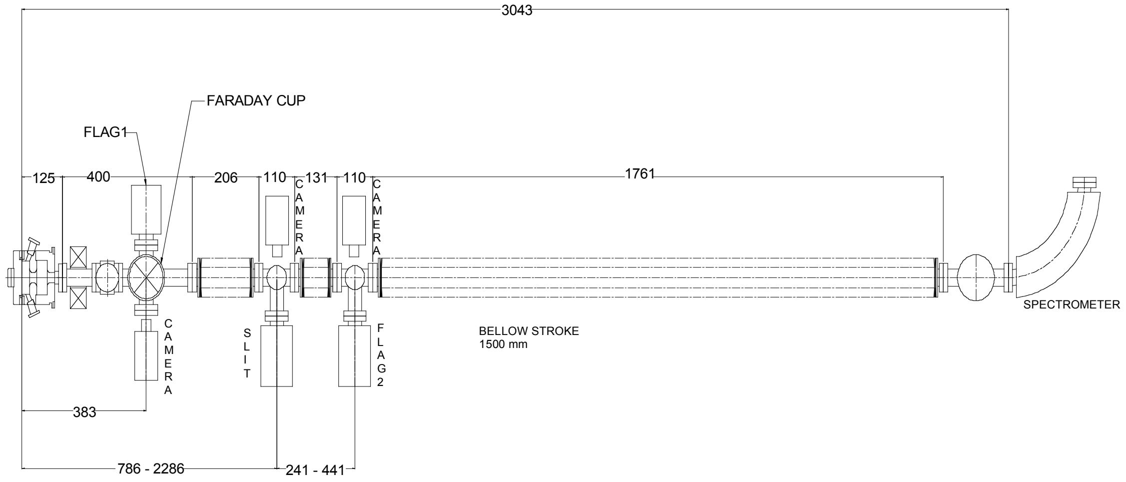

Figure 4.31: Movable system for emittance measurement.

The design of the slit-array is constrained, as discussed in Chapter 3, by the need to create emittance-dominated beamlets. The slits must also stop, or largely degrade, the intercepted components of the beam, and so a certain thickness —a few mm — of high-Z material (*e.g.* tungsten), must be used. This in turn sets the limit on angular acceptance of the device, which implies a limit on how far from the beam waist one may obtain an accurate measurement. The emittance measurement simulation model will be improved to study this problem. In the end, one must measure the unintercepted beam size at the slits, and the size deduced from the slit-array output, to verify the applicability of the technique in any given measurement scenario.

In the case of the slit-collimated electrons, the signal provided by optical transition radiation (OTR) at this energy is not large enough to make the phase space measurement. Therefore it is preferable to use highly sensitive Ce:YAG crystals. Such detectors are commonly used at UCLA for this purpose; an example of a Ce:YAG crystal mounted with viewing mirror that was obtained from UCLA for resolution tests at the LNF DAFNE injector linac is shown in Fig. 4.32.

Figure 4.32: *UCLA Ce:YAG detector and mirror, mounted on assembly.*

The beam will be spent in a dump after a bending magnet. Before the dump, energy and energy spread will be measured. The beam dynamics of the bend spectrometer system must be studied further, as space-charge effects will degrade the achievable resolution of this low energy measurement.

An insertable Faraday cup, which can be actuated into the beam path just in front of the gun, will allow accurate measure of the emitted charge, in particular for the correct phase setting between the laser and the gun RF. It will also allow calibration of non-intercepting measurements that are needed in order to perform parametric studies of emittance vs. charge. Non-intercepting charge diagnostics that may be employed include the sum-signal of beam-position monitors, or fast toroidal instruments called "integrating current transformers" (ICTs). Both of these methods are in wide use at photoinjector labs worldwide.

The problem of beam pulse length measurement at such low energies is a bit subtle. One may not easily use coherent transition radiation-based diagnostics (discussed below), because of the angular spread of the radiation pattern. Also, streak camera-based measurements are a bit difficult, as one may not use optical transition radiation (OTR), or Cerenkov radiation derived from a gas. On the other hand, one may employ aerogel, a substance which has index of refraction between that of a gas and a solid. For 5.6 MeV, the threshold for Cerenkov light generation is at an index of 1.004. The aerogel presently in use at UCLA has $n=1.008$, and therefore produces light at 5°, which is an optimum choice balancing the efficiency of production and problems in pulse lengthening due to large angles in the photon transport to the streak camera. Use of the existing streak camera at LNF with an aerogel detector therefore seems to be a promising path to take for this measurement.

4.6.2 Diagnostics for the SPARC linac

Once the transverse emittance evolution past the gun (initial emittance compensation) has been studied in detail and a full phase space characterization has been performed. At this point, the correct beam conditions at the position entry in to the accelerating structures will have been established, the linacs will be installed, and the commissioning of the full injector can start. We now review the diagnostics that will be needed for each relevant beam parameter.

a) Laser-RF gun parameters

Apart from the control of the stability of various parameters characterizing the laser pulse, as discussed in the laser section, there are special requirements regarding the interaction of the laser pulse with the RF gun. The impact position on the cathode must be centered on the cathode itself and stable within 50 μm. The control of this parameter will be performed by the creation of a virtual cathode, on which the position, and stability, measurement will be performed by a quadrant photodiode or a CCD matrix, with the error signal operating in feedback action on the last mirror alignment.

The phase of the laser pulse with respect to the RF in the gun must be stable within1 ps, and this control will be executed by means of the signal from a fast photodiode, at the virtual cathode level, operating as a feedback on the gun RF phase. The scheme for this feedback is given in the section on RF systems.

b) Beam alignment and standard controls

Standard BPMs of the strip-line type will be used to measure the beam alignment on the magnetic axis. BPMs will be positioned before, between, and after the accelerating structures, as well as in the transport sections before the undulator. As noted above, one may use the sum-signal from these devices to monitor the charge non-destructively. In addition to use of BPMs, the beam current will be monitored after the gun, after the linac, and before the beam dump by ICT monitors.

Beam position monitors (BPMs) will be installed before, between, and after the accelerating structures in the SPARC injector, as well as in the transport section before the undulator. Matched striplines are used in each BPM for the simultaneous readout of the horizontal and vertical positions. The intensity information can also be derived from the sum of the signals. The strips have angular width of ±30° degrees and a length of 136 mm, with the transverse dimensions chosen to form, with the vacuum pipe, a transmission line with characteristic impedance $Z_0=50\Omega$.

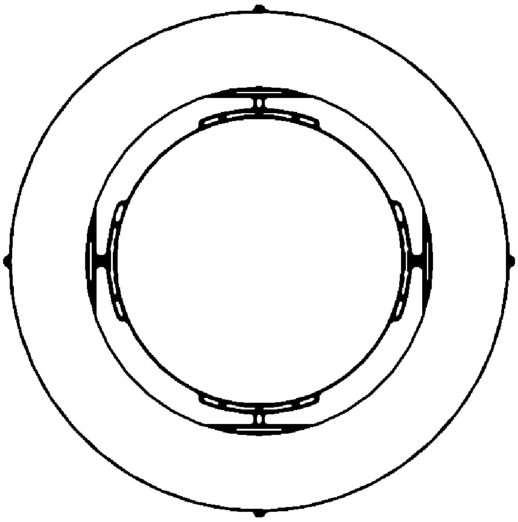

***Figure 4.33**. Cross-sectional view of the stripline beam position monitor.*

The BPM frequency response is periodic with a sinusoidal shape. It presents a null at all frequencies where the strip length is equal to $n\lambda/2$, and the maximum where the strip length corresponds to an odd-quarter wavelength. In our case the length has been chosen to have a maximum of the BPM transfer impedance as near as possible to the linac frequency. In this way we will have enough sensitivity to verify the possible presence of parasitic bunches produced by dark current or other causes.

Each strip-line has two termination ports to avoid reflections in the measuring electronics and to allow the injection of a calibration pulse if needed. When the upstream port is perfectly matched with its characteristic impedance in principle no signal will appear on the downstream port in presence of a relativistic beam.

***Table 4.4:** BPM parameters.*

Vacuum pipe diameter	47.4	Mm
Stripline diameter	39.4	Mm
Stripline angular width	30°	Degree
Stripline length	136	Mm
Characteristic impedance	50	Ω
Strips thickness	1	Mm
Max of transfer impedance	N*551	MHz (*n* odd integer)

The pickup voltage induced by a charged bunch at the upstream port is given by the following expression:

$$V(t) = \frac{\phi}{2\pi}\frac{Z_0}{2}\left[I_b(t) - I_b\left(t - \frac{2l}{c}\right)\right] \qquad (4.2)$$

where □ is the angular coverage of the strips, Z_0 the characteristic impedance of the line, l the length of the strips, and $I_b(t)$ the beam current [1].

The four pickups signals will be sent to the detection electronics through coaxial cables. The impulse response of a coaxial cable, taking into account the skin effect and neglecting dielectric losses, can be estimated as

$$h(t) = \sqrt{\frac{\square}{\square}} \cdot t^{\square\frac{3}{2}} \cdot e^{\square\frac{\square}{t}} \tag{4.3}$$

where □ is function of the cable attenuation A (dB) and the frequency f (Hz) at which A is measured [2].The voltage signals induced by a centered beam, expected at the end of a coaxial cable is given by the convolution of the two responses (Eqs. 4.2 and 4.3) given above. The bunch is a few ps long and for our estimate it can be approximated by an impulse function. In this approximation, we obtain for different cable length the waveforms reported in Fig. 4.30.

The beam position will be deduced comparing the amplitude A,B,C,D of the signals induced in the four striplines. Measurement and acquisition of these signals will be performed through a dedicated detection electronics. The proposed processing scheme for SPARC is commonly referred as log-ratio detection [3]. A possible layout of such a system is shown in Fig. 4.35.

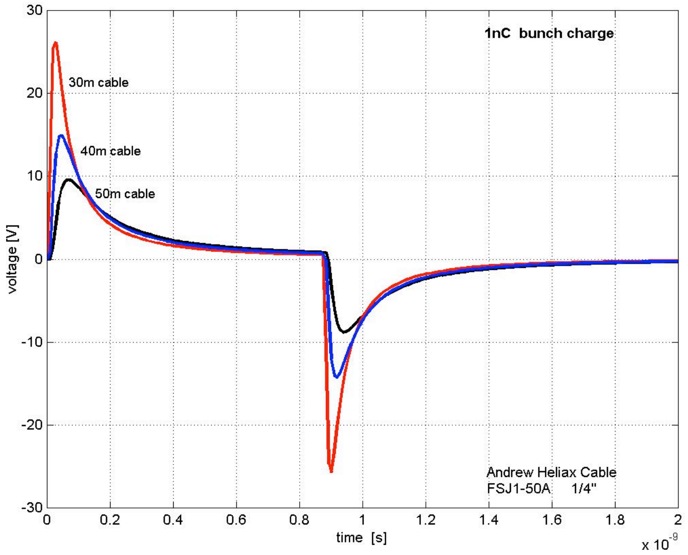

Figure 4.34. *Expected voltage signals induced from a centered beam at the end of different lengths of coaxial cable.*

In the log-ratio method the signals from opposite electrodes are processed through independent channels with band pass filters and logarithmic amplifiers. The RF-bursts from the filters (see Fig. 4.34) are demodulated through amplifiers which provide the log of the envelope of the signals. The outputs are then applied to a differential amplifier to obtain the difference of the logs and hence a signal proportional to ratio of the logs. Externally triggered ADCs are the last stage to acquire the two signals to be processed with a reconstruction algorithm to extract the beam transverse position.

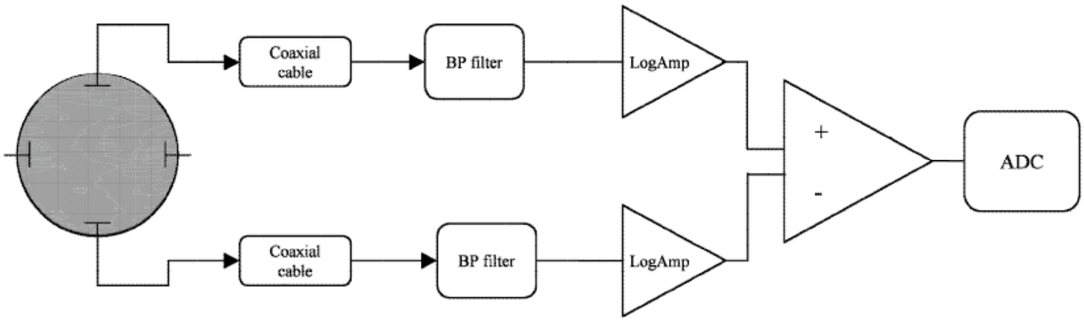

Figure 4.35: *Scheme for a log-ratio detection of the BPM signals (only vertical signal processing is shown).*

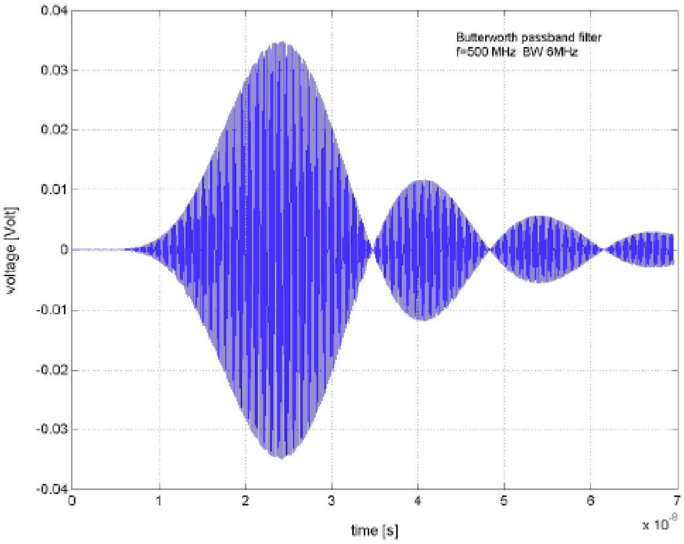

Figure 4.36. *Sample output signal from band-pass filter.*

In fact, as a first order approximation, for small beam offset we can write:

$$x = k_x \cdot \log\left(\frac{A}{D}\right) \tag{4.4}$$

$$y = k_y \cdot \log\left(\frac{B}{C}\right) \tag{4.5}$$

where k_x and k_y [mm] are the inverse sensitivities of the BPM. The proposed pickup has the same sensitivity for both horizontal and vertical axes; it can be estimated as:

$$k_x = k_y \approx \frac{\ln 10}{8} R \cdot \frac{\phi}{\sin(\phi/2)} = 25.1 \text{ mm} \tag{4.6}$$

where the best approximation is obtained if R is the average of the strip radius and the beam pipe radius [1].

Nonlinearities in the BPM performance for larger beam offset, due both to the pickup and the logarithmic transfer function, can be accounted for by using a nonlinear fit. Coefficients of the fitting functions are deduced from bench calibration, performed simulating the beam field with the wire method and measuring the BPM response for different wire position.

The BPM resolution, *i.e.* the minimum position difference that can be measured, is limited by thermal noise, electronic noise and fitting functions error. The thermal noise contribution to resolution errors can be evaluated from the expression for the beam position used with the logarithmic method,

$$\Delta x_{noise} \approx k_x \cdot \log\left(1+\sqrt{2}\cdot\frac{\sigma}{A}\right) = 1.5\ \mu\text{m}, \qquad (4.7)$$

where σ is the noise rms voltage superimposed to the beam induced signals, in our case $\sigma = \sqrt{4kT\cdot R_L \cdot \Delta f} \approx 3.5\ \mu V$ for a R_L=50Ω load impedance, T=300°K temperature and Δf=6 MHz bandwidth. The amplitude A is that of the beam signal, as obtained from the generic stripline at the output of the band pass filter (shown in Fig. 4.32 for nominal bunch charge).

The contribution to resolution error coming from quantization error in the analog to digital conversion for a 12 bit ADC is:

$$\Delta x_{adc} = \frac{1}{\sqrt{2}}\cdot k_x \cdot \frac{1}{2^{12}} \approx 2.2\ \mu\text{m}. \qquad (4.8)$$

It follows that the major contribution to resolution errors is introduced by noise figures of amplifiers and any kind of active electronics in the signal chain. In order for these effects to allow us to to achieve a final resolution of 20 μm *rms* the noise figure should not exceed 17dB.

c) Emittance Measurement

At the full energy of 150 MeV, the transverse emittance will be measured by means of the standard quadrupole scanning method. This is not a single shot measurement, but single-shot slit-based measurements may not be performed above, say, 15 MeV, due to unfavorable scaling of the slit dimensions. For quadrupole scans the beam sizes encountered, as predicted by the simulations, will be in the range of few tens of microns. These sizes and intensities require a state-of-the-art detection and some care in choice of camera optics. Under these conditions, measurements at the VISA experiment showed that one may not confidently rely on YAG screens [4]. We therefore are strongly considering OTR, of which we have considerable experience and a strong understanding at LNF. It should be noted that one may also attempt to measure with a single-shot (or few shots) the emittance of the beam through the information obtained through the OTR far-field angular spectrum.

d) Bunch length

This is typically one of the most difficult measurements, and is of particular importance for a beam devoted to a FEL experiment. The difficulty of the measurement will be increased when the bunch compression will be tested.

For the initial bunch length of roughly 10 ps, a streak camera operating with synchrotron or Cherenkov radiation would be the first choice, being a single shot instrument and almost the only one capable of giving the real longitudinal beam profile. In our case, we would have to bring the radiation outside the hall hosting the linac, to a radiation safe location, and preserving the timing properties. This is a very hard task, that convinced us to follow two different approaches.

A now almost standard way of measuring short beam pulses is by the analysis of the spectrum of some coherent radiation. Coherent transition radiation is now being being the most used. This is not a single shot measurement, and a beam profile can hardly be obtained, but the technique is well established and can be more robust and accurate as one makes the bunch shorter. Coherent transition radiation (CTR)-based measurements have shown sub-ps resolution, as illustrated by the data from UCLA Neptune Laboratory velocity bunching data [6] shown below. These experiments are at the limit of resolution of the Martin-Puplett polarizing interferometer, which is dictated in scale by the spacing of the polarizing wire grid (100 microns in this case). It should also be noted that for very long bunches, the collectible coherent signal is also small, and one may not have a robust signal for bunches much longer than the nominal 2.5-3 ps (rms) pulses which are expected in the uncompressed beam case.

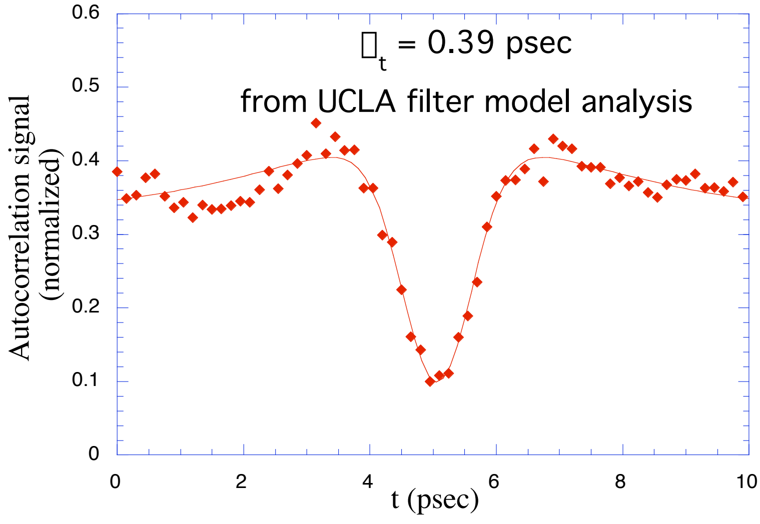

Figure 4.37. *Autocorrelation scan from CTR emitted in UCLA Neptune lab velocity bunching experiment, using short, high-gradient standing wave linac.*

In order to improve upon this resolution, as is needed at ongoing UCLA Neptune, UCLA/LLNL, and UCLA/BNL ATF experiments, a new design for the interferometer has been adopted, as seen in Fig. 4.38. This new design, which is now being seriously considered for use in both chicane and velocity bunching experiments at SPARC, has been developed by UCLA and its collaborator Prof. Uwe Happek of Univ. Georgia. It is a simple, compact Michelson, using partially reflective, <10 micron thick beam splitters. It should have a resolution one order of magnitude smaller than that of the polarizing scheme. In addition, it has a much smaller footprint, and is commensurately less expensive, because of size, fewer optics, and less cost in the beam splitters.

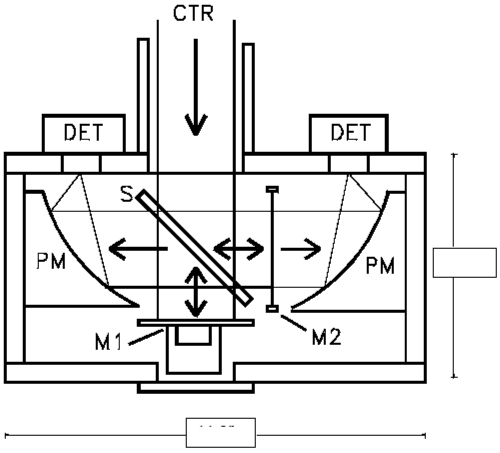

Figure 4.38. *Compact CTR Michelson interferometer for high resolution (sub-10 micron) bunch length measurements (courtesy U. Happek).*

It should be noted that this device, which has a reference detector that measures the total power of coherent radiation can be used for routine beam compression optimization, as the power emitted is roughly inversely proportional to the bunch length.

Another method, which can be considered to be a generalization of the streak camera, is the use of a RF deflector on the beam. A transverse deflecting RF field is applied the bunch, which traverses the cavity at the RF zero-crossing. This introduces a correlation between the longitudinal electron distribution and the transverse angle, which then is converted into a position through a subsequent drift. A high resolution fluorescent or OTR screen, placed in a following low beta position, can produce an image of the bunch longitudinal profile. It is a destructive operation, and some care must be taken for the beam losses, but coupled to highly linear screens (OTR), it can give the better results than those of a streak camera. Preliminary estimations of the needed cavity parameters indicate that 50 micron (160 fs) longitudinal resolution may be obtained with a short (20 cm) standing wave deflector cavity at 2856 MHz that requires only 1 MW to energize. Studies of deflector cavity optimization are now ongoing, and are based on the experience of LNF personnel on developing similar devices for the CLIC Test Facility at CERN.

Both these proposed bunch length measurement techniques will be implemented in the straight line after the linac. It is also worth noting that a very high resolution longitudinal profile measurements may be made with electro-optic sampling of the beam fields, as detected by an ultra-short laser probe. Since a 100 fs laser probe will already be in existence at SPARC, this method, which for now must be classified as an experiment rather than a robust diagnostic, deserves further investigation.

e) Energy and energy spread

These are somewhat standard measurements requiring a dispersive channel. The secondary line in the machine layout is, for this stage, devoted to this measurement. A dedicated optics will provide a high-resolution spectrometer, with an OTR or YAG crsytal screen in its focal plane. The excellent resolution of OTR, which may allow to measurement of smaller details in the bunch energy distribution, needs to be considered against the signall strength available from the scintillating screen. For the high brightness beam being measured at SPARC, we must still evaluate the effects of collective fields (coherent synchrotron radiation) on the accuracy of measurements involving bending of the entire beam.

e) Slice analyses

For a SASE FEL production, the properties of single slices inside the bunch are much more important that the overall properties of the whole bunch. As can be seen by the discussion of the slice-emittance measurement in the simulation section of this document, one may take advantage of the dispersive property of the beam line, in conjunction with information derived from the out-of-bend dimension to make slice measurements. The time-encoding of the information (through the momentum of the slice) in the proposed slice emittance measurement may be obscured by collective longitudinal fields in the beam, such as space-charge and wakes.

Slice analyses based on RF deflectors may also be employed, that do not rely on this somewhat suspect encoding. These schemes have been discussed in detail in the beam dynamics section. We discuss below the details of the RF deflector design that will enable these powerful diagnostic methods to be implemented at SPARC.

References for 4.6.2

[1] R. Shafer: Characteristics of Directional Coupler Beam Position Monitors, IEEE, NS-32, No. 5, 1985, p. 1933

[2] R.L. Wigington, N.S.Nahan: “Transient Analysis of Coaxial CablesConsidering Skin Effect”, Proc. IRE 45, pp.166 (1957)

[3] R.E. Shafer: "Beam Position Monitoring," AIP Conference Proceedings 212, Accelerator Instrumentation, p.47 (1989)

[4] "Limitations on the resolution of YAG:Ce Beam Profile Monitor for High Brightness Electron Beams", A. Murokh, J.Rosenzweig, E. Johnson, X.J. Wang, and V. Yakimenko, in *The Physics of High Brightness Beams,* 564 (Eds. J. Rosenzweig and L. Serafini, World Scientific, 2000

[5] "Bunch length measurement of picosecond electron beam from a photoinjector using coherent transition radiation" A. Murokh, J. Rosenzweig, M. Hogan, H. Suk and G. Travish, *Nuclear Instruments and Methods A* **410,** 549 (1998)

[6] “Velocity Bunching Experiment at the Neptune Laboratory”, P. Musumeci, J. Rosenzweig, and R. Yoder, Proc. PAC 2003 (IEEE, 2003).

4.6.3 RF deflector design

The simplest and most efficient multi-cell deflecting structure that can be used to deflect the bunch is a standing wave structure operating in the π-mode. In Fig. 4.39 we show, as an example, a simple 5-cell cavity with beam pipe tubes. The external radius (*b*) has been chosen in order to tune the resonant frequency of the π-mode to 2.856 GHz, the internal radius (*a*) is equal to the beam pipe radius (20 mm), the cell length (*d*) is equal to $c/2f_{RF}$ to synchronize the bunch passage and the deflecting field. The iris thickness (*t*) has been chosen as a reasonable value of 9.5 mm, considering that it is not a critical dimension in term of sensitivities.

The dispersion curves of the single cell as obtained by MAFIA 2D simulations with b=60 mm are reported in Fig. 4.40. The deflecting π-MODE has a frequency equal to 2.856 GHz, while the nearest monopole and dipole modes are far away from the deflecting mode.

The deflecting voltage $V_\perp$ is related to the dissipated power in the cavity P_{RF} (equal to the input power if the coupling coefficient between the generator and the cavity is equal to 1) and the transverse shunt impedance $R_\perp$ by the relation

$$V_\perp = \sqrt{2P_{RF}R_\perp}\ . \tag{4.9}$$

The total transverse shunt impedance $R_\perp$, quality factor *Q,* and frequency separation with respect to the nearest modes Δf, as a function of the number of cells n, has been calculated by MAFIA 2D. The results of this study are reported in Table 4.4. The transverse shunt impedance scales approximately as $R_\perp \approx 0.5M\Omega * n$ while the quality factor is practically independent of n.

The peak surface electric field E_P in the structure has been found to scale approximately as

$$E_P\left[\frac{MV}{m}\right] \approx 90\sqrt{\frac{P_{RF}\left[MW\right]}{n}}\ . \tag{4.10}$$

Therefore with an input power P_{RF}=2 MW we obtain $E_P \approx$60 MV/m with 5 cells and a marginally unacceptable $E_p \approx$130 MV/m with 1 cell.

The previous results allow us to choose the number of cells for the deflecting structure. The choice can be optimized considering the following considerations:

a) the available transverse deflecting voltage for a given input power;
b) the available space in the SPARC transfer line;
c) the mode separation with different number of cells to avoid problems of mode overlapping;
d) the maximum acceptable surface peak electric field to avoid problems related to high field intensities, discharges and so on.

The 5-cell deflecting structure fulfills all of the stated requirements. In fact, it allows operation with a very low input power, P_{RF}□2MW, while obtaining contemporary low peak surface electric field and resolution length of the order of □25 □m at P_{RF}=2MW. These parameters permit measurement of the longitudinal beam profile with good accuracy, even considering the possibility of longitudinal compression factors of up to 20. Moreover the operation at low input power (□2MW) allows to simplify the power line design as discussed below.

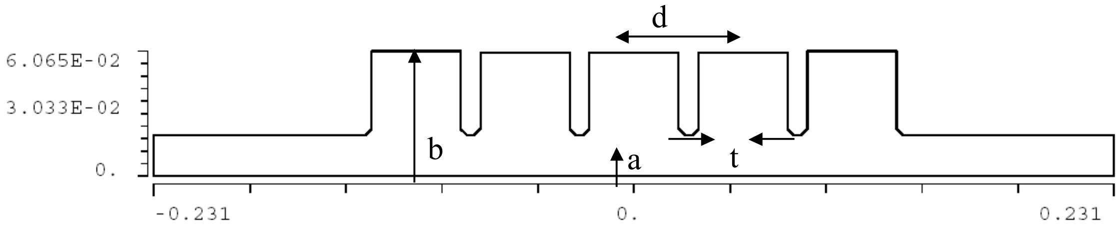

***Figure 4.39**. The transverse profile of the 5-cell deflecting cavity.*

***Table 4.5**: Deflecting cavity properties obtained by MAFIA 2D simulations as a function of the number of cells.*

Number of cells	Total active length [m]	Transverse impedance [M□]	Quality factor	Bandwith [kHz]	Nearest mode frequency separation [MHz]
3	0.16	1.5	17100	167	25
5	0.26	2.5	16700	171	6
9	0.47	4.5	16900	169	1.5

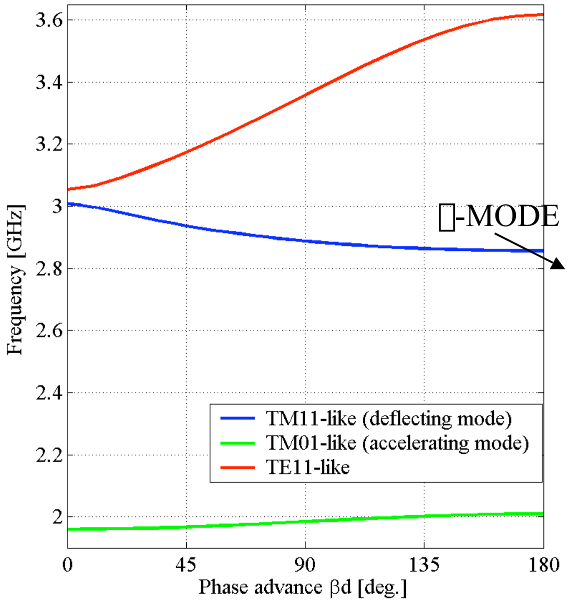

***Figure 4.40:** Single cell dispersion curves of deflection-mode standing wave structures obtained by MAFIA 2D simulations.*

RF deflector design procedure: 2D profile study

The 2D profile of the 5-cell RF deflector has been studied using the MAFIA 2D code. The frequency sensitivities of the single cell profile with respect to the dimensions are reported in Table 4.6. The simulated 5-cell profile is reported in Fig. with the dimensions shown in Table 3. The radius of the cells connected to the beam pipe tube in this design has been changed in order to achieve a field flatness of 3%. The on-axis magnetic field profile in the structure is plotted in Fig. 4.41 and the results of the MAFIA simulations in term of resonant frequency, transverse shunt impedance and quality factor are reported in Table 4. These calculated quantities are also compared with the HFSS results discussed in the next paragraph.

To evaluate the sensitivities of the resonant frequency and field flatness as a function of the single cell dimensions, a battery of simulations have been performed. The results are reported in Table 4.7 and Fig. 4.41 for the most critical parameter *b*. From this study, it is possible to conclude that errors in the cells machining of the order on 10^{-2} mm give frequency errors of the order of 100 kHz and field errors of few percent. These errors can be easily compensated by a proper tuning procedure.

Table 4.7: *Frequency sensitivities of the single cell profile with respect to cell dimensions.*

Dimension	nominal value [mm]	Sensitivity [kHz/mm]
A	20.00	-19
B	60.00	-43
T	9.50	1.2
D	52.48	1.8

Table 4.8: *Dimensions of the 5-cell structure.*

Dimension	value [mm]
a	20.00
B2=b3	59.97
b1	60.67
t	9.50
d	52.48

Table 4.9: *Simulation results of the 5-cells deflecting cavity (comparison between MAFIA 2D and HFSS)*

	MAFIA	HFSS
Frequency [GHz]	2.85699	2.85467
Q	16800	16400
$R_{\perp}$ [MΩ]	2.47	2.43

***Table 4.10**: Resonant frequency sensitivity with respect to the external radius b.*

Dimension	Sensitivity [kHz/μm]
b1	8.6
b2	10.8
b3	

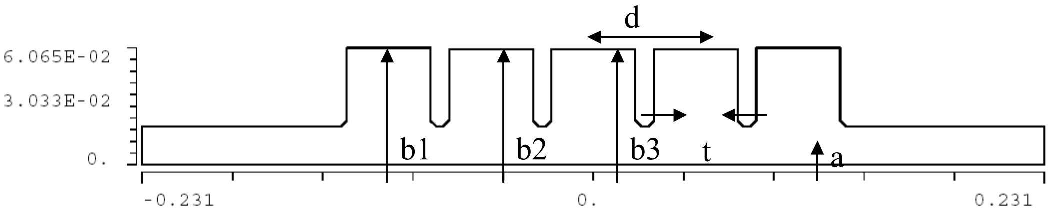

***Figure 4.41**: 5-cell deflecting cavity simulated by MAFIA 2D.*

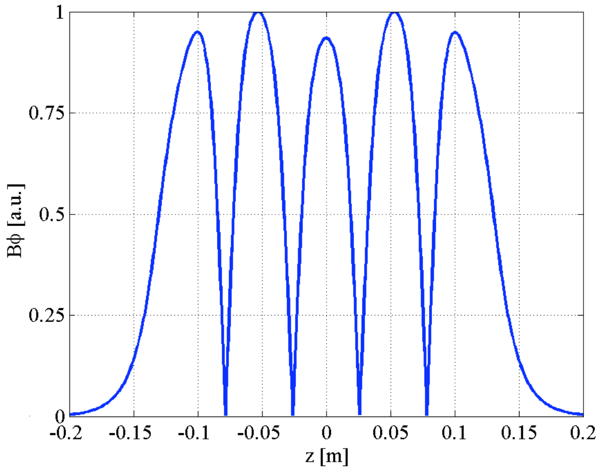

***Figure 4.42:** Absolute value of the magnetic field for the 5-cells cavity obtained by MAFIA 2D simulations.*

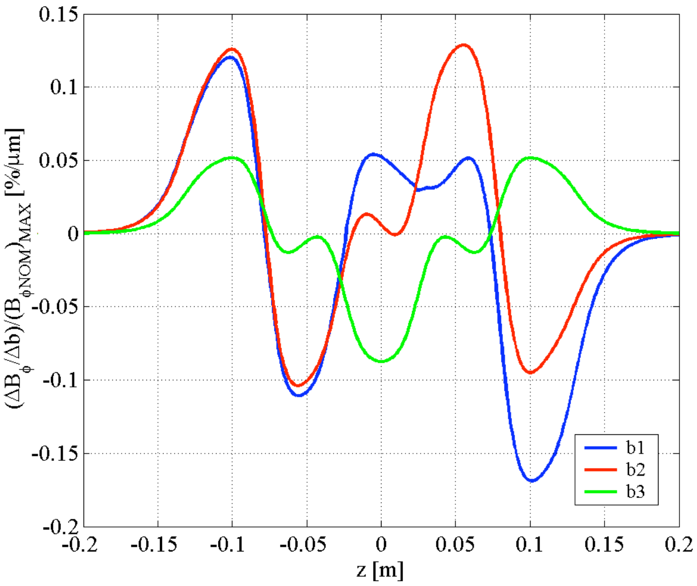

Figure 4.43. *Relative magnetic field sensitivity with respect to external radius of the cells.*

3D profile study

A 3D simulation study of the deflecting mode structure has been performed using HFSS. The comparison between the 2D and 3D results is shown in Table 4.9 where we consider the 5-cell structure without coupler.

The coupler design has been chosen to adapt a rectangular waveguide coupler feeding the central cell of the structure. The HFSS simulated structure is plotted in Fig. 4.44. After some the optimization and re-tuning of the central coupler cell we have obtained the result plotted in Figs. 4.45(a) and (b) in term of field flatness and reflection coefficient at the input port respectively. The obtained coupling factor □ and the transverse shunt impedance are equal to 0.94 and 2.11 M□, respectively.

A complete investigation has been performed in order to find the mode separation between the desired deflecting mode and the nearest mode within the pass-band. The result is summarized in Table 4.10. It is important to remark that the nearest modes are not excited by the coupler and can, therefore, perturb only marginally the deflecting field. The nearest mode that can be excited by the coupler is the □/2 deflecting mode, whose magnetic field profile is shown in Fig. 4.46.

Concerning the tuning system, the simulations performed on the 3D single cell of Fig. 4.43. shows that a cylindrical tuning rod of *r*=5 mm (similar to those found in the RF gun) gives a sensitivity of 550 kHz/mm. This is enough to easily compensate any possible machining error.

Table 4.11: *Frequency separation between the deflecting mode and nearest unwanted modes.*

	Excited by coupler	Δf [MHz]
Deflecting mode tilted polarity (90 deg.)	NO	6.5
$(3/4)\pi$ mode polarity 0 deg.	NO	5.4
$(3/4)\pi$ mode polarity 90 deg.	NO	5
$\pi/2$ mode	YES	20

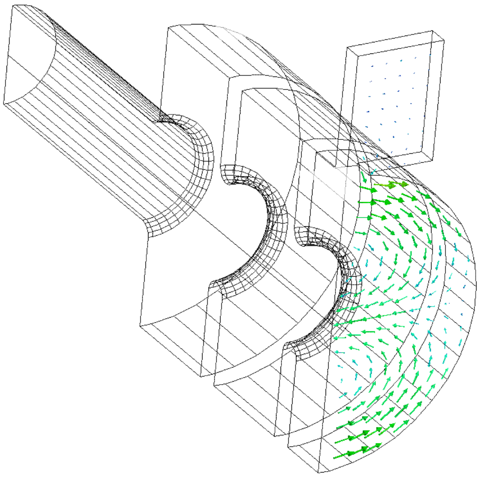

Figure 4.44: *3D HFSS simulated structure with coupler.*

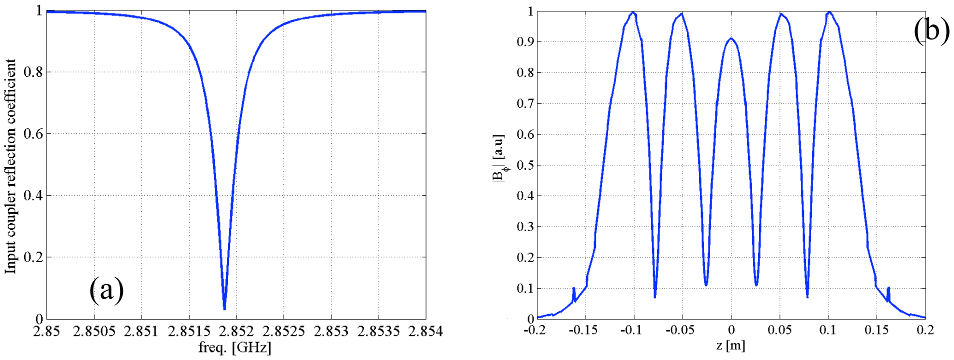

Figure 4.45: *HFSS coupler simulation results: a) reflection coefficient at the input port; b) on-axis magnetic field profile.*

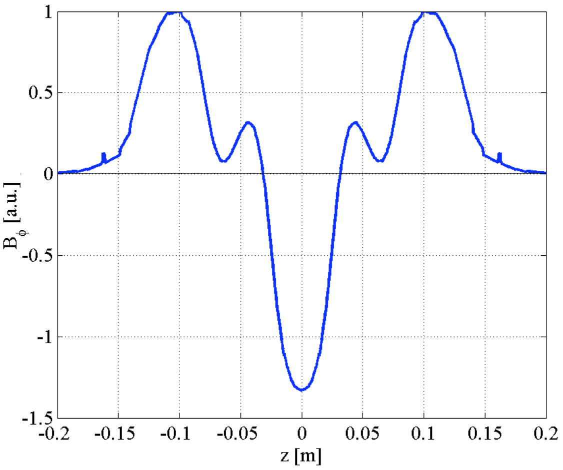

Figure 4.46: *Magnetic field of the π/2 deflecting mode excited by the coupler.*

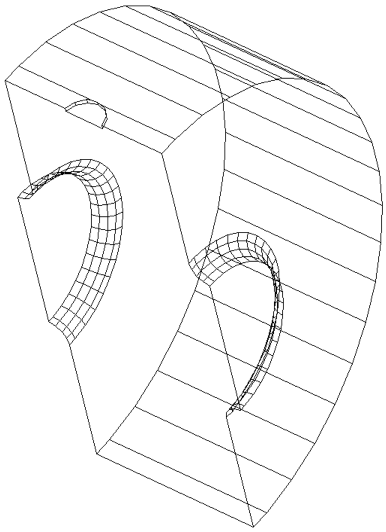

Figure 4.47: *3D single cell with tuning system simulated by HFSS.*

Cold test studies

An aluminum cold test model of the 5-cell π-mode rf deflector has been manufactured to LNF specifications and tested and LNL and University of Rome “La Sapienza” by members of the SPARC team. A photograph of the device during its testing at LNF is shown in Fig. 4.48.

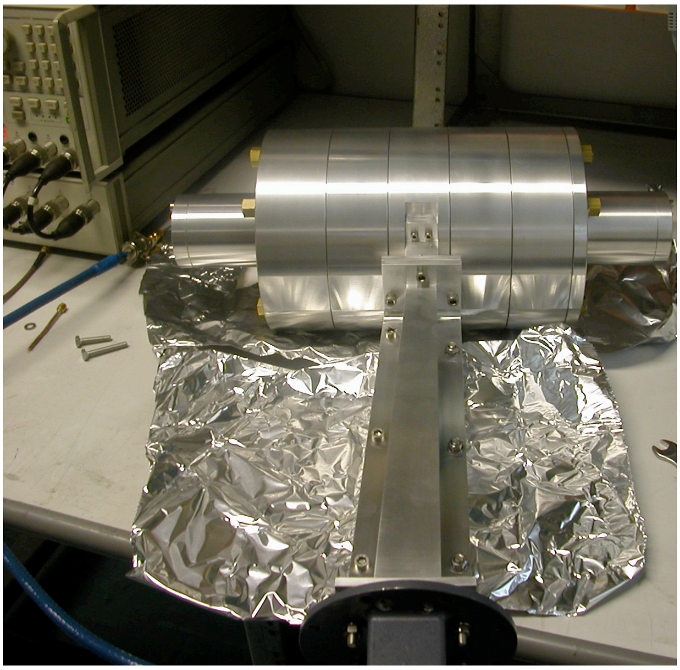

Figure 4.48: *Aluminum cold test model of 5-cell rf deflector, under test at LNF.*

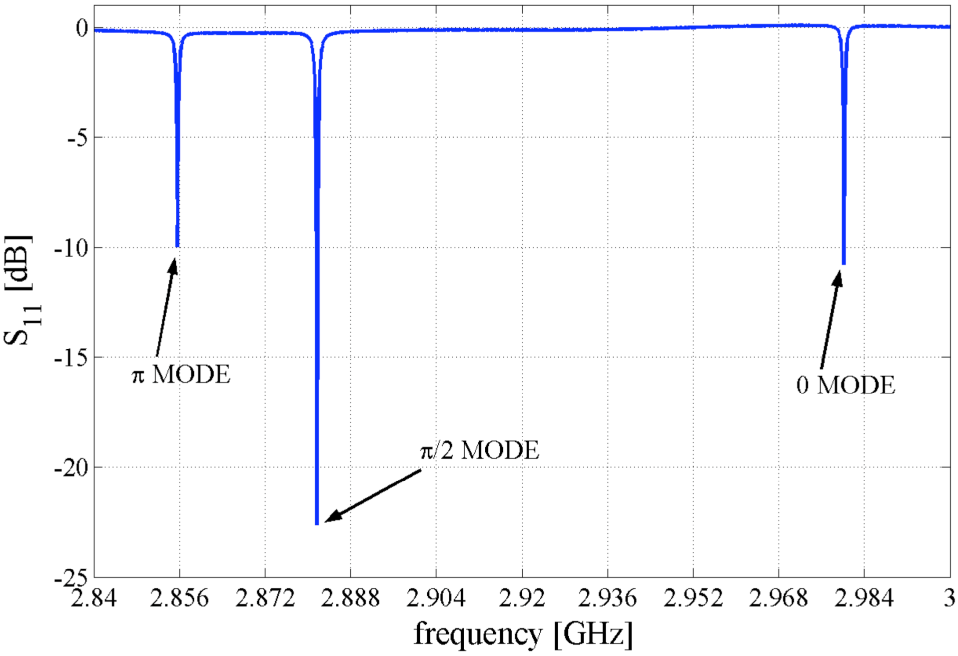

Figure 4.49: *Reflection spectrum of 5-cell rf deflector cold test model, showing little excitation of nearest, odd symmetry modes.*

The rf deflector was tested for mode frequencies and for field flatness of the various modes. The S_{11} frequency spectrum for the device is shown in Fig. 4.49. This spectrum shows that the predicted π-mode frequency is directly at the design value of 2856 MHz. Importantly, it also displays the suppression of excitation of the nearest spurious mode in the pass-band, the 3π/4-mode, by elimination of coupling through choice of the center coupler.

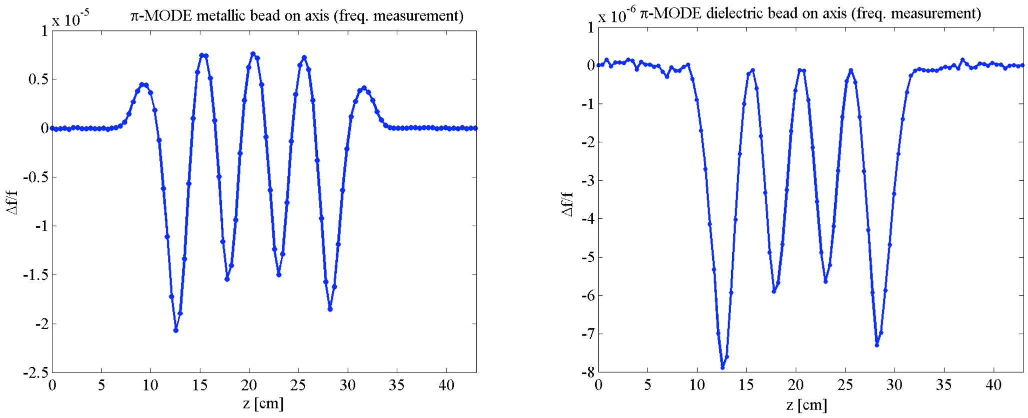

Figure 4.50: *On-axis bead pull frequency shift data for rf deflector π-mode, using both metallic and dielectric beads.*

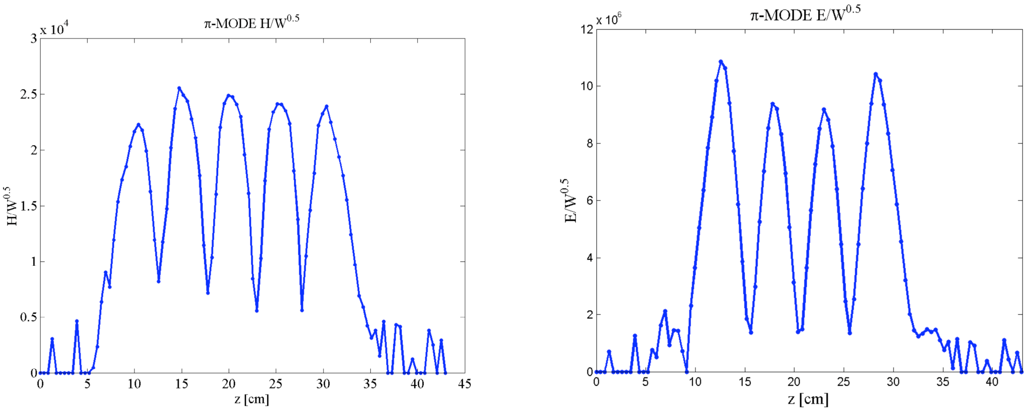

Figure 4.51: *Experimentally determined on-axis π-mode field profiles, from bead pull frequency shift data.*

The results of the bead pull tests on the field profile of the rf deflector π-mode are given in Figs. 4.50 and 4.51. In order to determine the electric and magnetic field profiles on-axis in the device in the presence of each other, it is necessary to perform two types of beam insertions, metallic and dielectric. Analysis of these two spatial scans together allows the disentangling of the two fields, as shown in Fig. 4.51, which illustrates a good level of magnetic field flatness. Thus, we have established the methods for testing that will allow the tuning of the final rf deflector device.

RF deflector power feed system

The 2 MW input power needed to feed the structure can be split out from the first klystron waveguide feed with a 10 dB directional coupler, as illustrated in Fig. 4.52. The circulator and the directional coupler shown assure that every reflected power from the deflector does not interact with the power feeding the RF gun. Moreover the high power switch is included to allow the deflecting field to be completely turned off.

Because of the reduced power needed for the structure it is possible to simply employ a waveguide system with air-fill, thus reducing the costs of the entire power feed system.

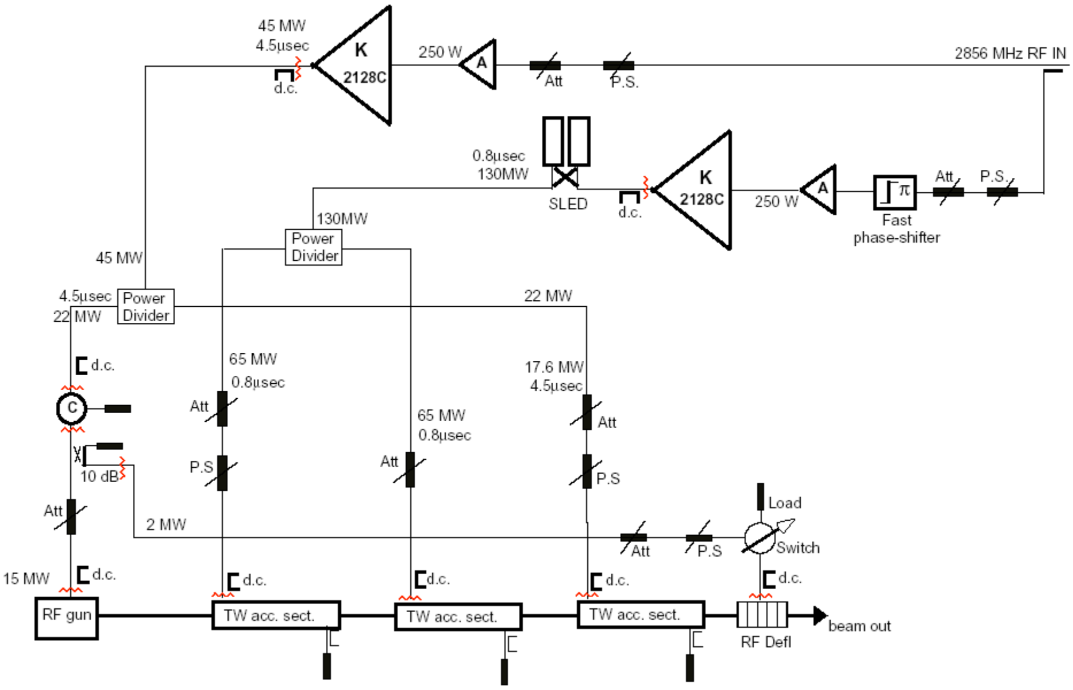

Figure 4.52: *Sketch of the RF deflector power feed system.*

4.7 VACUUM SYSTEM

Beyond the RF gun, the SPARC injector is a linear accelerator that works under ultra-high vacuum ($P \approx 10^{-7}$ Pa). The vacuum system components that are envisioned at present consist of:

a) All metal vacuum chamber
b) 21 Titanium sputter ion pumps
c) 6 Vacuum gauges and control units
d) 2 Residual gas analyzers and control units
e) 6 Gate valves
f) 10 Service valves
g) 1 Fast valve

The implementation of the vacuum system is described in the following subsections.

Vacuum chamber

SPARC vacuum chamber is made of 304L stainless steel, with a diameter of about 40 mm, and CONFLAT type flanges. In order to lower as much as possible the vacuum out-gassing, a rigorous cleaning procedure, using an alkaline detergent in an ultrasonic bath, distilled water rinse and vacuum firing, will be performed.

Pumping system

The SPARC vacuum system, shown schematically in Fig. 4.53, consists of 21 titanium sputter ion pumps:

9 on the RF waveguides
3 on the RF gun
9 on the linac itself.

With these pumps it is possible to reach a vacuum pressure of about 10^{-6} Pa on the waveguides, 10^{-8} Pa on the RF gun and 10^{-7} Pa on the RF sections and the transfer lines.

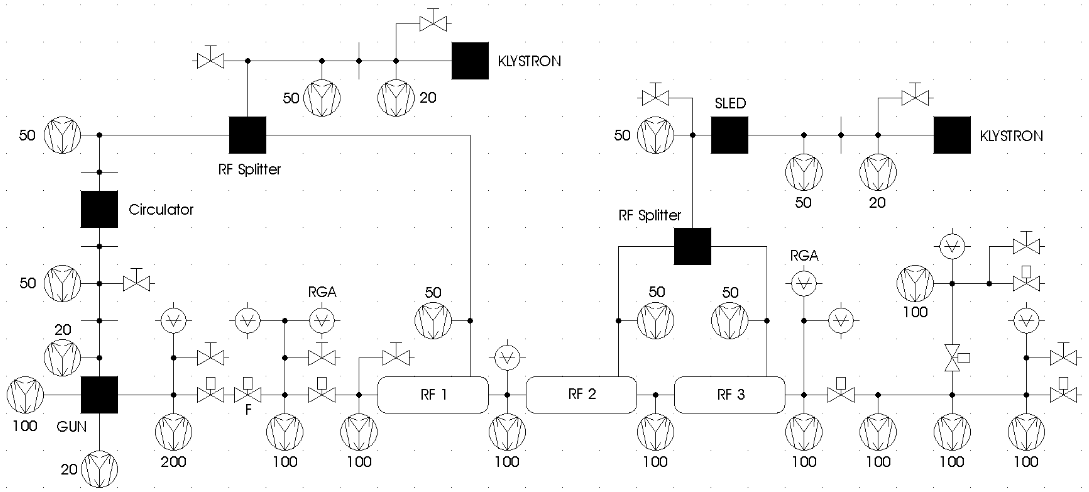

Figure 4.53. SPARC vacuum system schematic.

Vacuum diagnostics

Vacuum diagnostics and control are made using 6 UHV Bayard Alpert gauges and two Residual Gas Analyzers (RGAs) installed on the LINAC. On the wave-guides it is sufficient to read the current input of ion pumps to have a rough indication of the vacuum pressure.

Vacuum valves and ancillary systems.

On the linac there are a total of 6 electro-pneumatic gate valves used to section the vacuum chamber. The first one, installed just downstream the RF gun, in conjunction with a fast closing valve, make up a safety device able to protect the gun from any possible disastrous loss of vacuum integrity.

The remaining valves are located at the beginning and at the end of the accelerating sections, at the end of the linac, and at the beginning and at the end of the spectrometer branch line. An interlock with the vacuum gauges acts in such a way that, when the pressure exceeds a given threshold, all the valves are closed.

Each section of the vacuum chamber has its own service valve to connect a primary vacuum pumping system, made of a turbo pump backed by a membrane pump, used to start the sputter ion pumps.

4.8 CONTROL SYSTEM

Successful commissioning and operation of a modern accelerator strongly depend on a powerful and reliable control system. Experimental accelerators like SPARC add some extra requirements for the control system like flexibility, expandability and compatibility with sub-systems, both hardware and software.

The design of the control system has therefore to be part of the machine project itself and should be, hopefully, developed in parallel with it. The rapidly changing hardware and software must also be taken into account. Industrial standards should be preferred for the core of the control system because of their long lifetime. On the other hand, because of the rapidly changing hardware and software, we must be ready to accommodate components based on new technologies.

The SPARC control system is to be based on distributed CPUs connected each other via shared memory to exchange data and commands. This is a concept we have already developed for LISA and DAFNE control systems and for the integration of optical diagnostic control system in TTF. Shared memory communication can be based either on network connections or using reflective memory.

The control system can be divided in three main parts:

a) Console display;
b) Supervisor and service data logging, web etc..
c) Front-end interface to the accelerator hardware such as RF, magnets, diagnostic instrument etc.

The console system will be expandable and upgradeable, with the possibility to add new operator terminals and increase the computing power if needed. At the supervisor level we will implement some automatic services like continuous data logging of all available machine parameters and distribution of the information to local or remote clients (consoles), or via the web. The front-end CPUs undertake the control of all accelerator components like RF, vacuum, magnets, diagnostic system etc. All these systems may have their own remote interface, either serial, analog or digital I/O with different speeds.

5. Facilities

5.1 DESIGN CRITERIA

The guiding aims of the facilities design are: high level of performance, reliability, energy effectiveness and the easiness of operation and maintenance. Here, the main criteria of design are revisited and some preliminary data are summarized.

The schematic in Fig. 5.1 represents the conceptual design of the cooling water/air conditioning system, without accessory systems. The water circuitry is divided in a de-ionized water part (for magnets and RF components) and a common water part for air conditioning units.

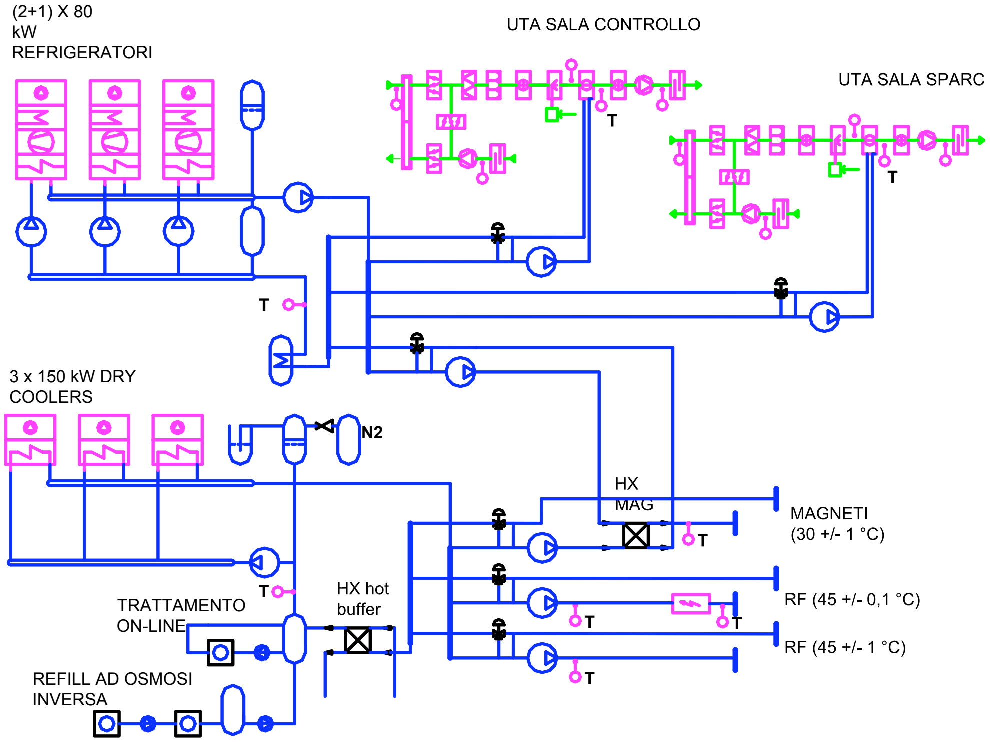

Figure 5.1. *SPARC cooling water/air conditioning system conceptual design.*

Table 5.1. *Water cooling requirements*

USER	POWER		FLOW		deltaT
	Phase 1	Phase 2	Phase 1	Phase 2	□
(DEIONIZED WATER)	kW	KW	liter/s	liter/s	°C
RADIOFREQUENCY	49	49	87.5	87.5	0.134
WATER COOLED MAGNETS	75	296	1.2	4.7	15
SUBTOTAL	125	345			□
(TOWN WATER)	□				□
UTA COILS	91	123	4.3	5.9	5

The fraction of the power released to the cooling water system at high temperature (45°C) by RF accelerator components is dissipated by dry coolers (fan cooled coils). Due to the positive difference between the water and the external environment (max 35°C), this way of cooling is extremely cost effective when compared to other options, as summarized in Table 1.

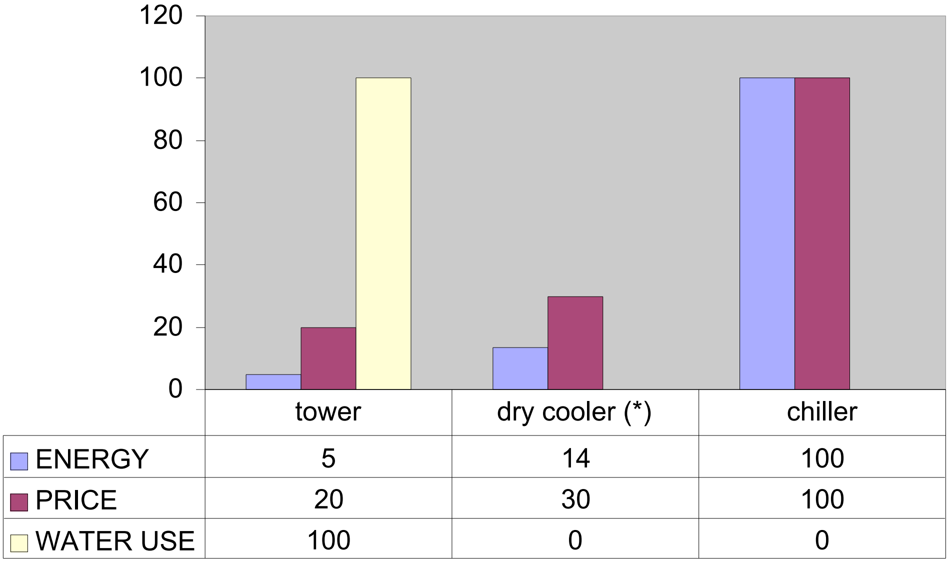

	tower	dry cooler (*)	chiller
ENERGY	5	14	100
PRICE	20	30	100
WATER USE	100	0	0

Figure 5.2. *Comparison of cooling system parameters (%)*

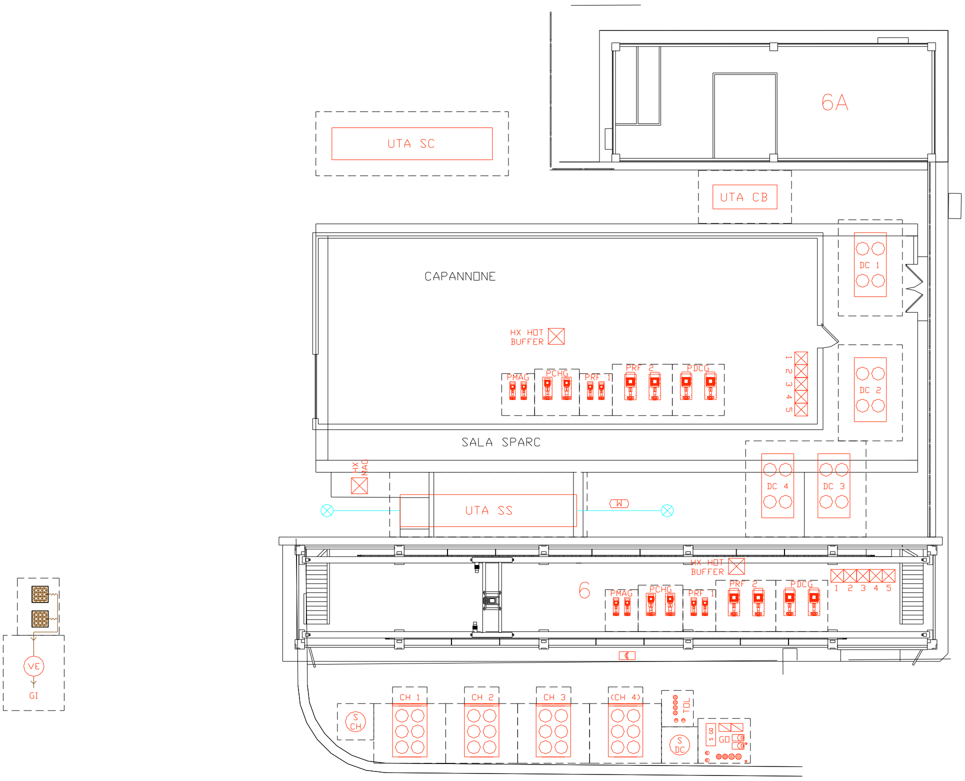

Figure 5.3. *Plant lay-out: main equipment room occupancy.*

Moreover, the use of a closed circuit avoids the circuit to be split in two, primary and secondary, achieving higher efficiency and lower costs. The regulation of temperature is accomplished simply by sequential insertion of the fans (4 - 6 for each dry cooler).

The air conditioning load (Table 2) is sustained by three chillers operating in parallel, producing low temperature water (7°C). Each chiller has a pumping unit, working only when its chiller is on.

The return temperature from users determines the total refrigeration power and so the number of working chillers (from zero to two in FIFO order), but a constant flow to the users is maintained by a general pump (PCHG) and a equalizing branch. The tank in the equalizing branch damps the thermal transitions.

This arrangement allows each chiller to work as near as possible to its maximum load and to have constant water flow in the evaporator, while guaranteeing constant flow to users with a small deviation from the low temperature level of 7°C when their load is lower than usual.

That deviation at low load is easily compensated by proper design of each user's automatic regulation, while the useful overall effect is to reduce power expense and to gain longer chiller lifetime and better COP.

Table 5.2. *Water cooling system summary*

	POWER		**FLOW**		
	phase1	phase2	phase1	phase2	sec/ prim
CHILLERS	kW	kW	liter/s	liter/s	
HX magnets (summer max)	75	296	3.6	14.1	3
UTA coils (summer)	91	123	4.3	5.9	1
TOTAL	**166**	**419**	8.0	20.0	
DRY COOLERS					
RF	49	49	2.4	2.4	0.027
magnets (winter)	75	295	3.6	14.1	3
TOTAL	**125**	**345**	6.0	16.5	

The cooling of magnets at 32°C is obtained by dry coolers in the same way of the RF equipment for a large period of the year, when the ambient air temperature is below 25°C (table 3). In the remaining hotter period, the water temperature is diminished by injecting cooler water from the low temperature circuit in the cold side of HX MAG heat exchanger. The amount of refrigeration power needed to cover these spikes is pumped from a ice storage bank filled during night time with the surplus from air conditioning circuit. In the case the stored power it is not sufficient, the third chiller (reserve unit) will provide the missing capacity.

5.2 Water temperature regulation

Temperature regulation of common chilled water, dry coolers warm water and UTA air supply has been already discussed. The high performance trimming of water supply temperature for RF linac equipment shall be obtained by a scheme with three way valve on the return, a secondary pump and an injection branch, for ±1°C accuracy level; an electric heater near the user will provide the final adjustment for the ±0.1°C accuracy level.

To obtained the required tolerances, DIN (or fractional) class PT100 RTD in four wire configuration with 4-20 mA transmitter and at least 12 bit controller shall be adopted. The valve shall have the proper authority on the circuit and electric actuator with feedback.

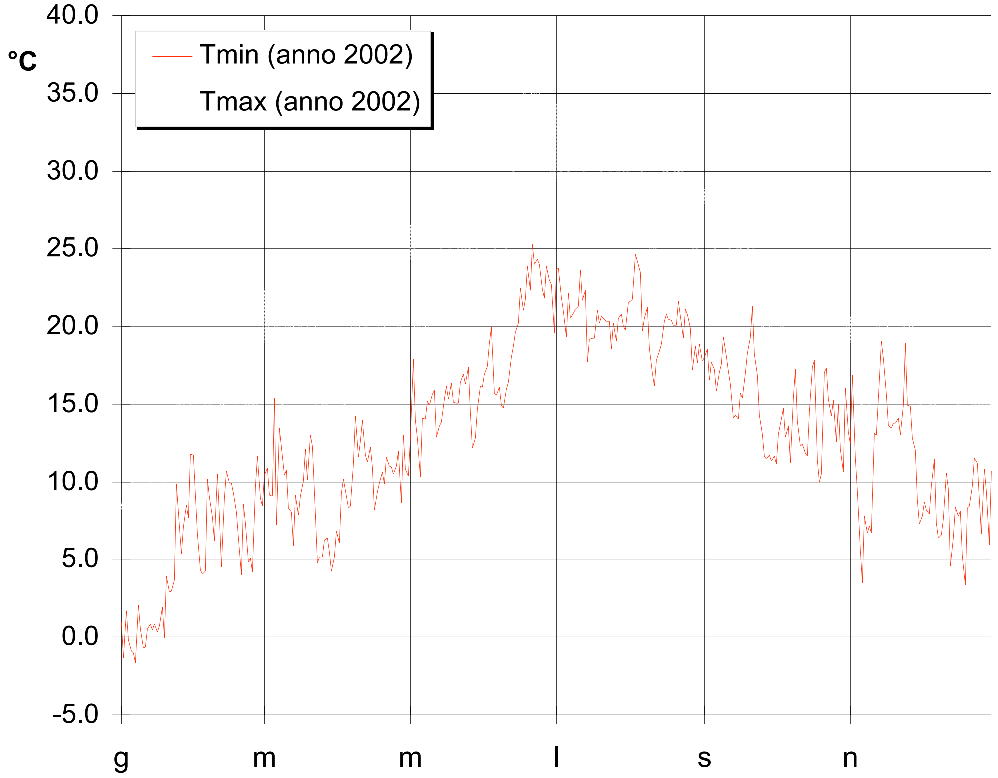

***Figure 5.4:** Annual temperature plot (2002 - Roma (Collegio Romano)*

5.3 Air conditioning units (UTA)

Three air conditioning units (UTA) provide the air handling for the whole SPARC complex: one for SPARC Main Hall, one for the clean room, and one for the control room.

***Table 5.3.** Air conditioning system summary*

UTA		**power in air**	**make up air**	**cold coil**	**water flow**	**air flow**
		KW	%	kW	l/s	mc/h
CONTROL ROOM	UTA SC	20.0	30.0	43.0	2.05	5882
PS ROOM						
CLEAN ROOM	UTA CP	3.0	3.0	8.0	0.38	882
SPARC HALL (phase 1)		8.0	13.0	10.0	0.48	2353
SPARC HALL (phase 2)	UTA SS	35.6	13.0	42.0	2.01	10471
CR AUXILIARY ROOM		20.0	30.0	30.0	1.43	5882
TOTAL (phase 1)		**51.0**		**91.0**	**4.3**	**15000**
TOTAL (phase 2)		**78.6**		**123.0**	**5.9**	**23118**

All the UTA systems have the same design: all air with partial recirculation, two separate fans for supply and return air, return/fresh air mixing section with exhaust air expulsion, exhaust air enthalpy recovery, pre-heating and cooling coil, steam humidifying section, post-heating coil.

Table 5.4: *Air conditioning design values*

	T set	Accuracy(t)
	°C	°C
CONTROL ROOM	22-25(*)	±1
PS ROOM (**)	NA	NA
CLEAN ROOM	20	±1
SPARC HALL	24	±2
CR AUXILIARY ROOM	24	±2

(*) winter-summer (*)ventilation only

The regulation of the cooling and post-heating coils shall be in sequence on supply air temperature compensated by room temperature at fixed point; the humidification/dehumidification shall be regulated by return air moisture content, piloting in sequence the steam producer and the cooling coil (whose set-point shall be the minimum between the two mentioned); the pre-heating coil is regulated at fixed point by the temperature after humidification.

The level of air quality shall be obtained by a EU3 pre filter and EU7 filter; clean room shall have an additional EU13 stage inside the air terminal units.

The energy efficiency is achieved by the use of: enthalpy recovery of exhaust air, the free cooling or heating based on the evaluation of the enthalpy difference between inside and outside environments, and the design of hot coils at a relatively low temperature to exploit of low level heat recycled from cooling of RF structures.

5.4 Clean room

A ISO 7 (at rest) class clean room shall house the laser equipment (see Table 5.4 for thermo-hygrometric conditions). The air distribution shall be of turbulent type, typical for that class; nevertheless the air velocity inside the room shall be maintained below 0.15 m/s at the height of laser equipment ($0.80 < h < 1.5$ m).

The "at rest" class condition has allowed the lowering of the required air flow, allowing smaller ducts suitable for the little existing holes between the SPARC hall and outside. The air handling unit (UTA) has been placed outside the underground hall, avoiding any vibration interference.

5.5 Noise and vibration

Care shall be paid in selecting proper equipment features to achieve noise and vibration reduction: chiller's compressors shall be rotating, all the axial fans (UTA, dry coolers, chiller condensers) shall have aerodynamic profiles and low regimes, the velocity of air in ducts shall be less than 7 m/s, the frontal air velocity in UTA coils shall be less than 2 m/s, the water velocity in piping shall be less than 1 m/s, the chillers shall have acoustic coffres and the UTA shall have thick (50 mm) side panels and noise suppressors at inlet and outlet. All the rotating equipment shall have properly designed anti-vibrating pads or supports.

A special program of field measures has just started to assure the stability of the laser devices with respect to machine-induced vibrations. The measures shall allow a better design of supports and damping devices.

5.6 Monitoring and control

A standard field bus (CANbus or PROFIbus) shall be employed to connect local devices like chiller microprocessors or temperature controllers to a PC based Central Unit for commissioning and monitoring. The programming environment shall be NI LabView. The automation of the plant shall be reduced to the essential, avoiding long debugging and excessive branching of the failure tree. All the information necessary to the accelerator complex shall be shared with control room and stored in a database.

5.7 Commissioning, test and balancing (TAB) procedure

Any high quality design will not produce acceptable results without an precisely planned commissioning procedure, which contains the following features:

- pressure test of the whole assembly;
- setting the working point of each pump and fan;
- balancing the hydraulic and air conditioning networks to assure the proper flows, with general, branch and terminal monitoring;
- short time tests for matching the elements of control loops;
- preliminary open loop tests and medium time tests to set and verify the parameters of PID controller;
- performance test and thermodynamic balancing of chillers, UTA, heat exchangers, ice storage and dry coolers;
- medium-long time tests to bring the system to design performance.

6. Organization and Management

6.1 PROJECT MANAGEMENT

The SPARC project is a collaboration among several institutions with 4 main research activities under a clear responsibilities. These activities are coordinated through a steering committee, lead by ENEA.

The basic scheme of the collaboration is therefore:

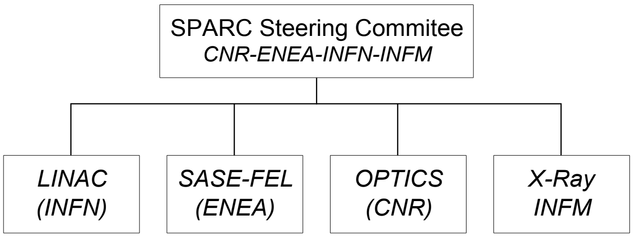

The INFN group responsible for the design and construction of a high brilliance 150 MeV photo-injector, adopted the following organization.

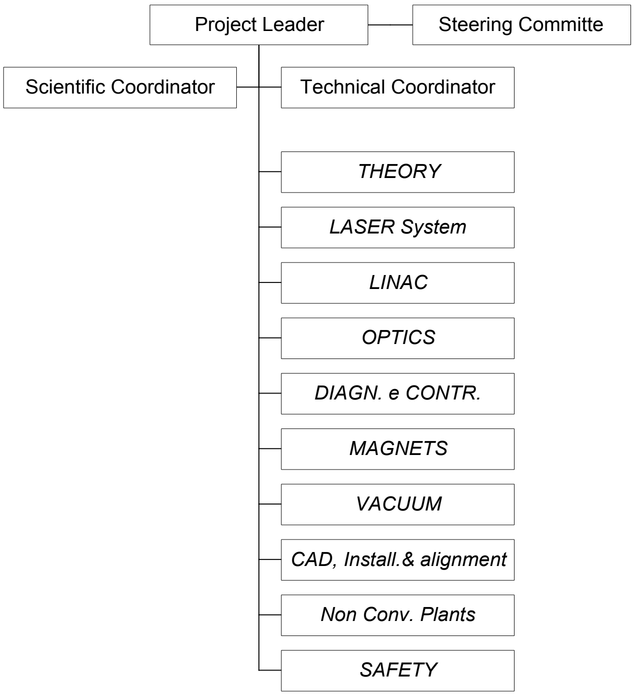

7. Project costs and schedule

7.1 OVERVIEW

The investment costs given in this chapter include all the components necessary for the construction of the 150 MeV SPARC photo-injector. Additional costs for the experimental hall installation plants, civil engineering, control room, environment, safety and health are not included. The personnel cost is also not included in the estimate.

7.2 COST ESTIMATE BASIS

The cost estimate has been obtained through preliminary contacts with firms or organizations able to deliver most of the main devices of the photo-injector, *i.e.* the drive laser system, the RF linac, RF gun, magnets, vacuum system, diagnostics and control systems. The total cost is 5.100.00 k .

7.3 MANPOWER REQUIREMENTS

The man power required for the different stages of the project, (design, procurement, fabrication and assembling, testing, installation and commissioning has been estimated mainly on the basis of the vast experience available in the Laboratori Nazionali di Frascati, which has allowed to build accelerator and detectors of much bigger size, as DAFNE, Kloe, Finuda etc. The manpower will be supplied mainly by LNF, Accelerator Division.

A total of about 60 man-years for the physicists and engineers and 30 man-years of technicians will be required. The total technicians man-power, per activity and per year, has been estimated as follows:

Table 7.1 *Technician manpower requirements*

TECHNICIAN MANPOWER for ASSEMBLY/COMMISSIONING				
	2003	2004	2005	tot
Mech. Draw.	2	2	0,5	4,5
Laser Optics		0,25	0,25	0,5
RF system	1	4	4	9
Vacuum	1	2	2	5
Diagn.Controls	1,5	3	3	7,5
Magnets	1	1	1	3

This level of technician manpower is available at LNF.

7.4 SCHEDULE

The construction time of SPARC Injector is 3 years, as indicated in the MIUR call for proposal. The start is January 2003, when the project has been funded by MIUR, although the budget was not been available at INFN until April 2003.

The evaluation is based on the long experience at LNF in building large facilities and detectors, and on the relatively small size of the linac. The preliminary elaboration of a construction schedule, is given in the following table.

Table 7.2 *SPARC schedule, high-level breakdown*

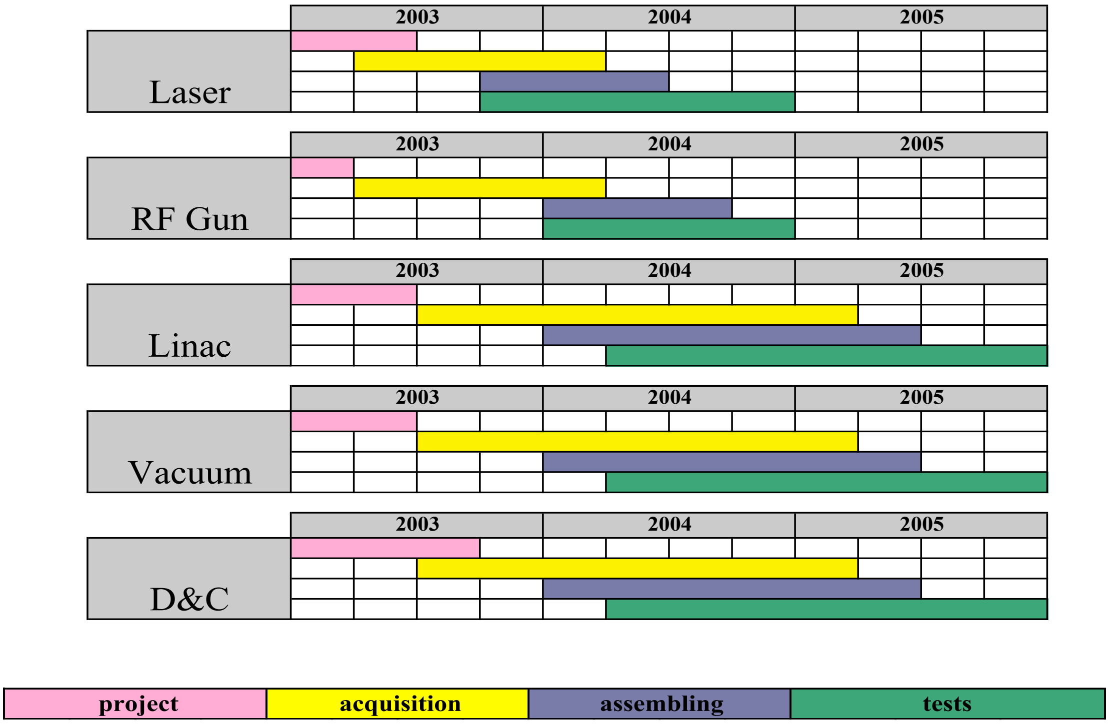

The schedule is tight, and it is necessary to speed up all the processes, in particular those of hardware system acquisition which might suffer of delays due to bureaucracy, and thus subsequently lead to delays in construction.

Each phase of the project is taken under control with WBS tools.